Dissertation

submitted to the

Combined Faculties of the Natural Sciences and Mathematics

of the Ruperto-Carola-University of Heidelberg, Germany

for the degree of

Doctor of Natural Sciences

Put forward by

Mikhail Kovalev

born in: Kursk, USSR

Oral examination:11.11.2019

NLTE analysis of the Gaia-ESO spectroscopic survey.

Referees: Dr. Maria Bergemann

Prof. Dr. Andreas Quirrenbach

Abstract

ZUSAMMENFASSUNG: In dieser Arbeit entwickeln wir eine Pipeline zur spektralen Analyse, die synthetischen NLTE Spektren mit *the Payne* (Ting et al. 2018) Spektralmodel kombiniert. Wir berechnen zwei spektrale Gitter, in einem der Gitter werden alle Elemente mit LTE behandelt und das zweite Gitter wird unter Verwendung von Eisen, Magnesium, Titan und Mangan mit NLTE modelliert, um NLTE Effekte auf die Bestimmung stellarer Parameter und Elementhäufigkeiten zu untersuchen. Diese Pipeline wird auf Spektren aus der dritten öffentlichen Datenveröffentlichung von Gaia-ESO (Gilmore et al. 2012) angewandt. Wir prüfen unsere Methodik mit einer Stichprobe von Standardsternen und Mitgliedern von Sternhaufen und finden signifikante Unterschiede zwischen NLTE und LTE im metallarmen Bereich. Die Elementhufigkeiten von Eisen und Titan sind homogen in allen Sternhaufen, aber mehrere Kugelsternhaufen zeigen eine signifikante Dispersion für [Mg/Fe]. Die Verringerung des mittleren [Mg/Fe] in einigen Kugelsternhaufen, im Vergleich zu Feldsternen mit vergleichbarer Metallizität, deuten möglicherweise eine *ex-situ* Entstehungsgeschichte an.

Wir kombinieren unsere NLTE Resultate auch mit den astrometrischen Daten des Gaia DR2 (Gaia Collaboration et al. 2018), um die chemo-dynamische Entwicklung der Milchstraße zu untersuchen. Wir nutzen die Unterschiede in der chemischen Zusammensetzung, um Scheibenpopulationen mit hohem [α/Fe] und niedrigem [α/Fe] zu unterscheiden. Halo Sterne werden durch Unterschiede in der Kinematik ausgewählt. Wir bestätigen frühere Ergebnisse, wie eine höhere Elementhäufigkeit von Mg im Vergleich zur Sonne im metallarmen Bereich und einen Abfall von [Mg/Fe] im Vergleich zur Sonne im metallreichen Bereich. Wir finden ein konstantes NLTE [Mg/Fe] ~ 0.3 dex Verhältnis sowohl fr die metallarme Scheibe als auch den Halo mit relativ kleiner Streuung zwischen einzelnen Sternen. Die Halo Sterne mit [Mg/Fe] vergleichbar zur Sonne wurden wahrscheinlich von anderen Galaxien eingefangen. Die beobachtete Exzentrizitätsverteilung für hohe [α/Fe] Scheiben Populationen schließt einen gewaltsamen Formationsmechanismus für die dicke Scheibe wie direkte Akkretion und dynamische Anregung aus. Die gemessenen chemischen und kinematischen Gradienten und Geschwindigkeitsdispersionen der Populationen mit hohem [α/Fe] können mit gasreichen Mergern erklärt werden, wobei radiale Migration nicht zu vernachlssigen ist.

ABSTRACT: In this work, we develop the spectral analysis pipeline that combines the NLTE synthetic spectra with *the Payne* spectral model (Ting et al. 2018). We compute two spectral grids, one grid with all elements treated in LTE and a second grid with iron, magnesium, titanium and manganese modelled in NLTE, to study the NLTE effects on the determination of the stellar parameters and chemical abundances. This pipeline is applied to spectra from the third public data release of the Gaia-ESO (Gilmore et al. 2012). We validate the method on the subsample of standard stars and cluster's members and find significant differences between NLTE and LTE in the metal-poor regime. All clusters are homogeneous in Fe and Ti, but several globular clusters showed significant dispersion in [Mg/Fe]. The depletion of the mean [Mg/Fe] in several globular clusters, compared to field stars of the same metallicity, may indicate their *ex-situ* formation history.

We also combine our NLTE results with Gaia DR2 (Gaia Collaboration et al. 2018) astrometric data to study Galactic chemo-dynamic evolution. We apply chemical separation to select high-[α/Fe] and low-[α/Fe] disk populations, with halo stars selected using kinematics. We confirm previous results like super-solar Mg abundance in the metal-poor regime and decrease of [Mg/Fe] to the solar abundances in the metal-rich regime. We find a constant NLTE [Mg/Fe]$\sim$ 0.3 dex ratio for both metal-poor disk and halo with relatively small star-to-star scatter. The halo stars with solar-like [Mg/Fe] are probably accreted from the other galaxies. The observed eccentricity distribution for high-[α/Fe] disk population rules out a violent thick disk formation mechanisms like direct accretion and dynamic heating. The measured chemical and kinematic gradients and velocity dispersions of the high-[α/Fe] population can be explained by the gas-rich merger scenario with the non-negligible contribution from the radial migration.

Contents

List of Figures

List of Tables

Acknowledgments

I would like to thank my host institute Max Plank Institute for Astronomy. I have great time there, working with many real professionals, which were always ready to help.

I am very grateful to my supervisor Dr. Maria Bergemann who believed in me and gave possibility to continue my astronomical carrier and learn many new interesting things and also helped me with many scientific and living issues.

I am very grateful to Prof. Andreas Quirrenbach for readily agreeing to referee this thesis. Furthermore I wish to thank Prof. Christian Fendt and Prof. Björn Malte Schäfer for willingly joining my examination committee.

I would like to acknowledge my collaborators Yuan-Sen Ting and Hans-Walter Rix for helpful comments and suggestions that allow to solve many scientific problems.

I want to thank my former and current office-mates Christos, Asmita, Jonas, Ricardo, Yulong, Alex, Ivana and Johannes for good working atmosphere and many interesting discussions on various topics.

I want to thank all people who helped and supported me during writing of this thesis. Especially I appreciate help from Kseniya, who gave very useful comments that greatly improved scientific content of the thesis. Special thanks go to Hans, Andy, Christos and Alex for the careful proof reading of this manuscript.

Chapter 1

Introduction

1.1 Motivation

We live in an era when scientists can explore various properties of the stars, starting from their luminosities, positions and velocities in the Milky Way Galaxy and ending with their detailed chemical compositions and ages. All this information comes from different astronomical techniques like astrometry, photometry, interferometry and spectroscopy. This thesis is focused on use of spectroscopy to analyse stars.

Spectroscopy has been developed since the 19^{th} century when Joseph Fraunhofer (1814) discovered absorption lines in the solar spectrum. Later Gustav Kirchhoff and Robert Bunsen (1859) found similar emission lines in spectra of gases. Further studies proved that spectroscopy is a great scientific tool. For example in 1868 a new chemical element - Helium was discovered by Jules Janssen and Norman Lockyer on the Sun and only in 1895 found on the Earth by William Ramsay. The reasonable interpretation of patterns visible in spectral lines of different atoms supported the development of a completely new area in physics – quantum theory.

The stellar spectrum carries a lot of information: line of sight velocity of the star via the Doppler shift of spectral lines, effective temperature $T_{\rm eff}$ via the shape of the continuum and strength of the lines. Additional information about star's rotation, size, mass, chemical composition is also encoded in the strength and shape of spectral lines. The combination of these parameters with other sources of data like photometry, astroseismology and evolution models allow us to estimate stellar ages and can tell us more about the interior of the star. All these properties can be constrained from stellar spectra with a principal restriction that analysis requires good spectral models which reflect all possible dependencies on modelled properties.

Using simplifications and approximations can produce biased results, which will lead to an incorrect interpretation of stellar properties and therefore a lot of effort should be given to accurate and careful modelling of stellar spectra. The progress in electronics and numerical methods allow us to model stellar atmospheres and predict how stellar spectra will look like. Several techniques were developed for the analysis of stellar abundances like equivalent width or spectrum synthesis analysis methods.

Thanks to multi-fibre spectrographs many stars can be observed at the same time which leads to a prodigious amount of spectra. Recently, several large spectroscopic surveys like RAVE (Steinmetz et al. 2006), APOGEE (Majewski et al. 2015), Gaia-ESO (Gilmore et al. 2012), GALAH (Buder et al. 2018b), LAMOST (Cui et al. 2012) have become available, bringing hundreds of thousands stellar spectra to the scientific community. Information content has to be recovered from all these observations, therefore an efficient method is required to accurately analyse large samples of stellar spectra.

1.2 Theoretical basis of spectral modelling

In spectroscopic observations, we can see only the outer layer of the star - the stellar atmosphere. In this relatively thin and cool region of the star, called the photosphere, radiation coming from hotter central parts interacts with atoms, ions, electrons and molecules of the atmosphere.

Generally spatial and temporal dependencies of these interactions are very difficult to model, therefore some simplifications can be made:

- the stellar atmosphere consists of homogeneous plane-parallel or spherical-symmetric layers,
- the atmosphere is in hydrostatic equilibrium, such that pressure is balanced by gravitational force,
- radiation flux conservation,
- no thermal conductivity, therefore energy can be transferred only by radiation and convection,
- convection is described by the mixing length theory (Böhm-Vitense 1958), which introduces free parameters such as mixing length and micro-/macroturbulence.

In the case of plane-parallel geometry, interaction of the light with the atmosphere can be described by the radiative transfer (RT) equation:

$$\cos\theta \frac{dI_\nu}{dz} = -\kappa_\nu \rho I_\nu + \eta_\nu \rho, \tag{1.1}$$

where dI_ν is the change of the specific intensity as light goes through layer with thickness dz, ρ is a mass density of the layer, θ is the angle between the direction of light ray and axis z, and κ_ν and η_ν and the absorption and emission coefficients, respectively.

The ratio of absorption and emission coefficients gives a source function:

$$S_\nu = \frac{\eta_\nu}{\kappa_\nu}, \tag{1.2}$$

which can be seen as specific intensity at some point in the atmosphere. We can rewrite equation 1.1 using optical depth $d\tau_\nu = \kappa_\nu \rho dz$ in the following form:

$$\mu \frac{dI_\nu}{d\tau_\nu} = -I_\nu + S_\nu, \tag{1.3}$$

where $\mu = \cos\theta$.

Integrating this equation from τ_ν to ∞, using dummy variable t_ν we got depth and angle dependent outgoing intensity (Gray 2005):

$$I_\nu^{out}(\tau, \mu) = \int_{\tau_\nu}^{\infty} S_\nu e^{-(t_\nu - \tau_\nu)/\mu} \frac{dt_\nu}{\mu}. \tag{1.4}$$

From observations of stars, one usually measures stellar flux F_ν, thus we need to integrate I^{out} over stellar disk (Gray 2005):

$$F_\nu = 2\pi \int_{\tau_\nu}^{\infty} S_\nu \int_0^1 e^{-(t_\nu - \tau_\nu)/\mu} dt_\nu d\mu = \int_{\tau_\nu}^{\infty} S_\nu E_2(t_\nu - \tau_\nu) dt_\nu, \tag{1.5}$$

where $E_2(x) = \int_1^\infty \frac{e^{-xw}}{w^2} dw$ - second exponential integral.

Therefore, to compute flux F_ν we need S_ν, that includes all emission and absorption processes in lines and continuum

$$S_\nu = \frac{\kappa_\nu^{cont} S_\nu^{cont} + \sum_{line} \kappa_\nu^{line} S_\nu^{line}}{\kappa_\nu^{cont} + \sum_{line} \kappa_\nu^{line}}. \tag{1.6}$$

Continuum absorption is dominated by the bound-free H$^-$ ion components for solar-like stars, whereas the free-free H$^-$ component and the neutral H component can become important for significantly hotter stars at shorter wavelengths.

For the atmosphere modelling one takes to account all opacity sources, but the number of absorption lines can exceed a few millions. Therefore they are usually treated using opacity distribution functions (ODF) or opacity sampling (OS) methods. In the ODF method a distribution of absorption coefficients as a function of frequency is tabulated for a range of temperatures, pressures and chemical abundances. The OS method is a statistical approach in which the line opacity is sampled on a fine grid of wavelength points using detailed line profiles for each individual spectral line.

For source function in lines we can use the relation (Gray 2005):

$$S_\nu^{line} = \frac{2h\nu^3}{c^2}\frac{1}{\frac{g_u N_l}{g_l N_u} - 1}, \tag{1.7}$$

where g_i, N_i are, respectively the statistical weight and level population (number density) of upper u and lower l energy levels, corresponding to certain line transition.

Quite often local thermodynamic equilibrium assumption (LTE) is used in the modelling of the stellar atmospheres, where excitation-ionisation balance is determined only by thermal collisions of the particles. This assumption can be expressed by following equations:

- Bolzmann distribution of particles energy level populations:

  $$\frac{N_j}{N} = \frac{g_j}{U}e^{-\frac{E_j}{kT}}, U = \sum_i g_i e^{-\frac{E_i}{kT}}, \tag{1.8}$$

  where g_j, E_j are the statistical weight and energy of the level j, U is a partition function, N total number density and N_j number density for particles with E_j.

- Saha distribution of particle ionisation states:

  $$\frac{N_{i+1}}{N_i}N_e = \frac{2}{\Lambda_e^3}\frac{U_{i+1}}{U_i}e^{-\frac{E_{i+1}-E_i}{kT}}, \tag{1.9}$$

  where E_i is the energy required for ionisation of state i, N_i number density for particles in ionisation state i and $\Lambda_e = \sqrt{\frac{h^2}{2\pi m_e kT}}$ is the thermal de Broglie wavelength.

- Maxwell distribution of particles velocities:

  $$\frac{N(v)}{N}dv = \sqrt{\frac{m}{2\pi kT}}e^{-\frac{mv^2}{2kT}}dv, \tag{1.10}$$

  with $N(v)$ number density of particles with velocities in a range $[v, v + dv]$, k the Bolzmann constant and m the mass of the particle.

It is clearly seen that all these distributions are determined by local kinetic temperature T.

Combining equations 1.8 and 1.7 we find that the Plank function represents the source function S_ν in LTE.

$$B_\nu = \frac{2h\nu^3}{c^2} \frac{1}{e^{\frac{h\nu}{kT}} - 1}. \tag{1.11}$$

The aforementioned assumptions allow one to compute atmospheric structure. There are several grids of 1D LTE hydrostatic atmospheric models that are built for a given set of stellar parameters like effective temperature T_{eff}, surface gravity $\log(\mathrm{g}) = \log\left(GMR^{-2}\right)$, microturbulence ξ and chemical composition. See for example ATLAS9 by Castelli & Kurucz (2004), MAFAGS-OS by Grupp (2004a) or MARCS by Gustafsson et al. (2008).

The chemical composition is expressed through the abundance of each elements relative to hydrogen. Abundance of element X is taken as logarithmic ratio of total number densities of element X and hydrogen H:

$$\log A(\mathrm{X}) = \log N(\mathrm{X}) - \log N(\mathrm{H}) + 12, \tag{1.12}$$

where abundance of the hydrogen $\log A(\mathrm{H}) = 12$. Iron abundance is typically used as representative for all “metal” elements (everything heavier then H and He). All abundances usually scaled to the solar values:

$$[\mathrm{Fe/H}] = \log A(\mathrm{Fe}) - \log A(\mathrm{Fe})_\odot. \tag{1.13}$$

The physical parameters of the atmosphere, like the temperature distribution T and electron pressure P_e, are usually tabulated as functions of optical depth τ. All other parameters like level populations, can be computed using previously introduced assumptions, equation of state and chemical composition. For example in MAFAGS-OS models, used in this thesis, gas and electron pressures, temperature, mass density, continuum opacity are provided as a function of optical depth.

This LTE assumption works well, until non-local photons start to affect level populations. This is usually the case for high temperatures and low densities (i.e solar chromosphere and corona). In this case, to account for “non-locality” in the processes of radiative transfer and ascertainment of excitation-ionisation equilibrium of an element, the concept of non-LTE (NLTE) is introduced. The Saha-Bolzmann equations are replaced by statistical equilibrium equations (SE), where the sum of all incoming rates from every level j to level i is equals to the sum of all outgoing rates from level i to every level j. For example, an equation for level i (Bergemann & Nordlander 2014):

$$N_i \sum_{i \neq j} (C_{ij} + R_{ij}) = \sum_{j \neq i} N_j (C_{ji} + R_{ji}), \tag{1.14}$$

where C_{ij}, R_{ij} are collisional and radiative rates (per particle) which establish equilibrium number of atom/ions excited to level i.

The system of SE equations is closed by the equation of number conservation for a given element X:

$$\sum_{i,c} N(\mathrm{X})_{i,c} = \frac{\alpha_{\mathrm{X}}}{\alpha_{\mathrm{H}}} \left(\sum_j N(\mathrm{H})_j + N_p \right), \tag{1.15}$$

where $\alpha_{\mathrm{X}}/\alpha_{\mathrm{H}}$ is the fraction of all atoms and ions of the element X relative to that of H and N_p is a number density of all protons

The collisional rates are computed with (Bergemann & Nordlander 2014):

$$C_{ij} = N_e \int_{v_0}^{\infty} \sigma_{ij}(v) v f(v) dv, \tag{1.16}$$

where $\sigma_{ij}(v)$ is the collision cross-section, N_e is the number density of the electrons and $f(v)$ is the Maxwell velocity distribution (equation 1.10) and v_0 is the threshold velocity with $mv_0^2/2 = h\nu_0$.

The radiative rates are computed with (Bergemann & Nordlander 2014):

$$R_{ij} = \int_0^{\infty} \frac{4\pi}{h\nu} \sigma_{ij}(\nu) J_\nu d\nu, \tag{1.17}$$

$$R_{ji} = \int_0^{\infty} \frac{4\pi}{h\nu} U_{ij} \sigma_{ij}(\nu) \left(\frac{2h\nu^3}{c^2} + J_\nu \right) d\nu, \tag{1.18}$$

$$U_{ij} = \left(\frac{N_i}{N_j} \right)_{\mathrm{LTE}} e^{-\frac{h\nu}{kT}}, \tag{1.19}$$

where $J = \frac{1}{4\pi} \oint I_\nu d\omega$ - mean intensity, $\sigma_{ij}(\nu)$ - cross-section for transition $i \rightarrow j$. The cross-sections σ_{ij} are usually the most uncertain parameters in NLTE modelling, because quantum-mechanical calculations are usually available only for a limited number of the energy levels and transitions (Barklem 2016).

The SE equations 1.14 for any energy level should be solved together with the RT equation 1.3. The solution is usually obtained iterativelly, taking LTE as an initial guess.

In practice, results of NLTE calculations are usually stored in the form of a departure coefficients - ratios of NLTE to LTE level populations as a function of optical depth:

$$b_i = \frac{N_i^{\mathrm{NLTE}}}{N_i^{\mathrm{LTE}}}. \tag{1.20}$$

Inserting equation 1.20 into equation 1.7 we derive NLTE source function for lines

$$S_\nu^{line} = \frac{2h\nu^3}{c^2} \frac{1}{\frac{b_l}{b_u} e^{\frac{h\nu}{kT}} - 1}. \tag{1.21}$$

In order to compute flux we still need to know absorption coefficients κ_ν^{line}. Under the assumption of complete redistribution of the electrons (when process of de-excitation is independent on the preceding excitation process) line absorption coefficient is:

$$\kappa_\nu^{line} = b_l N_l^{\mathrm{LTE}} \frac{\pi e^2}{m_e c \rho} f_{ij} \psi(\nu - \nu_0) \left(1 - \frac{b_l}{b_u} e^{\frac{h\nu_0}{kT}}\right), \tag{1.22}$$

where f_{ij} is the oscillator strength, $\left(1 - \frac{b_l}{b_u} e^{\frac{h\nu_0}{kT}}\right)$ is the stimulated emission factor and $\psi(\nu - \nu_0)$ is the line profile.

The line profile describes the position, shape and width of the line. There are several physical processes that broaden lines:

- natural broadening, due to finite lifetime of an excited state, given by Lorentz profile with damping constant γ_R,

$$\psi(\nu - \nu_0) = \frac{\gamma_R/4\pi}{(\nu - \nu_0)^2 + (\gamma_R/4\pi)}, \tag{1.23}$$

- pressure broadening due to elastic collisions with nearby particles, given by Lorentz profiles

$$\psi(\nu - \nu_0) = \frac{\gamma_n/4\pi}{(\nu - \nu_0)^2 + (\gamma_n/4\pi)}, \tag{1.24}$$

  with damping constants γ_n, where index n is a number that characterise a dependence of the perturbing force on distance between particles: $n = 3$ for resonance broadening (collisions between hydrogen atoms), $n = 4$ for quadratic Stark effect (collisions with charged particles, quadratic to electric field strength), $n = 6$ for van der Waals broadening (collisions with neutral hydrogen atoms).

- Doppler broadening, due to the thermal and non-thermal (microturbulence) motions of the atoms, given by Gaussian profile

$$\psi(\nu-\nu_0)=\frac{1}{\sqrt{\pi}\nu_D}e^{-\frac{(\nu-\nu_0)^2}{\nu_D}}, \tag{1.25}$$

  with $\nu_D=\frac{\nu_0}{c}\sqrt{\frac{2kT}{m}+\xi_t^2}$,

- fine structure (spin-orbit interaction plus relativistic correction for kinetic energy), hyperfine structure (interaction between the magnetic field created by the electron and the magnetic moment of the nucleus), isotope (presence of the different isotopes) and Zeeman (interaction with external magnetic field) splitting.

The line profile is usually the Voigt-Hjerting function:

$$\psi(\nu-\nu_0)=\frac{H(a,v)}{\sqrt{\pi}\Delta\nu_D},\ v=\frac{\nu-\nu_0}{\nu_D},a=\frac{\gamma_R+\gamma_3+\gamma_4+\gamma_6}{4\pi\nu_D}. \tag{1.26}$$

This Voigt-Hjerting function is a convolution of the Lorenz (dominating in line wings) and Gaussian (dominating in line core) profiles.

There are also several broadening mechanisms that acts on emergent profile:

- macroturbulence broadening, due to non-thermal motions larger than photon mean free path, usually given by Gaussian profile,
- rotational broadening, due to stellar rotation, characterised by $v\ \sin i$, given by special rotational profile
- instrumental broadening, due to limited resolution of the spectrograph, usually given by Gaussian profile.

The result of convolution of the later three profiles with emergent flux, computed using equation 1.5, produces a synthetic spectrum. That spectrum can be compared with the observed one.

1.3 Analysis of observed spectra

In order to estimate atmospheric parameters and chemical composition we need to compare spectral lines in models with those of observations. There are several non-spectroscopic methods to constrain atmospheric parameters of the stars. For example, one can use photometric calibrations to compute T_{eff} and parallaxes plus stellar evolution models to get log(g). Also astroseismology can be used to constrain log(g). At the same time T_{eff} and log(g) can be determined from the spectra along with chemical abundances. There are two methods to do this: analysis of equivalent width of the lines and spectral synthesis.

In the first method we measure equivalent width (W_λ) for individual lines. W_λ of the spectral line is the width of the rectangle with a height equal to that of continuum emission (F_0) and with same area as considered line.

$$W_\lambda = \int_{-\infty}^{\infty} \left(1 - \frac{F_\lambda}{F_0}\right) d\lambda. \tag{1.27}$$

First the observed spectrum is searched for line suitable for abundance estimation. The selection is usually based on sufficient line strength and negligible blending by other lines. Iron lines are commonly used to determine atmospheric parameters, because they are usually numerous and strong.

Traditionally, effective temperature is constrained using excitation equilibrium. In this method we require no correlation between excitation potential and the abundance of each line. These can be achieved by variation of the temperature. Surface gravity can be constrained from ionisation balance between lines of neutral and ionised species $\log A(\text{FeI}) = \log A(\text{FeII})$. The microturbulence can be constrained by requiring no trend between line strength and abundance for all lines. Once all atmospheric parameters are derived, spectral lines of elements other than iron can be analysed.

The spectrum synthesis method is more general and can be applied for blended lines. The comparison of the observed spectral profiles to model spectrum can be done visually or using some optimisation algorithm, usually χ^2-minimisation. All spectral and broadening parameters are varied until the shape of the observed spectrum is reproduced by synthetic one. For example, a common way to determine T_{eff} is a fitting of Balmer lines wings (Mashonkina et al. 2008).

In both such approaches only small a portion (regions around strong lines) of the spectrum is actually analysed, therefore a major part of information is not used. Also such careful line-by-line analysis is slow and feasible for the exploration of large data sets.

1.3.1 Machine learning in spectroscopy

Recently new techniques have been developed for automatic spectral analysis. Most of them explore machine learning methods, which are designed to analyse large data sets. These methods do not necessary follow physical laws, but rather find empirical connections between spectral parameters and flux variations. The basic idea of these methods is to use some data set with well-known spectral parameters to create some predictive model *a training set* and apply it to data set with unknown parameters *the testing set*. In spectroscopy testing set contains observed spectra, while training set is a spectral library consisting spectra with known parameters. Such a library can be based on previously analysed real spectra (data-driven) or can be computed using spectral synthesis codes (model-driven).

One characteristic property of such methods is that they require significantly large training data set in order to perform well. Also they are presumed to work well only in region covered by training set, therefore their extrapolation ability is weak. Predictive models can be either forward or inverse. Forward model takes parameters as an input, while inverse model takes spectrum. Therefore, inverse models provide estimated parameters directly, while forward model require some additional algorithm to find optimal parameters, but it allows us to generate optimal spectrum. Usually inverse models are much faster than forward ones.

In what follows we will make overview of several inverse and forward predictive models.

Inverse models

Bailer-Jones et al. (1997) used a artificial neural network (ANN) for automatic spectral classification. In the following study Bailer-Jones (2000) ANN was used to determine three stellar parameters (T_{eff}, log(g) and [Fe/H]) from spectra of different quality and resolution. The subsequent study of Re Fiorentin et al. (2007) used a similar method to analyse SDSS/SEGUE spectra with ANNs trained on both real and synthetic spectra. This is an inverse model, that takes an observed spectrum as input and provides a stellar parameter as an output, with a hidden layer in between, see Fig. 1.1. Each layer consists of nodes with are connected with all nodes[1] on the previous or next layer. Such layers are called fully-connected. The output of hidden layers is activated by some non-linear function. This ANN can be seen as a non-linear composite function, where many hidden parameters (two for each

---

[1] Sometimes nodes are also called neurons

weighted connection: $y = wx + b$) were adjusted using information from synthetic spectra during the training procedure.

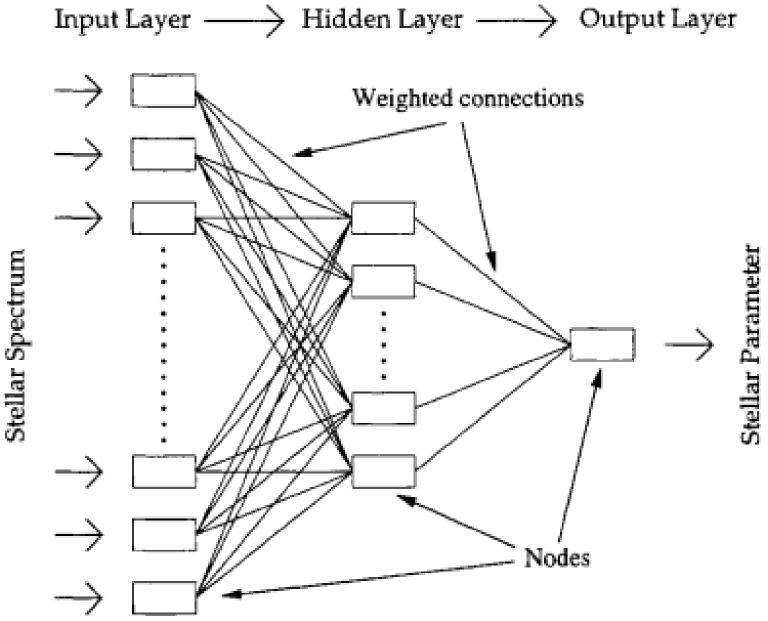

Figure 1.1: Example of simple ANN with one fully-connected hidden layer. Figure credit Bailer-Jones et al. (1997)

The MATISSE (MATrix Inversion for Spectral SynthEsis) algorithm has been specially developed for analysis of Gaia RVS spectra by Recio-Blanco et al. (2006). It uses linear combinations of the synthetic spectra as a basis vectors for spectral parameters: $T_{\text{eff}}, \log(\text{g})$ and [Fe/H]. They use local multi-linear regression to find optimal coefficients for the basis vectors during the training step. Stellar parameters are found through the projection projecting of observed spectrum on these basis vectors.

Fabbro et al. (2018) have applied deep learning techniques to APOGEE spectra in their inverse model called *StarNet*, using both real and synthetic spectra as a training set. *StarNet* used not only fully-connected layers like Bailer-Jones (2000), but also convolutional layers with max pooling. Such additional layers allow ANN to apply several filters to the input spectrum in order to detect features which are sensitive to output parameters. Output of the max pooling layer then goes to the fully-connected hidden layers.

The last inverse model, *AstroNN*, developed by Leung & Bovy (2019) employs Bayesian ANN to fit APOGEE spectra. This is a data-driven model, where the

ANN implementation basically mimics the standard APOGEE pipeline, deriving atmospheric parameters from the full spectrum and abundances of individual elements from spectral windows. In comparison with Fabbro et al. (2018) this ANN can utilise the uncertainty information for data from the training set and also work with spectra for which some parameters have missing values. This is done by implementing an objective function during training. Also such an ANN is able to estimate the uncertainties of the predicted parameters, via random dropout of some nodes in fully-connected layers.

Forward models

In the case of forward modelling we have some non-linear function that represents the flux spectrum at any arbitrary point in multidimensional parameter space.

$$F(\lambda|\mathbf{l}) = f(\mathbf{l}|\theta(\lambda)) + noise, \tag{1.28}$$

where $\mathbf{l}$ is the set of spectral parameters ($T_{\rm eff}$, $\log(\mathrm{g})$, $V_{\rm mic}$ and abundances), $\theta(\lambda)$ are the model parameters that describe model and the *noise* term is required only for models based on real spectra. The model parameters $\theta(\lambda)$ are determined during training step.

In *Canon* (Ness et al. 2015) a quadratic model was implemented to fit APOGEE spectra using the spectra of the stars in galactic stellar clusters as a training set. The model uses χ^2 minimisation to estimate $T_{\rm eff}, \log(\mathrm{g})$ and [Fe/H]. The equation 1.28 can be written as:

$$F(\lambda|\mathbf{l}) = \theta^T(\lambda)\mathbf{p_2}(\mathbf{l}) + noise, \tag{1.29}$$

where $\mathbf{p_2}(\mathbf{l})$ - quadratic polynomial of the spectral parameters. The model parameters $\theta(\lambda)$ are derived via least-square minimisation. In the follow up study by Casey et al. (2016a) this model is upgraded in order to fit chemical abundances. Later *Canon* was successively implemented to analyse spectra from the GALAH survey by Buder et al. (2018b). This approach was generalised by Rix et al. (2016) to a polynomial spectral model (not necessary quadratic), where *ab-initio* synthetic spectra are used as a training set.

Not all flux variations with spectral parameters can be well described by a quadratic formula, therefore Ting et al. (2018) use ANNs for forward modelling in the *Payne* code. In this approach, ANN have spectral parameters as an input layer, two fully-connected hidden layers and flux as an output layer. In this case, flux $F(\lambda|\mathbf{l})$ is approximated as:

$$F(\lambda|\mathbf{l}) = \mathbf{w_2}(\lambda)\sigma(\mathbf{w_1}(\lambda)\sigma(\mathbf{w_0}(\lambda)\mathbf{l} + \mathbf{b_0}(\lambda)) + \mathbf{b_1}(\lambda)) + \mathbf{b_2}(\lambda), \tag{1.30}$$

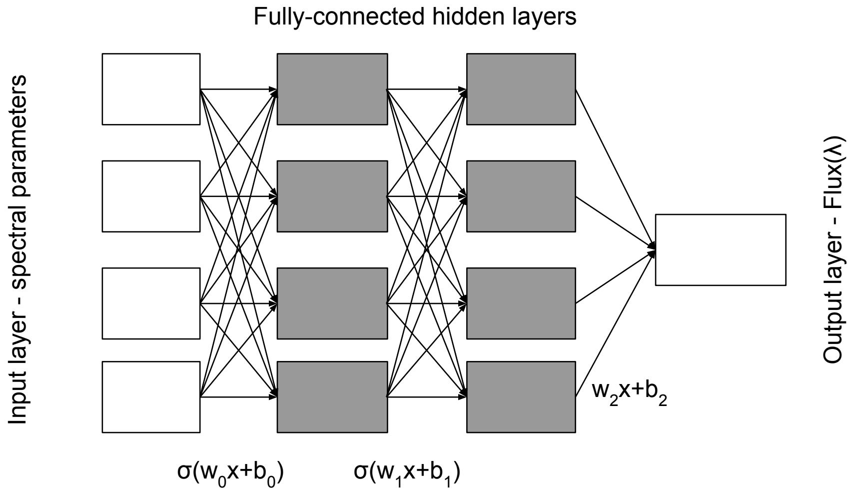

Figure 1.2: Schematic description of the *Payne* ANN.

where $\sigma(z) = (1 + e^{-z})^{-1}$ is a sigmoid function and $\mathbf{w_i}(\lambda), \mathbf{b_i}(\lambda)$ are matrices with parameters of weighted connections between nodes, see Fig. 1.2. This model was trained on synthetic spectra computed with ATLAS12 (Castelli & Kurucz 2004; Castelli 2005) atmospheric models and was applied to fit APOGEE DR14 spectra.

1.4 The Milky Way structure

The spectroscopic chemical composition contains useful information on interstellar medium from which a star was born, and together with knowledge of stellar kinematics, it allows one to study evolution of the Galaxy. The Milky Way is a spiral galaxy of SBbc type, according to Hubbles classification (Binney & Merrifield 1998). It can be roughly represented by a superposition of three components: bulge, halo, and disk. The bulge is a dense central part within radius of ~ 3 kpc, mostly populated by old stars and metal-rich globular star clusters. The infrared observations revealed the presence of the bar in the bulge (Bland-Hawthorn & Gerhard 2016). The halo has spherical shape, extending more than 30 kpc from the centre (Binney & Merrifield 1998). It is mostly populated by very old stars in stellar streams and metal-poor globular clusters. The disk contains the majority of the stellar content of the Galaxy. Based on photometric parallax technique it is subdivided onto the thin disk and thick disk components (Gilmore & Reid 1983). The thin disk with a scale length of 3.8 kpc and a scale height of 300 pc, while the thick disk has a scale length 2.0 kpc and a scale height of 900 pc (Jurić et al.

2008; Bensby et al. 2011). The thin disk is presumed to contain young low-[α/Fe][2] stars and open star clusters, while the thick disk consists of older high-[α/Fe] stars (Bensby et al. 2014). The schematic side-view of the Galaxy is shown in Figure 1.3.

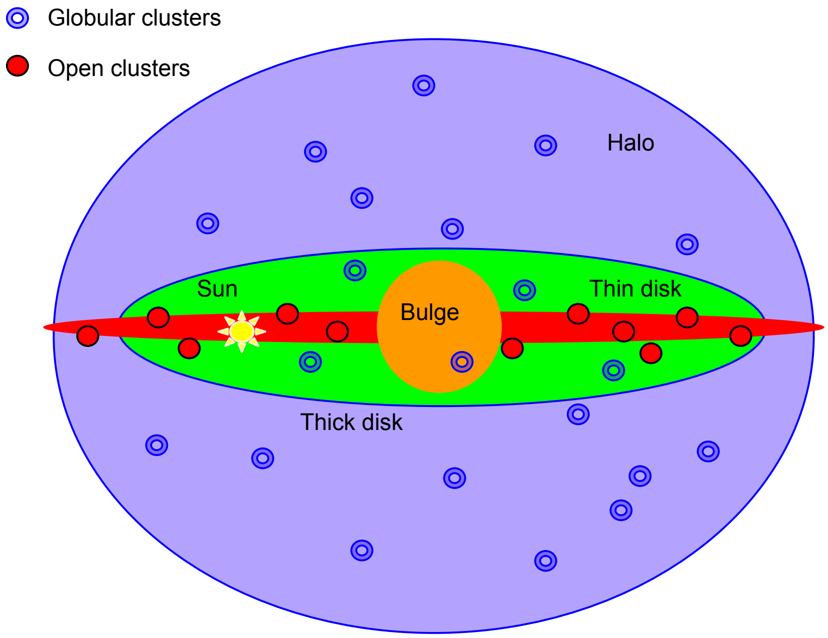

Figure 1.3: Schematic side-view of the Galaxy. (not to scale)

These thin/thick disks are present in almost all present-day spiral galaxies (Comerón et al. 2019), therefore origin of such structures is very important for our understanding of galaxy formation. There are two formation mechanisms: violent and secular origin. The former includes the direct accretion of stars from the disrupted satellite galaxies (Abadi et al. 2003) or dynamical heating of the primordial thin disk via an infalling satellite (Freeman 1987; Quinn et al. 1993; Villalobos & Helmi 2008). In the latter mechanism the thick disk forms in a starburst, during a gas-rich mergers (Brook et al. 2004, 2007) or as a result of the redistribution of stellar orbits via scattering on transient spiral arms - radial migration (Roškar et al. 2008; Schoenrich & Binney 2009a; Loebman et al. 2011). There is also a model proposed in Minchev et al. (2013), which utilises several scenarios at different stages of disk evolution. In that model, an early merger event is required to enable intensive radial migration of the inner disk stars to outer regions. Validations of one scenario or the other is possible only with help of observations in stellar chemistry and kinematics.

---

[2] The α-elements are chemical elements with even periodic numbers that are produced via the capture of α-particles in the massive stars ($M > 8M_\odot$) and include O, Ne, Mg, Si, S, Ar, Ca and Ti. The [α/Fe] usually represents the [<Mg,Si,Ca,Ti>/Fe].

1.5 Kinematic properties of the stars

In order to compute stellar positions and velocities we need astrometric observations along with spectroscopic line-of-sight velocities. Fortunately the Gaia space mission (Gaia Collaboration et al. 2018) provides a 5D astrometric solution $(\alpha, \delta, \mu_\alpha, \mu_\delta, \varpi)$ for millions of stars in the Galaxy. The following section describes how to make use of this information to disentangle the formation mechanisms of the Milky Way.

1.5.1 Galactocentric coordinates and velocities

Consider a right-handed galactocentric Cartesian system $\mathbf{X_g Y_g Z_g}$ (Figure 1.4). Solar galactocentric coordinates are $\mathbf{r}_\odot = (X_\odot,\ Y_\odot,\ Z_\odot)^T = (-8.0,\ 0.0,\ 0.0)^T$kpc.

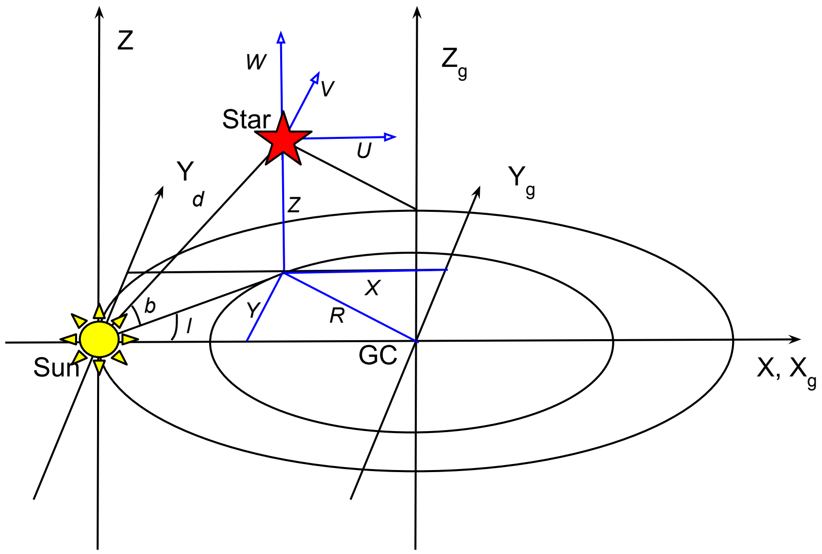

Figure 1.4: Galactocentric Cartesian system definition. GC is the galactic centre, d is the heliocentric distance to the star, l, b are the spherical galactic coordinates of the star, $X,\ Y,\ Z$ are the galactocentric Cartesian coordinates of the star.

Assume we know the distance d to the star (i.e. using parallax $d = \varpi^{-1}$) and it has ICRS[3] coordinates α, δ. So the galactocentric coordinates of the star in can be

---

[3] Inertial celestial reference system given for epoch "J2000", that is, the Julian date 2451545.0 or 01/01/2000 11:58:55.816 UTC.

computed from ICRS position using:

$$\begin{pmatrix} X \\ Y \\ Z \end{pmatrix} = \mathbf{A}'_{\mathbf{G}} \begin{pmatrix} d\cos\alpha\cos\delta \\ d\sin\alpha\cos\delta \\ d\sin\delta \end{pmatrix} + \mathbf{r}_{\odot}, \tag{1.31}$$

with ICRS to Galactic coordinates transformation matrix

$$\mathbf{A}'_{\mathbf{G}} = \boldsymbol{R}_z(-l_{\Omega})\boldsymbol{R}_x(90^{\circ} - \delta_{\mathrm{G}})\boldsymbol{R}_z(\alpha_{\mathrm{G}} + 90^{\circ}) \tag{1.32}$$

$$\boldsymbol{R}_x(\theta) = \begin{pmatrix} 1 & 0 & 0 \\ 0 & \cos\theta & \sin\theta \\ 0 & -\sin\theta & \cos\theta \end{pmatrix} \tag{1.33}$$

$$\boldsymbol{R}_z(\theta) = \begin{pmatrix} \cos\theta & \sin\theta & 0 \\ -\sin\theta & \cos\theta & 0 \\ 0 & 0 & 1 \end{pmatrix}, \tag{1.34}$$

with $(\alpha_{\mathrm{G}}, \delta_{\mathrm{G}}) = (192.85948^{\circ}, +27.12825^{\circ})$ being the Galactic north pole ICRS coordinates, and $l_{\Omega} = 32.93192^{\circ}$ is the galactic longitude of the first intersection of the galactic plane with the equator (Kovalevsky et al. 1997). Computed with these values:

$$\mathbf{A}'_{\mathbf{G}} = \begin{pmatrix} -0.0548755604162154 & -0.8734370902348850 & -0.4838350155487132 \\ +0.4941094278755837 & -0.4448296299600112 & +0.7469822444972189 \\ -0.8676661490190047 & -0.1980763734312015 & +0.4559837761750669 \end{pmatrix}. \tag{1.35}$$

Assume the star has a line-of-site velocity and proper motions $V_{\mathrm{los}}, \mu'_{\alpha}, \mu_{\delta}$ with $\mu'_{\alpha} = \mu_{\alpha}\cos\delta$. The peculiar motion of the Sun is given in the Cartesian values $\mathbf{v}_{\odot} = (U_{\odot}, V_{\odot}, W_{\odot})^T = (11.1,\ 12.24,\ 7.24)^T\ \mathrm{km\,s^{-1}}$ (Schönrich et al. 2010). Differentiating by time formula 1.31 gives us the velocity components $(dX/dt,\ dY/dt,\ dZ/dt) = (U,\ V,\ W)$ in the form:

$$\begin{pmatrix} U \\ V \\ W \end{pmatrix} = \mathbf{A}'_{\mathbf{G}} \begin{pmatrix} \cos\alpha\cos\delta & -\sin\alpha & -\cos\alpha\sin\delta \\ \sin\alpha\cos\delta & \cos\alpha & -\sin\alpha\sin\delta \\ \sin\delta & 0 & \cos\delta \end{pmatrix} \begin{pmatrix} V_{\mathrm{los}} \\ 4.74\ d\ \mu'_{\alpha} \\ 4.74\ d\ \mu_{\delta} \end{pmatrix} + \mathbf{v}_{\odot}, \tag{1.36}$$

where U is positive towards the Galactic centre.

In order to get velocities in cylindrical coordinates we first define the Cartesian values corrected for the circular velocity at the solar radius

$$V_X = U, \tag{1.37}$$

$$V_Y = V + V_{\mathrm{c},\odot}, \tag{1.38}$$

$$V_Z = W, \tag{1.39}$$

where we use the nominal value $V_{c,\odot} = 220\,\mathrm{km\,s^{-1}}$. The cylindrical components are then

$$V_R = (XV_X + YV_Y)/R, \tag{1.40}$$

$$V_\phi = -(XV_Y - YV_X)/R, \tag{1.41}$$

$$V_Z = V_Z, \tag{1.42}$$

with $R = \sqrt{X^2 + Y^2}$, V_R the radial velocity, and V_ϕ the azimuthal velocity. Note minus sign in V_ϕ which we use to make clockwise solar circular motion positive.

1.6 Probing the thick disk formation scenarios

Knowledge of stellar positions and velocities allows us to compute stellar orbits using a model of the Galactic potential that represents a mass distribution within the Galaxy. One of the important orbital characteristics is an eccentricity e, which can be calculated as:

$$e = \frac{r_{apo} - r_{peri}}{r_{apo} + r_{peri}}, \tag{1.43}$$

where r_{peri} and r_{apo} denote the closest approach of an orbit to the Galactic center and the farthest extent of an orbit from the Galactic center.

From the eccentricity distribution of the stellar population, we can extract information about its dynamical origin. Sales et al. (2009) explored four scenarios in N-body model simulations and proposed using the eccentricity distribution of the thick disk stars to select a dominant formation scenario. We present their simulation results in Figure 1.5. They selected thick disk population as stars with $2R_0 < R < 3R_0$ (R_0 is a scale length of the thick disk) and at height from one to three scale-height of the thick disk. The distribution for the accretion scenario is very wide and has a median value at $e = 0.5$, and in the dynamical heating scenario eccentricities show a bimodal distribution with a higher peak at $e = 0.2$ and a lower peak at $e \sim 0.8$. The radial migration scenario has a narrow distribution that is centred at $e \sim 0.3$ and has a sharp cut-off at high eccentricities at $e = 0.7$. For the gas-rich merger scenario, the e distribution is centred at $e = 0.2$ and has a long tail down to $e = 0.9$. Sales et al. (2009) also suggest that a relatively small sample of ~ 150 stars is enough to distinguish a dominant scenario from the others at a 90% confidence level.

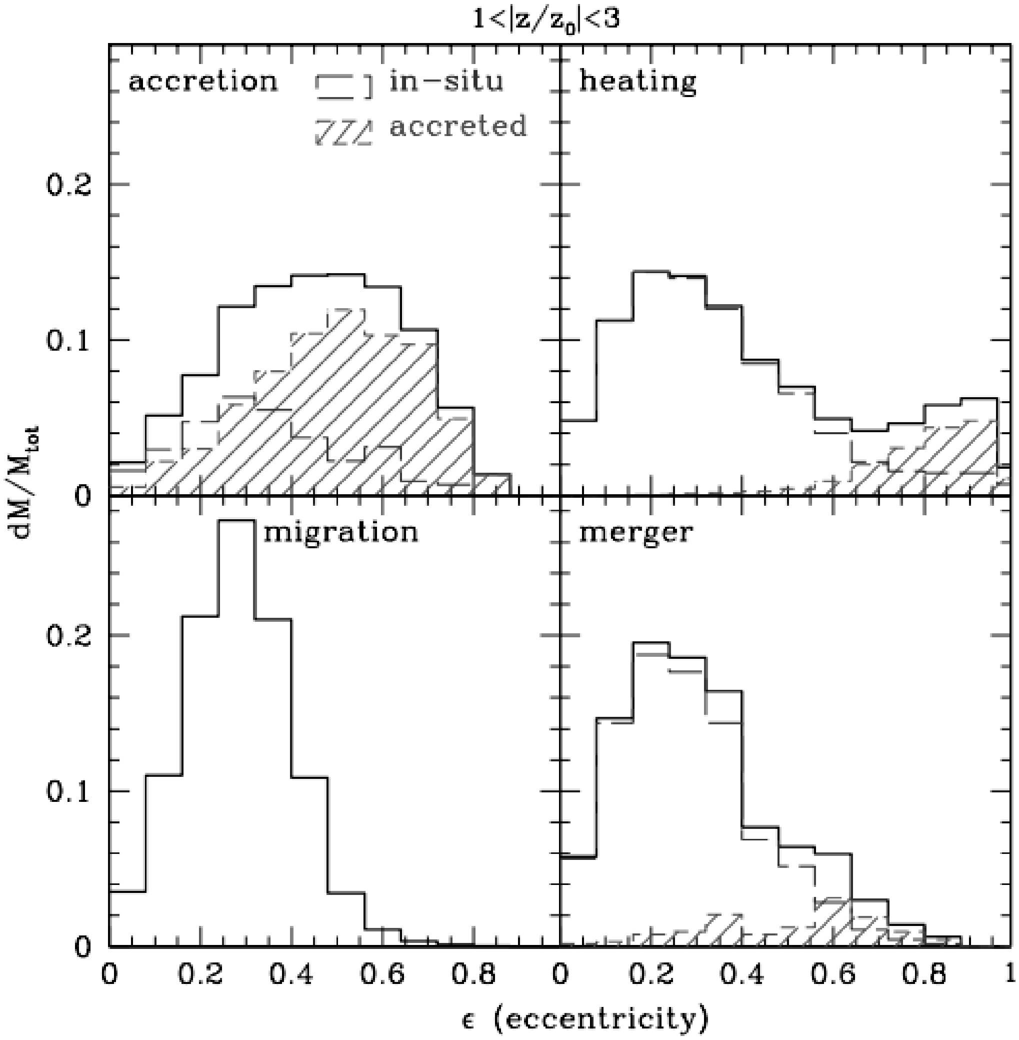

Figure 1.5: Eccentricity distributions as a probe of the thick disk formation scenario. Figure credit Sales et al. (2009)

1.7 This thesis

In this thesis we analyse spectra from the Gaia-ESO survey using NLTE synthetic models in combination with *the Payne* code. In Chapter 2 we present spectral analysis pipeline that use NLTE spectral models to study of NLTE effects on determination of stellar parameters and chemical abundances. We analyse stellar spectra in the sample containing Gaia benchmark stars and members of the galactic stellar clusters. In Chapter 3 we explore NLTE metallicity and abundance of magnesium together with astrometric information from Gaia second data release for Milky Way field stars in context of the Galactic chemical composition and dynamical evolution. In Chapter 4 we present the online-service that provides NLTE abundance corrections and spectral models for nine chemical elements in cool stars.

Chapter 2

NLTE Chemical abundances in Galactic open and globular clusters

This thesis chapter is based on article Kovalev et al 2019, *A&A 628, A54*

2.1 Introduction

Fast and reliable modelling of stellar spectra is becoming increasingly important for current stellar and Galactic astrophysics. Large-scale spectroscopic stellar surveys, such as Gaia-ESO (Gilmore et al. 2012; Randich et al. 2013), APOGEE (Majewski et al. 2015), and GALAH (De Silva et al. 2015) are revolutionising our understanding of the structure and evolution of the Milky Way galaxy, stellar populations, and stellar physics. The ever-increasing amount of high-quality spectra, in return, demands rigorous, physically-realistic, and efficient data analysis techniques to provide an accurate diagnostic of stellar parameters and abundances. This problem has two sides. Precise spectral fitting and analysis requires powerful numerical optimisation and data-model comparison algorithms. On the other hand, the accuracy of stellar label estimates is mostly limited by the physics of spectral models used in the model-data comparison. The fitting aspect has been the subject of extensive studies over the past years, and various methods (e.g. Recio-Blanco et al. 2006; Schönrich & Bergemann 2014; Ness et al. 2015; Casey et al. 2016b; Ting et al. 2018) have been developed and applied to the analysis of large survey datasets.

Major developments have also occurred in the field of stellar atmosphere physics. Non-local Thermodynamic Equilibrium (NLTE) radiative transfer is now routinely performed for many elements in the periodic table. This allows detailed calculations of spectral profiles that account for NLTE effects. NLTE models consistently describe the interaction of the gas particles in stellar atmospheres with the radiation field (Auer & Mihalas 1969), in this respect being more realistic than LTE models. In NLTE, photons affect atomic energy level populations, whilst in LTE those are set solely by the Saha equation for ionisation and by the Boltzmann distribution for excitation. NLTE models predict more realistic absorption line profiles and hence provide more accurate stellar parameters and abundances (e.g. Ruchti et al. 2013; Zhao et al. 2016). However, NLTE models are often incomplete in terms of atomic data, such as collisions with H atoms and electrons or photo-ionisation cross-sections. Major efforts to improve atomic data are underway (e.g. Yakovleva et al. 2016; Bautista et al. 2017; Belyaev & Yakovleva 2017; Barklem et al. 2017; Amarsi et al. 2018; Barklem 2018) and there is no doubt that many gaps in the existing atomic and molecular databases will be filled in the near-term future. Besides, strictly speaking, no single NLTE model is complete in terms of atomic data, and also quantum-mechanical cross-sections are usually available for a small part of the full atomic or molecular system (Barklem 2016).

In this work, we study the effect of NLTE on the analysis of stellar parameters and chemical abundances for FGK-type stars. We combine NLTE stellar spectral models with *the Payne*[1] code developed by Ting et al. (2018) and apply our methods to the observed stellar spectra from the 3^{rd} public data release by the Gaia-ESO survey. This work is a proof-of-concept of the combined NLTE-Payne approach and it is, hence, limited to the analysis to the Gaia-ESO benchmark stars and a sample of Galactic open and globular clusters, for which independent estimates of stellar labels, both stellar parameters and detailed abundances are available from earlier studies.

The chapter is organised as follows. In Section 2.2, we describe the observed sample, the physical aspects of the theoretical spectral models, and the mathematical basis of *the Payne* code. We present the LTE and NLTE results in Section 2.3 and compare them with the literature in Section 2.4. Section 2.5 summarises the conclusions.

---

[1] `https://github.com/tingyuansen/The_Payne`

2.2 Methods

2.2.1 Observed spectra

We use the spectra of FGK stars observed within the Gaia-ESO spectroscopic survey (Gilmore et al. 2012; Randich et al. 2013). These spectra are now publicly available as a part of the third data release (DR3.1)[2]. The data were obtained with the Giraffe instrument (Pasquini et al. 2002) at the ESO (European Southern Observatory) VLT (Very Large Telescope). We use the spectra taken with the HR10 setting, which covers 280 Å from 5334 Å to 5611 Å, at a resolving power of $R = \lambda/\Delta\lambda \sim 19\,800$. The average signal-to-noise ratio (S/N) of a spectrum ranges from 90 to 2800 per Å[3], with the majority of the spectra sampling the S/N in range of 150-200 Å^{-1}.

Our observed sample contains 916 FGK-type stars with luminosity classes from III to V that includes main-sequence (MS), subgiants, and red giant branch (RGB) stars. A fraction of these are the Gaia-ESO benchmark stars (174 spectra of 19 stars), but we also include 742 stars in two open and 11 globular clusters. We exclude four benchmark stars with effective temperature $T_{\rm eff} < 4000$ K, because this regime of stellar parameters is not covered by our model atmosphere grids. β Ara is not a part of our calibration sample, as it is not recommended as a benchmark in Pancino et al. (2017). These stars are previously analysed by Gaia-ESO (Smiljanic et al. 2014; San Roman et al. 2015; Pancino et al. 2017) and included in the The Gaia-ESO DR3 catalogue.

2.2.2 Instrumental profile

Similarly to technique that Damiani et al. (2016) used to obtain instrumental profile for Giraffe HR15N setting, we used sum of two Gaussian profiles to fit line at 5578 Å in calibration spectrum of thorium-argon lamp, downloaded from ESO webpage[4]. In the Figure 2.1 it is shown that such new instrumental profile describe spectral profile much better than simple Gaussian computed according to reported resolution of HR10 setting $R = 19\ 800$. Error of one-Gaussian profile can be upto

---

[2] `http://archive.eso.org/wdb/wdb/adp/phase3_spectral/form?collection_name=GAIAESO`

[3] We employ the following relationship: S/N [Å^{-1}]=$\sqrt{20}$ S/N [pixel^{-1}], where 20 pixels are equivalent to 1 Å, that is, the sampling of the Giraffe HR10 spectra.

[4] `http://www.eso.org/observing/dfo/quality/GIRAFFE/pipeline/SKY/html/GI_SRBS_2004-09-26T22_48_10.511_Medusa2_H548.8nm_o10.fits_details.html`

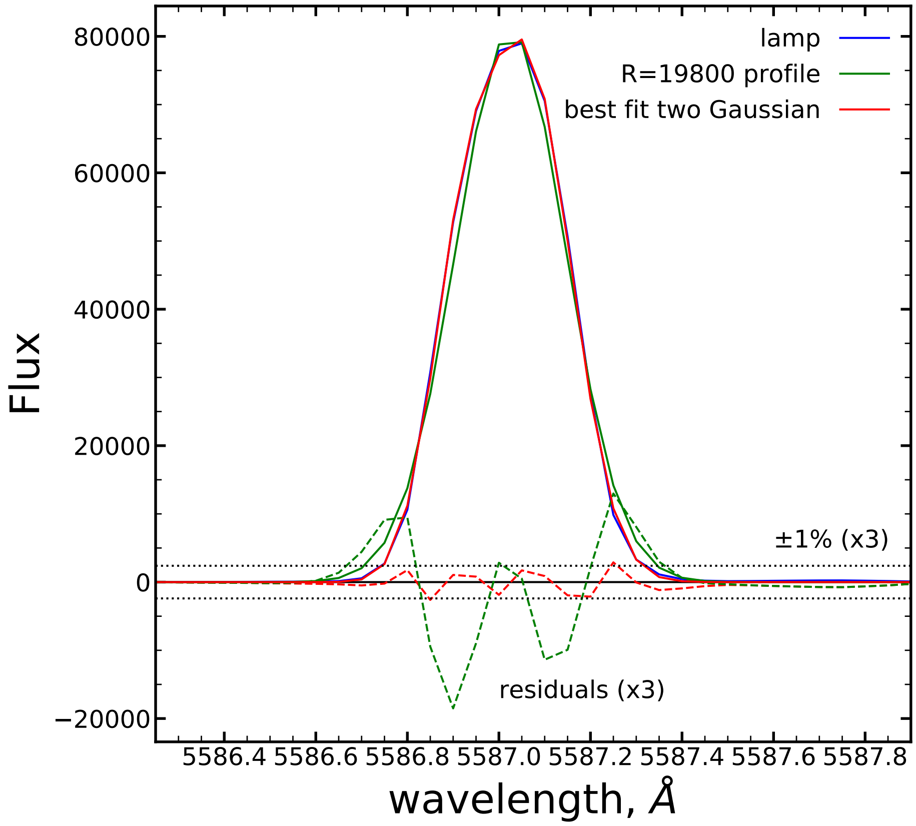

Figure 2.1: The results of instrumental profile fitting. Residuals of the fit are upscaled three times.

5-7%, while using two-Gaussian profile error always below 1% level. Resulting instrumental profile with best fitted parameters is listed below:

$$\lambda(v) = \frac{A_1}{\sqrt{2\pi\sigma_1^2}}\exp\left(-\frac{(v-v_1)^2}{2\sigma_1^2}\right) + \frac{A_2}{\sqrt{2\pi\sigma_2^2}}\exp\left(-\frac{(v-v_2)^2}{2\sigma_2^2}\right) \tag{2.1}$$

with $A_1 = 0.465$, $A_2 = 0.194$, $\sigma_1 = 4.971\,\mathrm{km\,s^{-1}}$, $\sigma_2 = 3.799\,\mathrm{km\,s^{-1}}$, $v_1 = -2.249\,\mathrm{km\,s^{-1}}$, $v_2 = 5.754\,\mathrm{km\,s^{-1}}$.

2.2.3 Radial velocities

Spectra in public data release are not corrected to rest frame, so they require radial velocity (RV) correction in order to be compared with synthetic spectra. We estimate the RV by cross-correlating the observed spectrum with a synthetic spectral template, which is shifted in the RV range of ±400 $\mathrm{km\,s^{-1}}$ (typical for stars in the Galaxy) with a step of 0.5 $\mathrm{km\,s^{-1}}$. We tested several combinations of stellar parameters and find that template computed in metal-poor dwarf parameters ($T_{\rm eff} = 5800$ K, $\log(g) = 4.5$ dex, $[\rm Fe/H] = -2$ dex) gives valid estimates of RV for the full [Fe/H] range. We compute the cross-correlation function for all RV values and fit a parabola to 20 points around the maximum value of the cross-correlation function. Then we apply the Doppler-shift to the observed spectrum using the velocity value at the position of the peak of the parabola. Since cross-correlation can incur small errors due to step size/template choice, we later fit for residual shift in range $\pm\,2\,{\rm km\,s^{-1}}$.

2.2.4 Model atmospheres and synthetic spectra

The grids of LTE and NLTE synthetic spectra are computed using the new online spectrum synthesis tool `http://nlte.mpia.de`. The model atmospheres are 1D plane-parallel hydrostatic LTE models taken from the MAFAGS-OS grid (Grupp 2004a,b). For the NLTE grid we first compute the NLTE atomic number densities for Mg (Bergemann et al. 2017), Ti (Bergemann 2011), Fe (Bergemann et al. 2012) and Mn (Bergemann, M. & Gehren, T. 2008) using the DETAIL statistical equilibrium (SE) code (Butler & Giddings 1985). These are then fed into the SIU (Reetz 1991) radiative transfer (RT) and spectrum synthesis code. In total, 626 spectral lines of Mg I, Ti I, Fe I and Mn I are modelled in NLTE for the NLTE grid, while for the LTE grid these lines are modelled with default LTE atomic level populations. Our approach is conceptually similar to Buder et al. (2018a), but we employ different SE and RT codes. We have chosen to use the MAFAGS-OS atmosphere grids, because these are internally consistent with DETAIL and SIU. In particular, the latter codes adopt the atomic and molecular partial pressures and partition functions that are supplied with the MAFAGS-OS models.

We compute 20 000 spectral models with $T_{\rm eff}$ uniformly distributed in the range from 4000 to 7000 K and log(g)s in the range from 1.0 to 5.0 dex. Metallicity[5], [Fe/H], is uniformly distributed in the range from $[\rm Fe/H] = -2.6$ to 0.5 dex. We also allow for random variations in the rations of the magnesium, titanium, manganese to iron: [Mg/Fe], [Ti/Fe] from -0.4 to 0.8 dex and [Mn/Fe] from -0.8 to 0.4 dex. The abundances of other chemical elements are assumed to be solar and follow the iron abundance [Fe/H]. In the metal-poor regime ($[\rm Fe/H] < -1$ dex), some elements (like important opacity contributors C and O) can be significantly enhanced relative to the solar values. Therefore, we computed several metal-poor synthetic spectra using a 0.5 dex enhancement of C and O abundances and found that there is no impact

---

[5] Hereafter, the abundance of iron [Fe/H], is used as a proxy for metallicity.

on the spectral models. Micro-turbulence varies from 0.6 to 2.0 $\mathrm{km\,s^{-1}}$, in line with high-resolution studies of FGK stars (e.g. Ruchti et al. 2013). The detailed solar abundances assumed in the MAFAGS-OS grids are reported in Grupp (2004a). For the elements treated in NLTE, we adopt $\log A(\mathrm{Mg})_\odot = 7.58$ dex, $\log A(\mathrm{Ti})_\odot = 4.94$ dex, $\log A(\mathrm{Mn})_\odot = 5.53$ dex and $\log A(\mathrm{Fe})_\odot = 7.50$ dex (meteoritic values from Grevesse & Sauval 1998).

The widths of spectral lines in the observed spectra depend on many effects, such as the properties of the instrument, turbulence in stellar atmospheres, and stellar rotation (Gray 2005). However, it is not possible to separate these effects at the resolution of the Giraffe spectra. Hence, the macroturbulence, V_{mac}, and the projected rotation velocity, $V\sin$ i, are dealt with by smoothing the model spectra with a Gaussian kernel, which corresponds to a characteristic velocity V_{broad} in the range from 5.0 to 25.0 $\mathrm{km\,s^{-1}}$ that encompasses the typical values of V_{mac} and $V\sin$ i reported for FGK stars (Gray 2005; Jofré et al. 2015). After that, the synthetic spectra are degraded to the resolution of the HR10 setup by convolving them with an instrumental profile (Section 2.2.2) and are re-sampled onto the observed spectrum wavelength grid using the sampling of 20 wavelength points per Å.

2.2.5 The Payne code

The data-model comparison is not performed directly. Instead, we use *the Payne* code to interpolate in the grid of synthetic spectra.

The approach consists of two stages: the training (model building) and the test (data fitting) steps. In the training step, we build a *Payne* model using a set of pre-computed LTE and NLTE stellar spectra. We approximate the variation of the flux using an artificial neural network (ANN). In the test step, χ^2 minimisation is employed to find the best-fit stellar parameters and abundances by comparing the model spectra to the observations. In what follows, we describe the key details of the method. For more details on the algorithm, we refer the reader to Ting et al. (2018).

The conceptual idea of the code is simple. We employ a simple ANN that consists of several fully connected layers of neurons: an input layer, two hidden layers, and an output layer. The input data are given by a set of stellar parameters (hereafter, labels) T_{eff}, log(g), V_{mic}, V_{broad}, [Fe/H], [Mg/Fe], [Ti/Fe], and [Mn/Fe]. The output data comprise the normalised flux values tabulated on a wavelength grid, as a function of the input labels. Three hundred neurons in each hidden layer apply a weight and an offset to the output from the previous layer, and these outputs are activated using a $ReLU(z) = \max(z, 0)$ function for the first layer and a sigmoid function $s(z) = (1 + e^{-z})^{-1}$ for the second layer. A subset of the pre-computed spectral grid (that is 15 000 synthetic spectra) is used to train the ANN, whereby the weights and the offsets are adjusted to the optimal values. This subset is referred to as a *training set*. We train the neural networks by minimising the L^2 loss. In other words, we compute a minimal sum of the Euclidean distances between the target ab-initio flux from the training set and the flux predicted by the model at each wavelength point. We use cross-validation with the remaining set of 5000 spectra, which are referred to as a *cross-validation set* to prevent over-fitting. This requires optimal values of the ANN to decrease L^2 loss also for the *cross-validation set*, which is not directly used during training. Together, the ANN layers act like a function that predicts a flux spectrum for a set of given labels. The main difference of the current implementation of *Payne* with respect to the one in Ting et al. (2018) is that we use only one ANN to represent the full stellar spectrum. In our realisation[6] an ANN can exploit information from the adjacent pixels, while previously each individual pixel was trained separately. A synthetic spectrum is generated at arbitrary points in stellar parameter space within the domain of the training grid and is compared to the observed spectrum. A standard χ^2 minimisation is used to compute the likelihood of the fit and, hence, to find the stellar parameters that best characterise the observed spectrum. We also allow for a small Doppler shift, $\pm$ 2 $\mathrm{km\,s^{-1}}$, on top of the RV from cross-correlation, to optimise the spectral fit.

The continuum normalisation of the observed spectra is performed during the χ^2 minimisation. We search for the coefficients of a linear combination of the first ten Chebyshev polynomials, which represents a function that fits the shape of the continuum, using the full observed spectrum. A synthetic spectrum is then multiplied with this function.

In total, for each observed spectrum, we optimise 19 free parameters: one Doppler shift, eight spectral labels and ten coefficients of Chebyshev polynomials. The abundances of individual elements are derived simultaneously with other stellar parameters via the full spectral fitting process. We also employed the classical method of fitting separately each spectral line using line masks. However, this method delivers less precise abundances, as gauged by the star-to-star scatter, hence, we do not use the line masks in the final abundance analysis.

Following the result in Bergemann (2011) which strongly recommended to use only Ti II lines in abundance analysis, we masked out all Ti I lines. We note, however, that we did not include NLTE calculations for Ti II, as the NLTE effects

---

[6] as it is now implemented in the Github version: `https://github.com/tingyuansen/The_Payne`.

on this ion are very small in the metallicity regime of our sample (Bergemann 2011). Hence, the difference between our LTE and NLTE Ti abundance reflects only an indirect effect of NLTE on stellar parameters.

2.2.6 Internal accuracy of the method

We verify the internal accuracy of the method by subjecting it to tests similar to those employed by Ting et al. (2018).

First, we compare the interpolated synthetic spectra to the original models from the cross-validation sample. In this case we explore how well *the Payne* can generate new spectrum. The median interpolation error of the flux across 5000 models is $\leq 10^{-3}$, that is, within 0.1%. We also find that larger errors occur for cooler stars, because there are many more spectral features. This result suggests that interpolation is more accurate than the typical S/N of observed spectrum.

Second, we test how well we can recover original labels from the model, through χ^2 minimisation. In this case we apply random Doppler shift, multiply the model spectrum by a random combination of the first ten Chebyshev polynomials, that represent the continuum level and add noise. Such a modified model serves as a fair representation of a real observed spectrum. The tests are performed for the noiseless models and the models degraded to a S/N of 90 Å^{-1} and 224 Å^{-1}. This range of S/N brackets the typical values of the observed HR10 spectra, with the majority of the spectra sampling the S/N range of 150-200 Å^{-1}. The typical S/N of the spectra of the benchmark stars is ~ 200 Å^{-1}.

Table 2.2 presents the average differences between the input and the output stellar parameters for the cross-validation sample. The scatter is represented by one standard deviation. To facilitate the analysis, we group the results into three metallicity bins.

The results for the noiseless models with [Fe/H] in the range from -1.6 to 0.5 dex suggest high internal accuracy of the method. For the lower-metallicity models, there is a small bias and a larger dispersion in the residuals, because we have less spectral information in this regime. The bias is also marginal for the high-S/N spectra with S/N $= 224$ Å^{-1}, although the scatter in the output is increased compared to the noiseless models. Our analysis of the noisy models, S/N $= 90$ Å^{-1}, yields acceptable results for the metal-rich and moderately metal-poor stars with [Fe/H] $\gtrapprox -1.6$ dex. On the other hand, the most metal-poor noisy spectra are not fitted well. Despite a modest bias in T_{eff}, the dispersion of $\log g$ and the abundance ratios is very large and may require a different approach to obtain high-precision abundances in this regime. According to this test, good Mn abundances (better than ∼ 0.1 dex) can be derived only for metal-rich stars.

These tests illustrate only the internal accuracy of *the Payne* model reconstruction and, hence, set the minimum uncertainty on the parameters determined by our method, regardless of the training sample, its physical properties and completeness. The analysis of observed data may result in a larger uncertainty, as various other effects, such as the physical complexity of the model atmospheres and synthetic spectra and properties of the observed data (data reduction effects etc.), will contribute to the total uncertainties. We test this in the next section by analysing the Gaia-ESO benchmark stars.

Table 2.1:: Gaia benchmark stars parameters from NLTE fit (for the max S/N spectrum) and reference study (Jofré et al. 2015), except where noted.

Star	$T_{\rm eff}$,K	log(g),dex	[Fe/H],dex	$V_{\rm mic}$, $\rm km\,s^{-1}$
	fit, ref	fit, ref	fit, ref	fit, ref
HD107328	4384, 4496 ± 59	1.90, 2.09 ± 0.14	-0.60, -0.38 ± 0.16	1.71, 1.65 ± 0.26
HD220009	4336, 4275 ± 54	1.86, 1.47 ± 0.14	-0.79, -0.79 ± 0.13	1.42, 1.49 ± 0.14
ksiHya	5045, 5044 ± 38	3.01, 2.87 ± 0.02	-0.05, 0.11 ± 0.20	1.54, 1.40 ± 0.32
muLeo	4462, 4474 ± 60	2.45, 2.51 ± 0.09	0.01, 0.20 ± 0.15	1.54, 1.28 ± 0.26
HD122563	4771, 4636 ± 37[1]	1.29, 1.42 ± 0.01[2]	-2.56, -2.52 ± 0.11[3]	2.53, 1.92 ± 0.11
HD140283	5888, 5787 ± 48[1]	3.63, 3.57 ± 0.12	-2.39, -2.34 ± 0.03[3]	2.16, 1.56 ± 0.20
delEri	5006, 4954 ± 26	3.61, 3.75 ± 0.02	-0.00, 0.01 ± 0.05	1.15, 1.10 ± 0.22
epsFor	5070, 5123 ± 78	3.28, 3.52 ± 0.07	-0.65, -0.65 ± 0.10	1.14, 1.04 ± 0.13
18Sco	5838, 5810 ± 80	4.32, 4.44 ± 0.03	0.02, -0.02 ± 0.03	1.27, 1.07 ± 0.20
alfCenB	5167, 5231 ± 20	4.33, 4.53 ± 0.03	0.14, 0.17 ± 0.10	1.06, 0.99 ± 0.31
muAra	5743, 5902 ± 66	4.05, 4.30 ± 0.03	0.22, 0.30 ± 0.13	1.32, 1.17 ± 0.13
betVir	6259, 6083 ± 41	4.06, 4.10 ± 0.02	0.18, 0.19 ± 0.07	1.51, 1.33 ± 0.09
epsEri	5079, 5076 ± 30	4.54, 4.60 ± 0.03	-0.14, -0.14 ± 0.06	1.11, 1.14 ± 0.05
etaBoo	6183, 6099 ± 28	3.84, 3.80 ± 0.02	0.27, 0.27 ± 0.08	1.52, 1.52 ± 0.19
HD22879	5907, 5868 ± 89	3.98, 4.27 ± 0.03	-0.80, -0.91 ± 0.05	1.24, 1.05 ± 0.19
HD49933	6718, 6635 ± 91	4.16, 4.20 ± 0.03	-0.36, -0.46 ± 0.08	1.51, 1.46 ± 0.35
HD84937	6481, 6356 ± 97	3.91, 4.15 ± 0.06	-2.00, -1.99 ± 0.02[3]	1.76, 1.39 ± 0.24
Procyon	6686, 6554 ± 84	3.91, 3.99 ± 0.02	0.03, -0.04 ± 0.08	1.83, 1.66 ± 0.11
tauCet	5349, 5414 ± 21	4.26, 4.49 ± 0.01	-0.52, -0.54 ± 0.03	1.00, 0.89 ± 0.28
<ref-fit>	-29 ± 88	0.09 ± 0.16	0.02 ± 0.09	-0.16 ± 0.18

Notes: In order to be consistent with our reference solar [Fe/H] scale, we subtracted 0.05 dex from Jofré et al. (2015) and 0.03 dex from Amarsi et al. (2016) metallicities. References:(1)Karovicova et al. (2018), (2)Creevey et al. (2019), (3) Amarsi et al. (2016).

Table 2.2:: Internal errors of label's recovery by *the Payne* see Section 2.2.6 for details.

S/N Å^{-1}	[Fe/H] dex	$\Delta T_{\rm eff}$ 1000 K	$\Delta\log(g)$ dex	$\Delta V_{\rm mic}$ km s^{-1}	$\Delta V_{\rm broad}$ 10 km s^{-1}	Δ[Fe/H] dex	Δ[Mg/Fe] dex	Δ[Ti/Fe] dex	Δ[Mn/Fe] dex
90	-2.6:-1.6	0.00±0.27	-0.05±0.56	-0.10±0.77	-0.01±0.29	-0.00±0.18	0.01±0.17	-0.02±0.34	-0.01±0.64
	-1.6:-0.6	0.01±0.12	0.00±0.21	0.01±0.26	-0.00±0.09	0.01±0.07	0.00±0.10	-0.01±0.13	-0.01±0.37
	-0.6:0.5	0.01±0.07	0.00±0.12	0.00±0.10	-0.00±0.05	0.01±0.06	-0.00±0.09	-0.00±0.07	-0.00±0.11
224	-2.6:-1.6	-0.00±0.11	-0.04±0.25	-0.00±0.41	0.01±0.13	-0.00±0.07	0.01±0.07	-0.01±0.17	-0.03±0.55
	-1.6:-0.6	-0.00±0.05	-0.00±0.08	-0.00±0.09	-0.00±0.04	-0.00±0.03	0.00±0.05	-0.00±0.05	-0.03±0.25
	-0.6:0.5	0.00±0.03	0.00±0.06	0.00±0.05	-0.00±0.02	0.00±0.04	0.00±0.04	0.00±0.03	0.00±0.05
no	-2.6:-1.6	-0.00±0.02	-0.01±0.06	-0.01±0.15	0.00±0.02	-0.00±0.02	-0.00±0.03	-0.00±0.04	-0.01±0.21
noise	-1.6:-0.6	-0.00±0.01	0.00±0.03	0.00±0.03	0.00±0.01	0.00±0.01	-0.00±0.02	0.00±0.02	0.00±0.05
	-0.6:0.5	0.00±0.01	0.00±0.05	0.00±0.03	0.00±0.01	0.00±0.05	-0.00±0.04	0.00±0.01	0.00±0.03

2.3 Results

2.3.1 Gaia-ESO benchmark stars

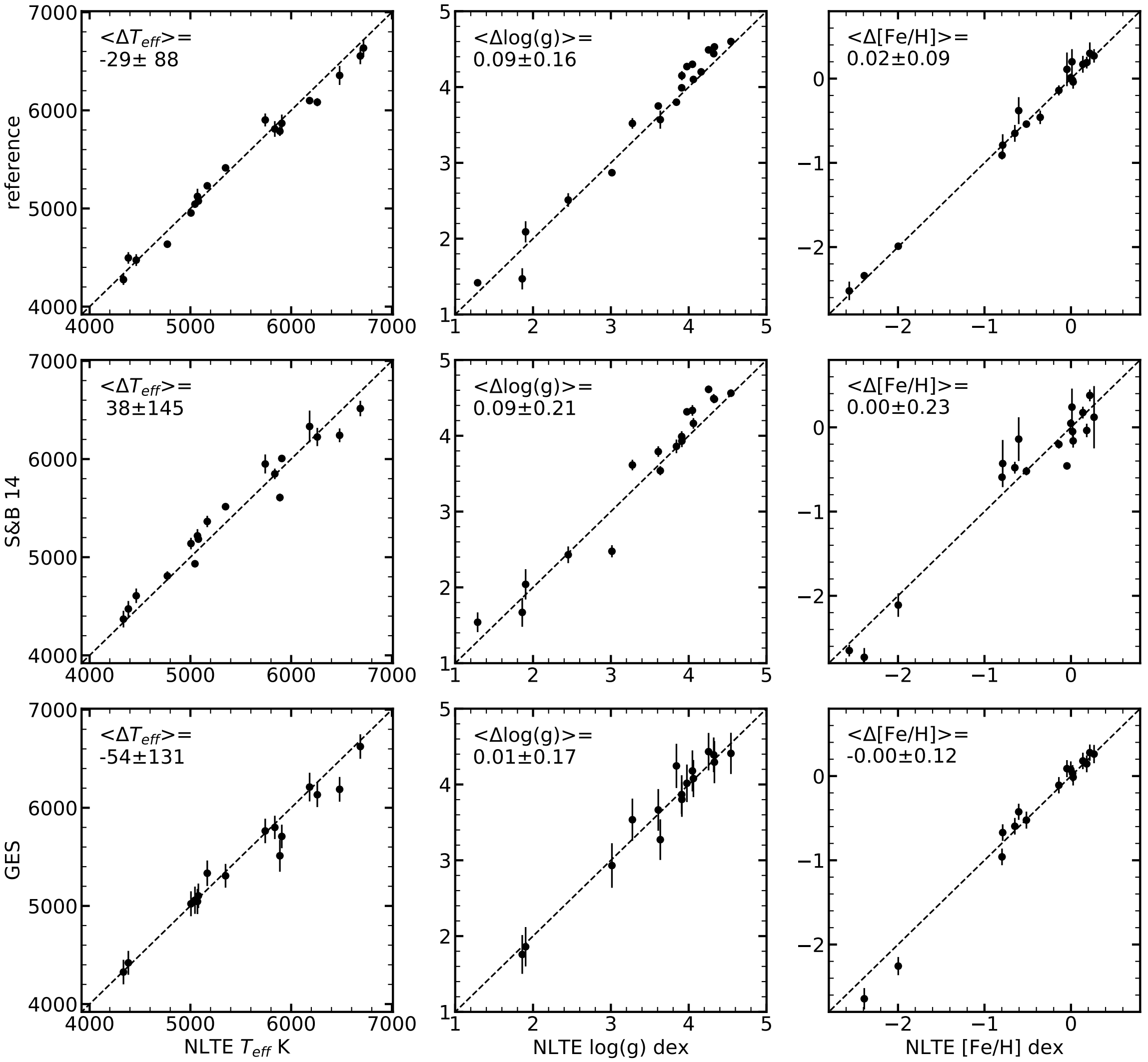

Figure 2.2: Our NLTE spectroscopic estimates for the benchmark stars compared with the literature. The top panels shows the reference stellar parameters and their uncertainties from Jofré et al. (2015); Karovicova et al. (2018); Amarsi et al. (2016). In the middle and bottom panels, we show our values against the results from Schönrich & Bergemann (2014) and GES catalogue Smiljanic et al. (2014), respectively. The mean offset and scatter are given in the legend of each plot.

Our results for the Gaia-ESO benchmark stars are shown in Fig. 2.2 and Fig. 2.3. Fig. 2.2 compares our NLTE stellar parameters with the values from Jofré et al. (2015), Schönrich & Bergemann (2014), and with the Gaia-ESO DR3 catalogue (GES) (Smiljanic et al. 2014). In Jofré et al. (2015), T_{eff} estimates were determined from photometry and interferometry, log(g) from parallaxes and astroseismology. [Fe/H] estimates were obtained from the NLTE analysis of Fe lines in the high-resolution spectra taken with the UVES, NARVAL and HARPS spectrographs (Blanco-Cuaresma et al. 2014). In order to be consistent with our reference solar [Fe/H] scale, we subtracted 0.05 dex from Jofre and GES metallicities, as they are based on the Grevesse et al. (2007) metallicity scale ($\log A(\text{Fe})_\odot = 7.45$ dex). Likewise, we subtracted 0.03 dex from Amarsi et al. (2016) metallicities, as they employ $\log A(\text{Fe})_\odot = 7.47$ dex. The estimates of stellar parameters in Schönrich & Bergemann (2014) are derived from the full Bayesian approach by solving for the posterior in the multi-dimensional parameter space, including photometry, high-resolution spectra, parallaxes, and evolutionary constraints. The estimates of stellar parameters in the Gaia-ESO DR3 catalogue rely on the high-resolution (UVES at VLT) spectroscopy only.

Figure 2.2 suggests that the agreement of our NLTE results with the literature studies is very good. The differences with Jofré et al. (2015) are of the order -46±119 K in T_{eff}, 0.10±0.17 dex in log(g) and 0.01±0.09 dex in [Fe/H] across the full parameter space, and they also compare favourably with the results obtained by Schönrich & Bergemann (2014) and reported in Gaia-ESO DR3 catalogue. Results for individual stars are listed in Table 2.1. Since DR3 catalogue data versus Jofré et al. (2015) data have comparable differences (15±90 K in T_{eff}, 0.08±0.20 dex in log(g) and 0.01±0.09 dex in [Fe/H]) we can say that our analysis achieve internal precision of Gaia-ESO.

The scatter is slightly larger for the metal-poor stars. This could be the consequence of the limited coverage of the training set. In particular, the two very metal-poor evolved stars HD 122563 and HD 140283 are located next to the low-metallicity edge of our training grid. Since the Gaia-ESO benchmark star sample contains only three stars with $[\text{Fe/H}] < -1$, no reliable statistics can be drawn on the success of our approach in this regime of stellar parameter. Also the sample of RGB stars is very small and contains only five objects with $\log(g) < 3$ dex. We address the performance of our method for low-gravity stars in the next section, by analysing a set of open and globular clusters that cover a large metallicity range, $-2.3 \lesssim [\text{Fe/H}] \lesssim -0.1$ dex, and provide a better sampling on the RGB.

Fig. 2.3 illustrates the performance of our method for the spectra taken at different exposure times. We have chosen four stars representative of our calibration sample: HD 107328 - a moderately metal-poor giant ($T_{\text{eff}} = 4384$ K, $\log(g) = 1.90$ dex, and $[\text{Fe/H}]_{\text{NLTE}} = -0.60$ dex), ξ *Hya* - a metal-rich subgiant

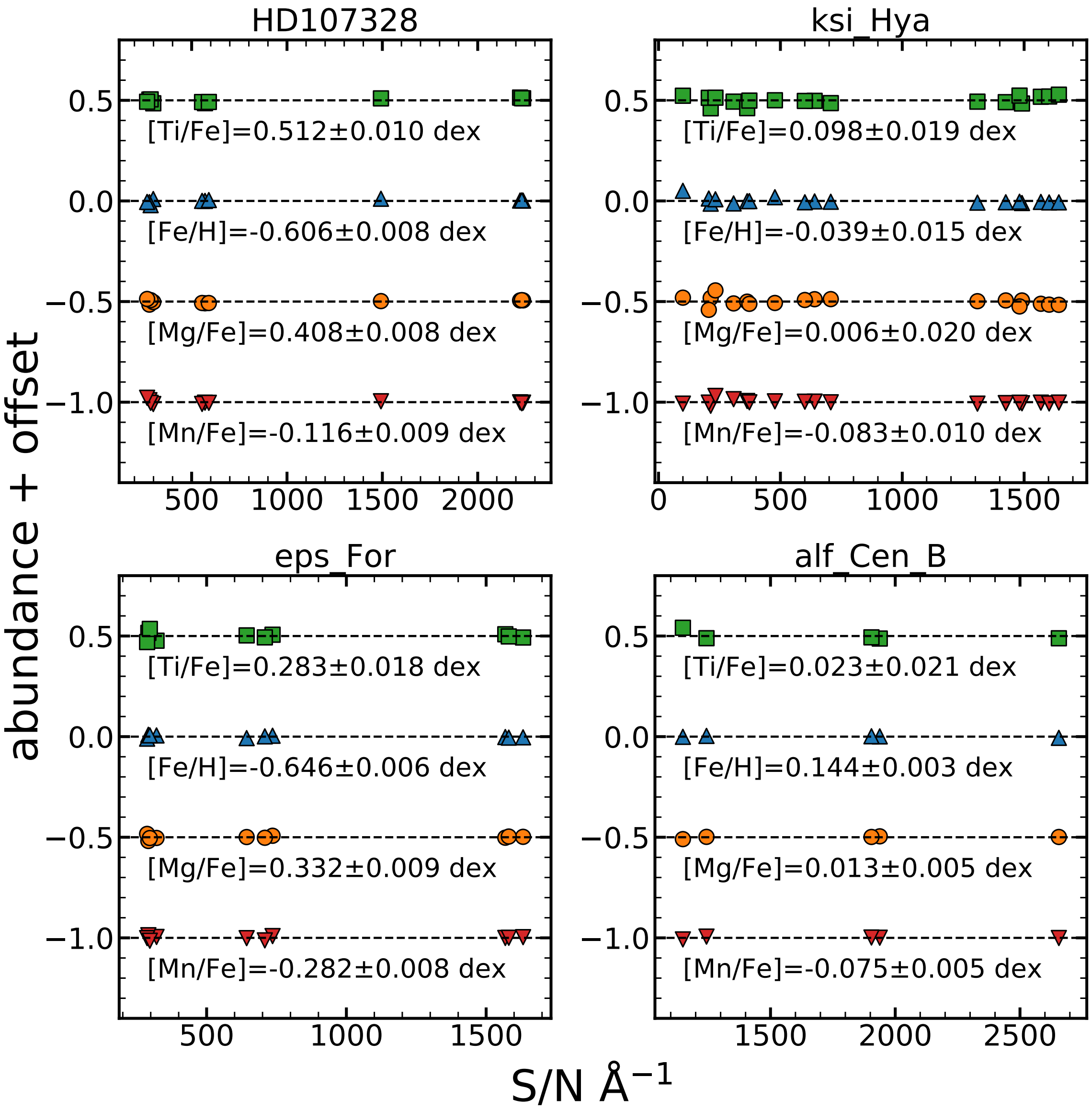

Figure 2.3: NLTE elemental abundances derived from the spectra taken at different exposure times. Abundances determined at S/N = 100 Å^{-1} appear just as precise as those at S/N > 2500 Å^{-1}. See section 2.3.1

($T_{\text{eff}} = 5045$ K, log(g) = 3.01 dex, and $[\text{Fe/H}]_{\text{NLTE}} = -0.05$ dex), ϵ *For* - a moderately metal-poor subgiant ($T_{\text{eff}} = 5070$ K, log(g) = 3.28 dex, and $[\text{Fe/H}]_{\text{NLTE}} = -0.65$ dex), and α *Cen* B - a metal-rich dwarf ($T_{\text{eff}} = 5167$ K, log(g) = 4.33 dex, and $[\text{Fe/H}]_{\text{NLTE}} = 0.14$ dex). These stars have been observed with different exposure times, corresponding to the S/N ratios of 90 to 2600 Å^{-1} that allows us to validate the differential precision of the adopted model. We do not detect any evidence of a systematic bias that depends on the data quality. In particular, the mean difference (taken as one standard deviation) between abundances of Fe, Mg, and Ti obtained from the S/N = 90 $\mathrm{\AA}^{-1}$ spectra and those obtained from the highest-quality data (S/N $\sim$ 2600 $\mathrm{\AA}^{-1}$) is not larger than 0.02 dex for any of these stars, and is less than 0.01 dex for the majority. We hence conclude that our results are not very sensitive to the quality of the observed data for a wide range of S/N ratios.

2.3.2 Open and globular clusters

Sample selection

Our dataset includes two open clusters and 11 globular clusters. The cluster members are chosen using the central coordinates and the RV estimates from the SIMBAD[7] database listed in Table 2.3. We select only stars with an RV within 5 $\mathrm{km\,s^{-1}}$ from the cluster median[8], for the open clusters. For the globular clusters, we assume a 1σ RV dispersion and the central values from Pancino et al. (2017). We also apply a 2σ clipping around the median in metallicity, and employ proper motions from Gaia DR2 (Gaia Collaboration et al. 2018) to exclude stars outside the 2σ range from the median proper motion of each cluster. It is common to use distances to compute astrometric gravities (e.g. Ruchti et al. 2013). However, the majority of clusters in our sample are located at heliocentric distances $d_\odot$ of > 2 kpc, where parallaxes are very uncertain. Besides, poorly constrained differential extinction in some clusters limits the applicability of standard relations, to derive log(g) from distances and photometric magnitudes. We, hence, refrain from using the Gaia DR2 parallaxes to compute surface gravities. Instead, we compare our results with the isochrones computed using our estimates of metallicities and the ages adopted from literature studies, in particular, from Kruijssen et al. (2018) for GCs and from the WEBDA database[9] for open clusters. For most clusters, the ages are derived from the colour-magnitude diagram turn-off or horizontal branch fits. Hence, also this comparison can be performed only with the caveat that the turn-off or horizontal branch ages are not a fundamental reference, but are model-dependent and may not be fully unbiased.

---

[7] `http://simbad.u-strasbg.fr/simbad/`

[8] The median is used because it is less sensitive to outliers.

[9] `https://www.univie.ac.at/webda/`

Table 2.3:: The cluster parameters: coordinates and radial velocities from SIMBAD database, ages and [Fe/H] from Kruijssen et al. (2018) for globular clusters (gc) and WEBDA database for open clusters (oc), distances and E(B-V) are from Harris (gc) or WEBDA (oc) databases, except where noted.

Cluster	α deg	δ deg	$d_\odot$ kpc	E(B-V) mag	<RV> km s^{-1}	Age Gyr	[Fe/H] dex
NGC 3532 (oc)	166.4125	-58.7533	0.484^c	0.034^c	4.31	0.31	-0.01
NGC 5927 (gc)	232.0029	-50.6730	7.7	0.45	-100.5	11.89	-0.48
NGC 2243 (oc)	97.3917	-31.2833	4.46	0.05	59.8	3.8^d	-0.57^d
NGC 104 (gc)	6.0224	-72.0815	4.45^d	0.04	-18.7	12.52	-0.75
NGC 1851 (gc)	78.5281	-40.0465	12.1	0.02	320.9	10.49	-1.1
NGC 2808 (gc)	138.0129	-64.8635	9.6	0.22	102.79	10.9	-1.14
NGC 362 (gc)	15.8094	-70.8488	8.54^a	0.05	222.95	10.87	-1.23
M 2 (gc)	323.3626	-0.8233	11.5	0.06	-6.7	12.01	-1.52
NGC 6752 (gc)	287.7170	-59.9846	4.0	0.02	-27.4	12.26	-1.43
NGC 1904 (gc)	81.0441	-24.5242	12.9	0.01	205.78	11.14	-1.37
NGC 4833 (gc)	194.8913	-70.8765	6.6	0.32	201.1	12.68	-1.97
NGC 4372 (gc)	186.4393	-72.6591	5.8	0.3..0.8^b	72.6	12.54	-1.88
M 15 (gc)	322.4930	12.1670	10.4	0.10	-106.6	12.98	-2.25

Notes. (a)- Chen et al. (2018),(b)-Kacharov et al. (2014),(c)-Fritzewski et al. (2019),(d)-Anthony-Twarog et al. (2005)

Stellar parameters and comparison with the isochrones

The majority of the globular clusters are distant and are represented by RGB stars in our sample. Main-sequence stars are observed only in the nearby metal-rich open cluster NGC 3532. Hence, in what follows, the discussion will mainly focus on the RGB population across a wide range of metallicities, from -0.5 (NGC 5927) to -2.3 dex (M 15).

In Fig. 2.4, we compare NLTE and LTE stellar parameters as a function of NLTE metallicity. Since most stars, within a cluster, are in the same evolutionary stage (lower or upper RGB), we have chosen to show only the mean NLTE-LTE differences, averaged over all stars in a given cluster. This is sufficient to illustrate the key result: the differences between NLTE and LTE $T_{\rm eff}$, $\log g$, and [Fe/H] vary in lockstep with metallicity, that reflects the NLTE effects in the formation of the Fe I and Ti I spectral lines, which are ubiquitous in HR 10. It is furthermore important, although not unexpected, that below [Fe/H] ~ -1 dex the changes are nearly linear, consistent with our earlier theoretical estimates (Lind et al. 2012) and with the analysis of the metal-poor field stars in the Milky Way (Ruchti et al. 2013). The

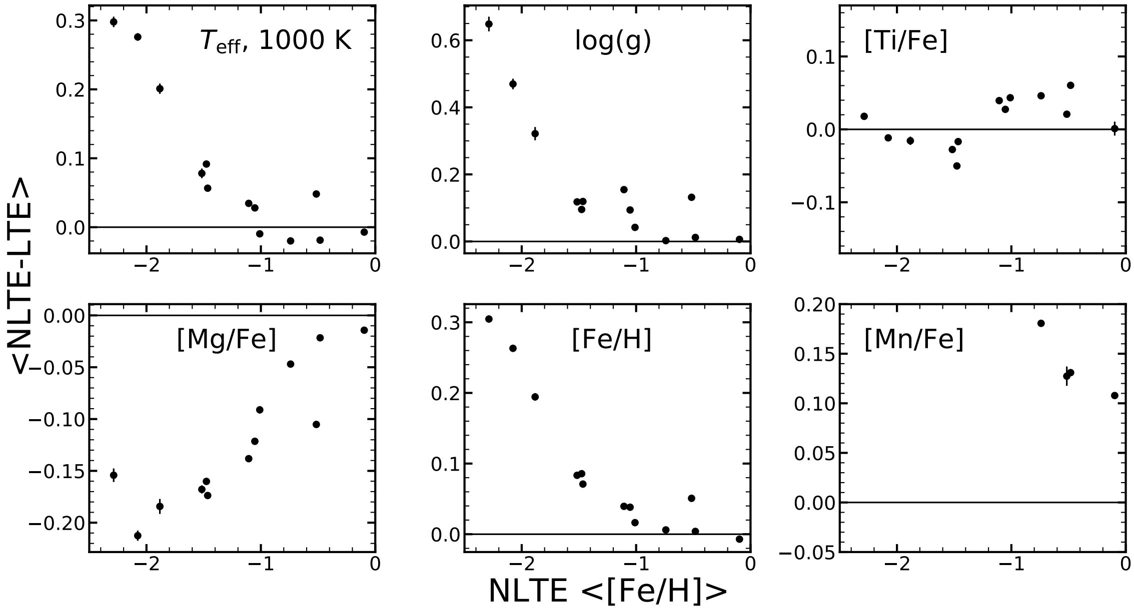

Figure 2.4: The mean differences between NLTE and LTE parameters for stars within each cluster against NLTE metallicity. For [Mn/Fe] only clusters with [Fe/H] $>$ -1 dex are shown. See section 2.3.2 for details.

NLTE effect is most striking at [Fe/H] $\lesssim -2$, where we find the difference of ~ 300 K in $T_{\rm eff}$, ~ 0.6 dex in $\log g$, and ~ 0.3 dex in [Fe/H]. The [Mg/Fe] ratios tend to be lower in NLTE that reflects negative NLTE abundance corrections for the only Mg line in HR10 (Mg I 5528 Å), which is consistent with earlier studies (Osorio et al. 2015; Bergemann et al. 2017). The upturn in [Mg/Fe] at [Fe/H] ~ -2 dex is real and it is caused by the change of the dominant NLTE effect at this metallicity. At higher [Fe/H], strong line scattering and photon loss, and, hence, the deviations of the source function from the Planck function, play an important role in the statistical equilibrium of the ion. However, in the metal-poor models, [Fe/H] $\lesssim -2$ dex, it is the over-ionisation driven by hard UV radiation field that acts on the line opacity and thereby counteracts the NLTE effects on the source function. We have masked out all Ti I lines (see Section 2.2.5), so differences in [Ti/Fe] are small $\lesssim 0.06$ dex and represent indirect NLTE effects on other stellar parameters. The difference in [Mn/Fe] is shown only for few metal rich clusters, and it is increasing to lower [Fe/H].

Fig. 2.5 and Fig. 2.6 show our NLTE/LTE results respectively for the 12 clusters in the $T_{\rm eff}$ - $\log g$ plane. We also overlay the PARSEC (Marigo et al. 2017) and Victoria-Regina (VandenBerg et al. 2014, hereafter, VR) isochrones to facilitate the analysis of the evolutionary stages probed by the stellar sample. The VR

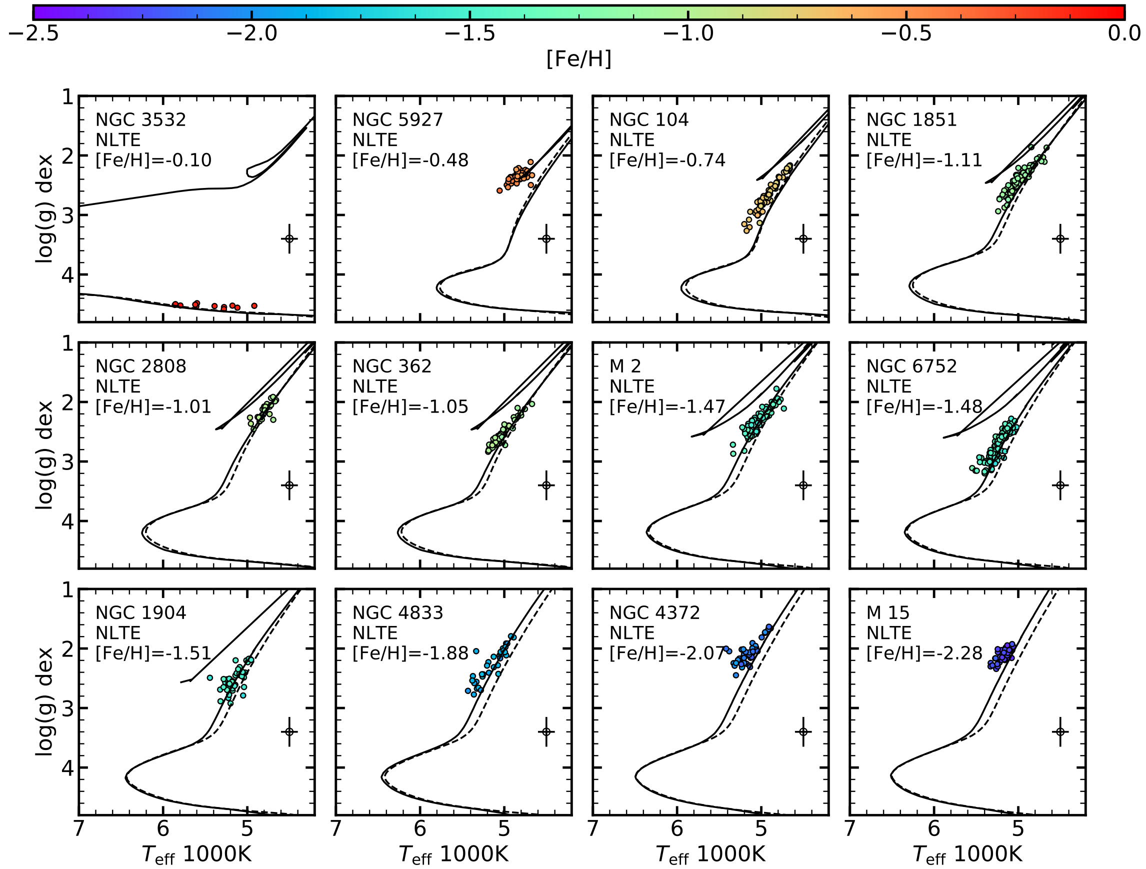

Figure 2.5: NLTE spectroscopic parameters compared with the PARSEC (solid line) and Victoria-Regina (dashed line) isochrones (Marigo et al. 2017; VandenBerg et al. 2014). The colour of the points indicates their [Fe/H]. Note different target selection for NGC 5927, where mostly stars at horizontal branch were observed.

isochrones assume the He abundance of $Y = 0.26$ and an α-enhancement, as given by our measurements of [Mg/Fe]. The PARSEC isochrones are computed using an effective metallicity (Aldo Serenelly, priv. comm.)

$$Z = Z_0(0.659 f_\alpha + 0.341), \tag{2.2}$$

where $Z_0 = 10^{\rm [Fe/H]}$ and $f_\alpha = 10^{\rm [Mg/Fe]}$. The error of the spectroscopic estimates is shown in the inset and it represents the typical uncertainty of our analysis ($\Delta(T_{\rm eff}) = 150$ K and $\Delta(\log(g)) = 0.3$ dex based on Gaia-ESO benchmark stars analysis). The star-to-star scatter in the $T_{\rm eff}$-log(g) plane is very small, and, within the uncertainties, consistent with the isochrones.

Surprisingly, both NLTE and LTE spectroscopic parameters agree well with the isochrones computed for the corresponding [Fe/H], despite the large differences

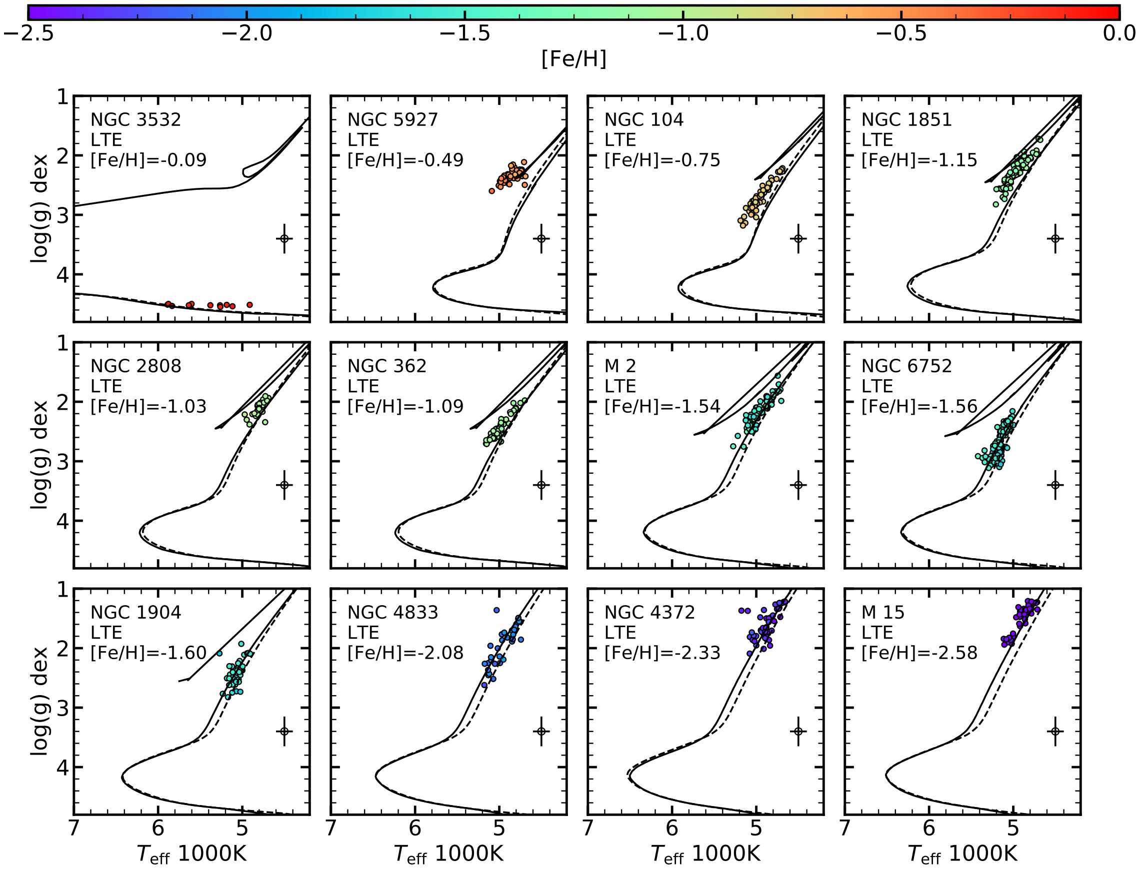

Figure 2.6: LTE spectroscopic parameters compared with the PARSEC (solid line) and Victoria-Regina (dashed line) isochrones (Marigo et al. 2017; VandenBerg et al. 2014). The colour of the points indicates their [Fe/H]. Note different target selection for NGC 5927, where mostly stars at horizontal branch were observed.

between NLTE and LTE parameters ($T_{\rm eff}$, $\log g$, [Fe/H], and [Mg/Fe]) especially at low metallicity. This would appear counter-intuitive, at a first glance, given the large offsets demonstrated in Fig. 2.4. However, this effect is, in fact, simply a result of the complex correlations in stellar parameters (as also extensively discussed in Ruchti et al. 2013): NLTE effects in the over-ionisation dominated species (such as Fe I, Ti I) significantly change the excitation and ionisation balance, such that the theoretical spectral lines tend to be weaker and a higher abundance would be inferred by comparing them to the observed spectra. Consequently, larger estimates of $T_{\rm eff}$, $\log g$, and [Fe/H] are expected from the NLTE modelling compared to LTE (see also Lind et al. 2012). The difference between NLTE and LTE [Fe/H] estimates is exactly the offset needed to match the higher (lower) $T_{\rm eff}$ and higher (lower) $\log g$ to the corresponding isochrone computed for the NLTE (LTE) metallicity and α-enhancement. This suggests that even large systematic errors in spectroscopic estimates may remain undetected in the $T_{\rm eff} - \log g$ plane, when spectroscopic values are gauged by comparing them with the isochrones.

In Figures 2.7, 2.8 we show example of spectral fits for two stars randomly selected from clusters sample and two metal-poor benchmark stars. Both LTE and NLTE model spectra match observed ones very well, having similar χ_r^2, while fit residuals mostly show noise and data reduction artefacts.

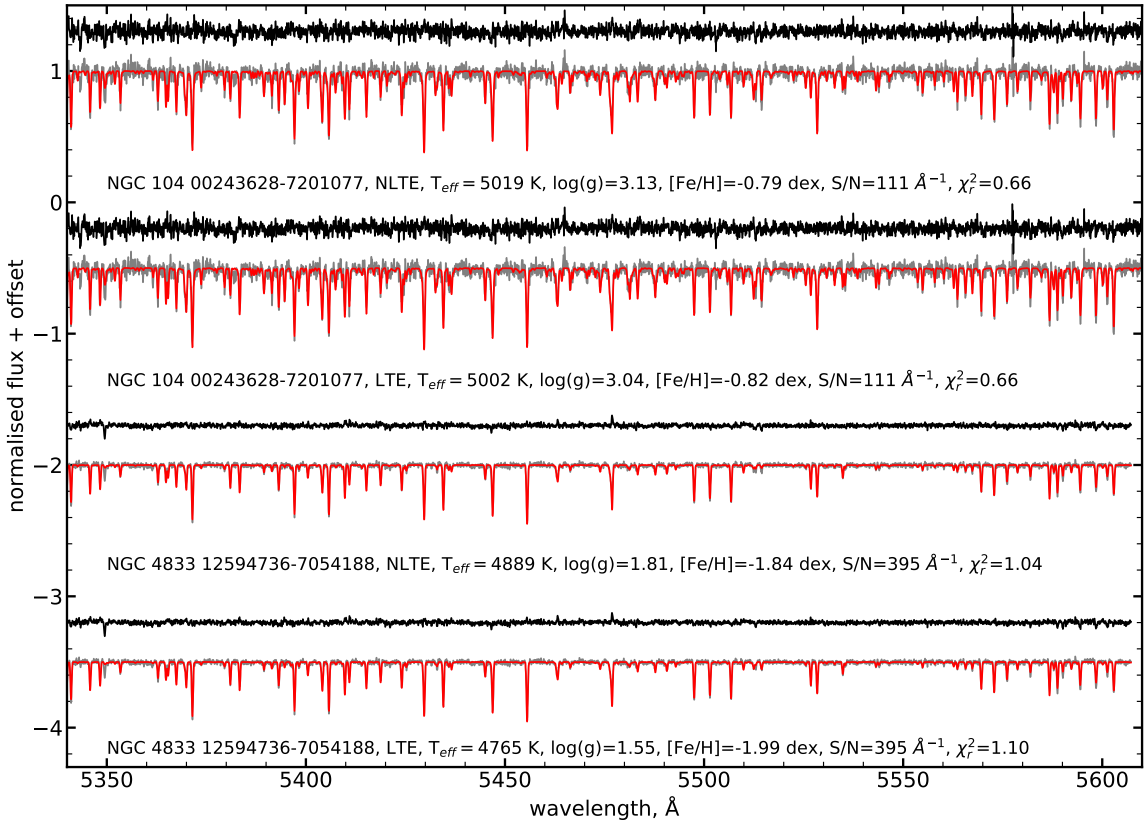

Figure 2.7: Example of NLTE/LTE spectral fit for two stars from cluster sample. Fitted spectra are shown as red lines in front of observed ones as gray lines, while fit residuals are shown 0.15 higher as black lines. Star names with derived $T_{\rm eff}$, log(g), [Fe/H], reduced χ^2 and S/N ratios are provided for each fit.

Our LTE and NLTE results show a slight tendency towards a hotter $T_{\rm eff}$ scale, which may appear more consistent with the PARSEC models. Yet, it might be premature to draw more specific conclusions on this matter, as we are aware of the imperfections of the stellar atmosphere and spectral model grids, such as an approximate treatment of convection, but also of the calibrations that are employed in the stellar evolution models (e.g. Fu et al. 2018)). At this stage, it appears to be sufficient to emphasize that our spectroscopic results are internally consistent,

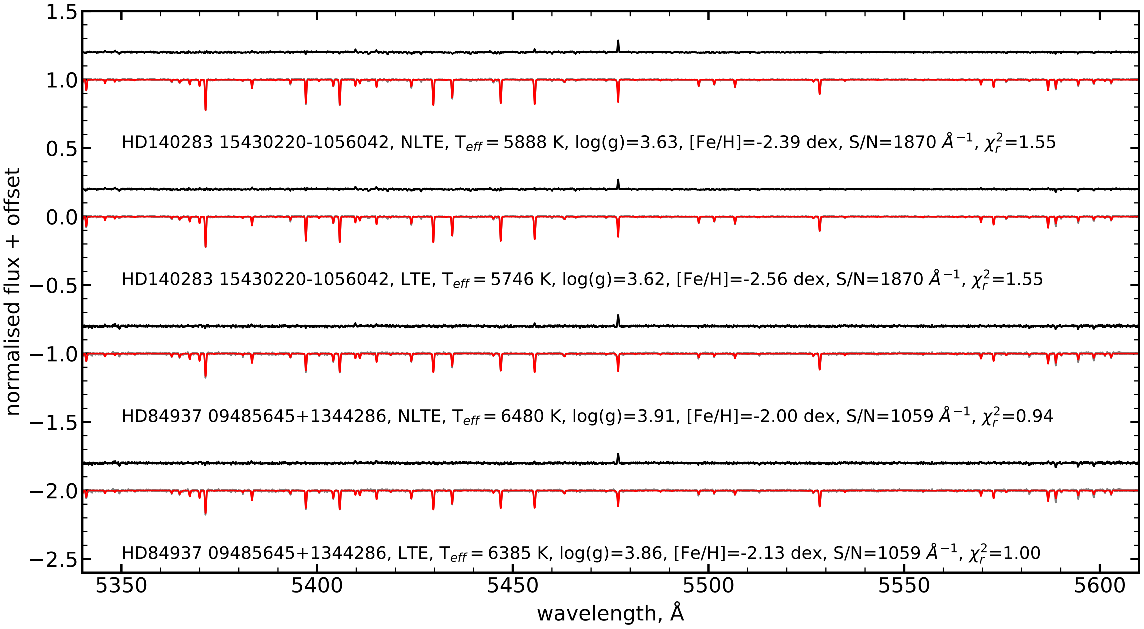

Figure 2.8: Example of NLTE/LTE spectral fit for two stars benchmark stars. Fitted spectra are shown as red lines in front of observed ones as gray lines, while fit residuals are shown 0.15 higher as black lines. Star names with derived $T_{\rm eff}$, log(g), [Fe/H], reduced χ^2 and S/N ratios are provided for each fit.

and allow predictive statements to be made on the astrophysical significance of the similarities and/or differences of chemical abundance patterns in the clusters.

Error estimates

To explore the sensitivity of the abundances to the uncertainties in stellar parameters, we use a method similar to the one employed in Bergemann et al. (2017). The standard errors are estimated by comparison with the independent stellar parameters for the benchmark stars (Section 2.3.1). These are $\pm\Delta T_{\rm eff} = 150$ K, $\pm\Delta \log(g) = 0.3$ dex and $\pm\Delta[{\rm Fe/H}] = 0.1$ dex. For $V_{\rm mic}$, we use the uncertainty of $\pm$ 0.2 km s^{-1}. We perturb one parameter at a time by its standard error, and re-determine the abundance of an element, while keeping the parameter fixed during the χ^2 optimisation. We then compare the resulting abundance with the estimate obtained from the full solution, when all labels are solved for simultaneously. Table 2.4 presents the resulting uncertainties for five stars representative of the sample. These differences are added in quadrature and are used as a measure of the systematic error of abundances ΔX. The systematic errors derived using this procedure are typically within 0.10 to 0.15 dex (Table 2.4).

Table 2.4:: Sensitivity of abundance ratios to errors in atmospheric parameters.

star/parameter	Δ[Fe/H] dex	Δ[Mg/Fe] dex	Δ[Ti/Fe] dex
06291929-3125331 $T_{\rm eff}$=6689, log(g)=4.22, [Fe/H]=-0.52			
$T_{\rm eff}$ +150 K	0.08	-0.01	0.01
log(g) +0.3 dex	0.07	-0.06	0.08
[Fe/H] +0.1 dex	$\cdots$	-0.02	0.01
$V_{\rm mic}$ +0.2 km s^{-1}	0.01	0.02	-0.01
total	0.10	0.06	0.07
00225472-7203461 $T_{\rm eff}$=5146, log(g)=3.08, [Fe/H]=-0.75			
$T_{\rm eff}$ +150 K	0.11	-0.07	0.04
log(g) +0.3 dex	0.08	-0.10	0.08
[Fe/H] +0.1 dex	$\cdots$	-0.05	0.02
$V_{\rm mic}$ +0.2 km s^{-1}	-0.03	0.02	-0.04
total	0.14	0.14	0.10
00250332-7201108 $T_{\rm eff}$=4662, log(g)=2.21, [Fe/H]=-0.78			
$T_{\rm eff}$ +150 K	0.13	-0.08	0.03
log(g) +0.3 dex	0.08	-0.09	0.04
[Fe/H] +0.1 dex	$\cdots$	-0.04	-0.01
$V_{\rm mic}$ +0.2 km s^{-1}	-0.04	0.02	-0.02
total	0.16	0.12	0.05
21300747+1210115 $T_{\rm eff}$=5150, log(g)=1.99, [Fe/H]=-2.32			
$T_{\rm eff}$ +150 K	0.10	-0.05	-0.01
log(g) +0.3 dex	0.01	-0.01	0.10
[Fe/H] +0.1 dex	$\cdots$	-0.05	-0.03
$V_{\rm mic}$ +0.2 km s^{-1}	-0.04	0.02	-0.01
total	0.11	0.08	0.11
21295615+1210296 $T_{\rm eff}$=5329, log(g)=2.30, [Fe/H]=-2.26			
$T_{\rm eff}$ +150 K	0.10	-0.02	0.02
log(g) +0.3 dex	0.06	-0.01	0.06
[Fe/H] +0.1 dex	$\cdots$	-0.03	0.01
$V_{\rm mic}$ +0.2 km s^{-1}	0.06	-0.01	0.03
total	0.13	0.03	0.07

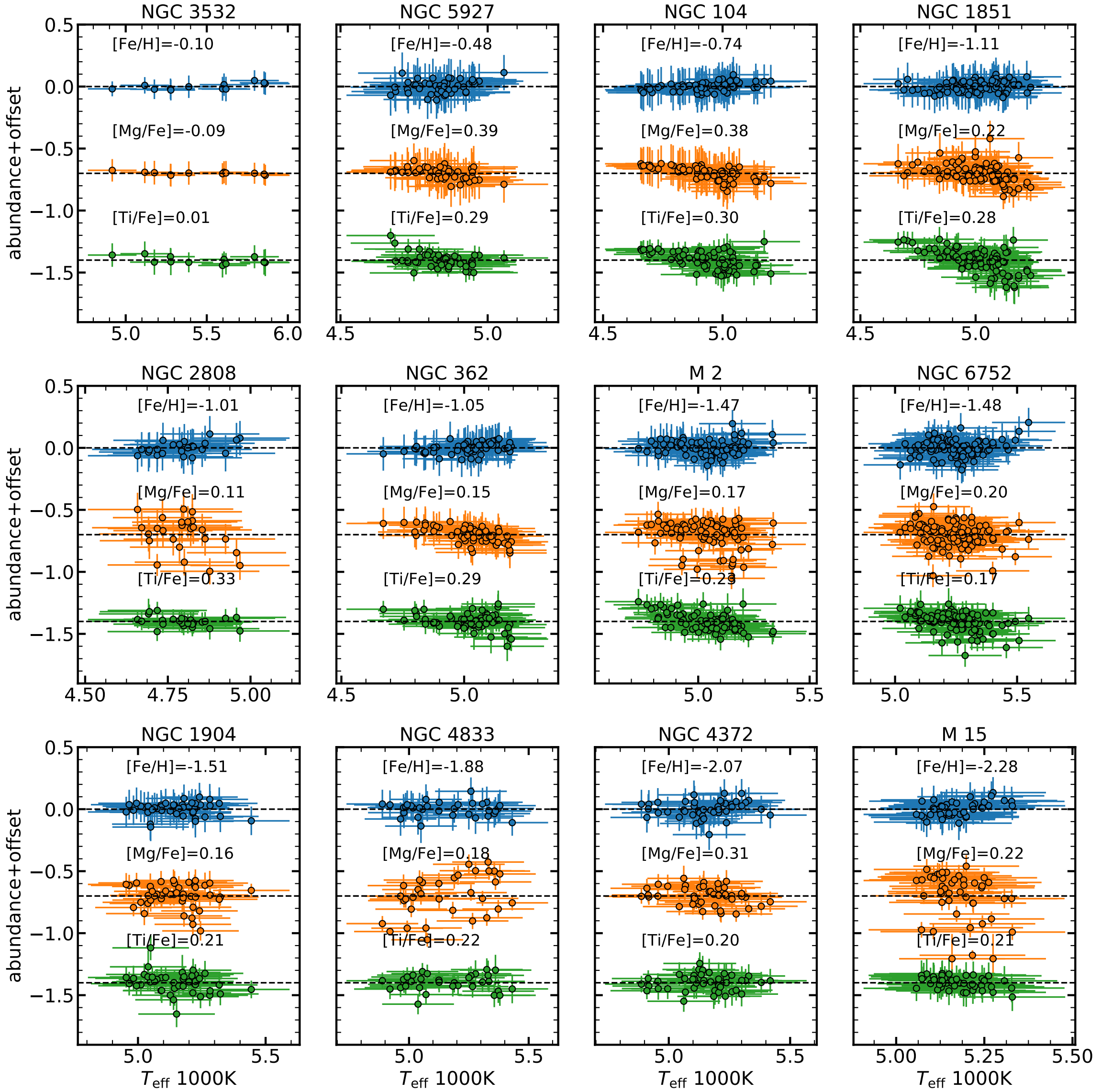

Figure 2.9: NLTE abundances as a function of $T_{\rm eff}$ for all cluster stars. The average and scatter are shown for all elements. The scatter in [Mg/Fe] is much larger than in [Fe/H] and [Ti/Fe], and it is typically attributed to multiple episodes of star formation and self-enrichment (see recent review by Bastian & Lardo 2018, and references therein). See Section 2.3.2 for details.

The test of internal accuracy suggests (Section 2.2.6) that we cannot have derived robust Mn abundances for much of the parameter space, because Mn lines in the HR10 spectra are weak in the metal-poor regime. Hence, the mean [Mn/Fe] ratios are only provided for the two metal-rich clusters NGC 3532 and NGC 5927.

Abundance spreads in clusters

Fig. 2.9 shows the [Fe/H], [Ti/Fe], and [Mg/Fe] abundance estimates in stars of OCs and GCs against stellar $T_{\rm eff}$. The uncertainties represent the systematic errors computed as described in see Section 2.3.2. The open cluster NGC 2243 is shown separately in Fig. 2.10 as it shows signatures of atomic diffusion. Of a particular interest is the dip of [Fe/H] at the cluster turn-off ($T_{\rm eff} \sim 6400$ K), which is qualitatively consistent with the predictions of stellar evolution models, which include radiative acceleration and gravitational settling (e.g. Deal et al. 2018). We leave a detailed exploration of this effect for our future study.

Whereas prominent systematic biases appear to be absent for most clusters, there is some evidence for a small anti-correlation of [Mg/Fe] and/or [Ti/Fe] values with $T_{\rm eff}$, for the moderately metal-poor clusters NGC 1851, NGC 362, M2, and NGC 6752. These clusters also show a somewhat tilted distribution of stars relative to the isochrones in the $T_{\rm eff} - \log g$ plane (Fig.2.5,2.6) suggesting that the origin of the trends is likely in the spectral models or method, employed in this work. Currently we have no straightforward solution for this effect.

The average abundance of a cluster $< X >$ and internal dispersion σ_X are computed using maximum likelihood (ML) approach (Walker et al. 2006; Piatti & Koch 2018), where we take into account the individual abundance uncertainties ΔX of each star. We numerically maximise the logarithm of the likelihood L, given as:

$$\ln L = -\frac{1}{2}\sum_{i}^{N}\ln(\Delta X_i^2+\sigma_X^2) - \frac{1}{2}\sum_{i}^{N}\frac{(X_i - < X >)^2}{\Delta X_i^2+\sigma_X^2} - \frac{N}{2}\ln 2\pi \tag{2.3}$$

where N is the number of stars in a cluster and X refers to one of [Fe/H], [Mg/Fe], [Ti/Fe] and [Mn/Fe]. The errors of the mean and dispersion are computed from the respective covariance matrices (Walker et al. 2006).

We find that all clusters are homogeneous in [Fe/H] and [Ti/Fe] at an uncertainty level of 0.03 dex. Four clusters (M 15, M2, NGC 4833, NGC 2808) show a larger scatter in [Mg/Fe] at the level of 0.07 dex or greater. Modest internal dispersions $\sigma_{\rm [Mg/Fe]} \sim 0.04$ dex are detected in NGC 1904 and NGC 6572.

In Fig. 2.11 we show the spectra of two M 15 stars with similar NLTE atmospheric parameters, though with significantly different magnesium abundances (Δ[Mg/Fe] = 0.65 dex). In these two spectra the relative depth of the Mg line at 5528.4 Å changes more than two times, in comparison to the nearby line of ionised scandium at 5526.8 Å.

Spreads in light element abundances, including Mg, have already been reported for a number of clusters, including NGC 2808 (Carretta 2015), M2 (Yong et al. 2015), NGC 4833 (Carretta et al. 2014) and M15 (Carretta et al. 2009). These spreads are typically attributed to multiple episodes of star formation and self-enrichment (see the recent review by Bastian & Lardo 2018, and references therein).

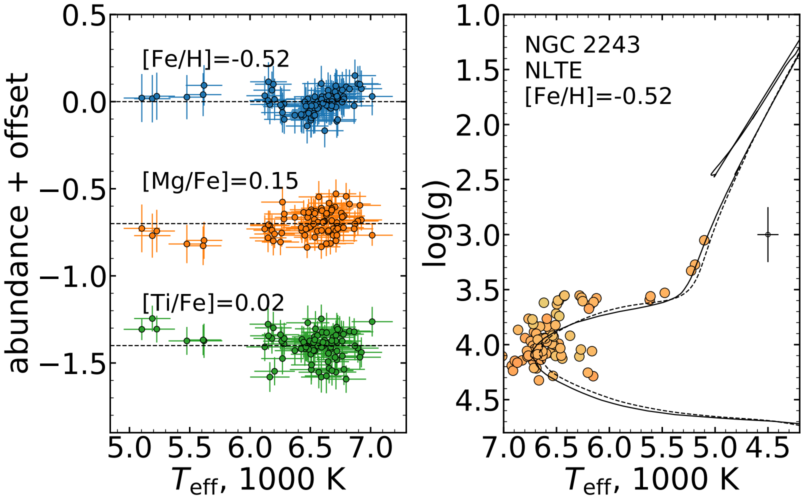

Figure 2.10: Abundances as a function of $T_{\rm eff}$ and the $T_{\rm eff}$-log(g) diagram for the open cluster NGC 2243. All values are our NLTE results. The isochrones were computed for the age of 3.8 Gyr from Anthony-Twarog et al. (2005) and $[{\rm Fe/H}]_{\rm NLTE} = -0.52$ dex.

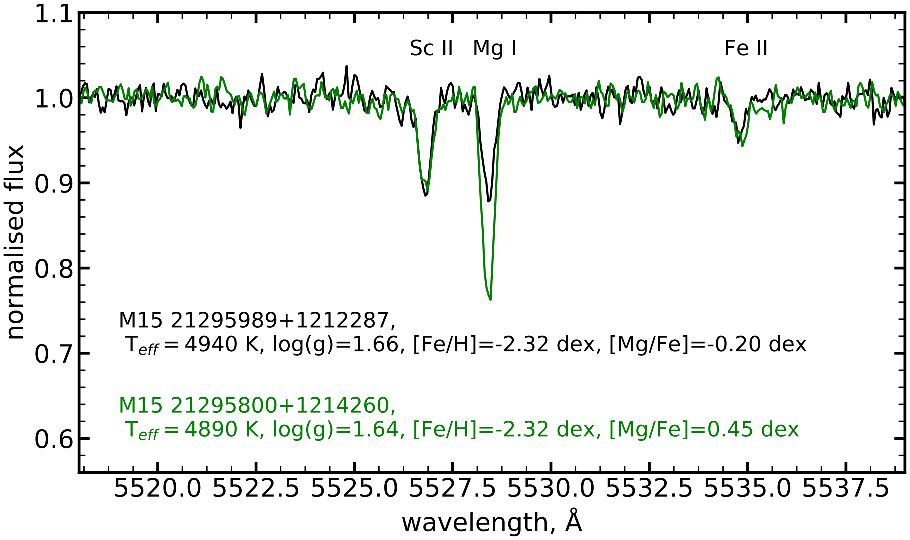

Figure 2.11: Comparison of the spectra of two stars with similar NLTE atmospheric parameters.

Table 2.5:: Maximum likelihood estimates of the cluster average abundances and internal dispersions.

Cluster N stars	$<[\mathrm{Fe/H}]_{\mathrm{NLTE}}>$ $<[\mathrm{Fe/H}]_{\mathrm{LTE}}>$ dex	$\sigma[\mathrm{Fe/H}]_{\mathrm{NLTE}}$ $\sigma[\mathrm{Fe/H}]_{\mathrm{LTE}}$ dex	$<[\mathrm{Mg/Fe}]_{\mathrm{NLTE}}>$ $<[\mathrm{Mg/Fe}]_{\mathrm{LTE}}>$ dex	$\sigma[\mathrm{Mg/Fe}]_{\mathrm{NLTE}}$ $\sigma[\mathrm{Mg/Fe}]_{\mathrm{LTE}}$ dex	$<[\mathrm{Ti/Fe}]_{\mathrm{NLTE}}>$ $<[\mathrm{Ti/Fe}]_{\mathrm{LTE}}>$ dex	$\sigma[\mathrm{Ti/Fe}]_{\mathrm{NLTE}}$ $\sigma[\mathrm{Ti/Fe}]_{\mathrm{LTE}}$ dex
NGC 3532	-0.10 ± 0.02	0.00 ± 0.02	-0.09 ± 0.03	0.00 ± 0.03	0.01 ± 0.03	0.00 ± 0.03
12	-0.09 ± 0.02	0.00 ± 0.03	-0.07 ± 0.03	0.00 ± 0.03	0.01 ± 0.03	0.00 ± 0.03
NGC 5927	-0.48 ± 0.02	0.00 ± 0.02	0.39 ± 0.02	0.00 ± 0.02	0.29 ± 0.01	0.00 ± 0.02
47	-0.49 ± 0.02	0.00 ± 0.02	0.41 ± 0.02	0.00 ± 0.02	0.23 ± 0.01	0.00 ± 0.02
NGC 2243	-0.52 ± 0.01	0.00 ± 0.01	0.15 ± 0.01	0.00 ± 0.02	0.02 ± 0.01	0.00 ± 0.04
84	-0.57 ± 0.01	0.00 ± 0.02	0.26 ± 0.01	0.00 ± 0.02	0.01 ± 0.01	0.00 ± 0.05
NGC 104	-0.74 ± 0.02	0.00 ± 0.02	0.38 ± 0.02	0.00 ± 0.02	0.30 ± 0.01	0.00 ± 0.02
68	-0.75 ± 0.02	0.00 ± 0.02	0.42 ± 0.02	0.00 ± 0.02	0.26 ± 0.01	0.00 ± 0.03
NGC 1851	-1.11 ± 0.01	0.00 ± 0.02	0.22 ± 0.01	0.00 ± 0.02	0.28 ± 0.01	0.00 ± 0.02
88	-1.15 ± 0.01	0.00 ± 0.02	0.36 ± 0.01	0.00 ± 0.02	0.24 ± 0.01	0.00 ± 0.01
NGC 2808	-1.01 ± 0.03	0.00 ± 0.03	0.11 ± 0.03	0.09 ± 0.03	0.33 ± 0.02	0.00 ± 0.02
25	-1.03 ± 0.03	0.00 ± 0.03	0.22 ± 0.03	0.00 ± 0.09	0.30 ± 0.01	0.00 ± 0.02
NGC 362	-1.05 ± 0.02	0.00 ± 0.02	0.15 ± 0.01	0.00 ± 0.02	0.29 ± 0.01	0.00 ± 0.01
62	-1.09 ± 0.02	0.00 ± 0.02	0.26 ± 0.02	0.00 ± 0.02	0.26 ± 0.01	0.00 ± 0.01
M 2	-1.47 ± 0.01	0.00 ± 0.02	0.17 ± 0.01	0.07 ± 0.01	0.23 ± 0.01	0.00 ± 0.02
78	-1.54 ± 0.01	0.00 ± 0.02	0.34 ± 0.02	0.08 ± 0.02	0.25 ± 0.01	0.00 ± 0.01
NGC 6752	-1.48 ± 0.01	0.00 ± 0.01	0.20 ± 0.01	0.03 ± 0.02	0.17 ± 0.01	0.00 ± 0.01
110	-1.56 ± 0.01	0.00 ± 0.01	0.35 ± 0.01	0.04 ± 0.02	0.23 ± 0.01	0.00 ± 0.01
NGC 1904	-1.51 ± 0.02	0.00 ± 0.02	0.16 ± 0.01	0.04 ± 0.02	0.21 ± 0.01	0.00 ± 0.02
44	-1.60 ± 0.02	0.00 ± 0.02	0.31 ± 0.02	0.00 ± 0.04	0.24 ± 0.01	0.00 ± 0.03
NGC 4833	-1.88 ± 0.02	0.00 ± 0.02	0.18 ± 0.03	0.15 ± 0.02	0.22 ± 0.01	0.00 ± 0.02
33	-2.08 ± 0.02	0.00 ± 0.03	0.36 ± 0.03	0.18 ± 0.03	0.24 ± 0.02	0.00 ± 0.02
NGC 4372	-2.07 ± 0.02	0.00 ± 0.02	0.31 ± 0.01	0.00 ± 0.03	0.20 ± 0.01	0.00 ± 0.02
45	-2.33 ± 0.02	0.00 ± 0.02	0.51 ± 0.02	0.00 ± 0.04	0.22 ± 0.01	0.00 ± 0.02
M 15	-2.28 ± 0.02	0.00 ± 0.02	0.22 ± 0.03	0.16 ± 0.02	0.21 ± 0.02	0.00 ± 0.02
46	-2.58 ± 0.02	0.00 ± 0.02	0.36 ± 0.04	0.22 ± 0.03	0.19 ± 0.01	0.00 ± 0.02

The estimated internal dispersions are summarised in Table 2.5. In the following, to be consistent with the literature, we will focus on the *observed* intra-cluster dispersion, instead of the ML estimated internal dispersion. We note that these two are not the same as the latter probes the *intrinsic* dispersion that is not accounted for by the measurement uncertainties, while the former includes both.

2.4 Discussion

2.4.1 Comparison with the literature

In what follows, we discuss our results for the Galactic clusters in the context of their chemical properties. Many literature abundances are given in 'standard' format: mean ± intra-cluster spread, computed as a simple standard deviation using all measurement in the cluster. In some cases, when not given in the same format, we recompute the mean and the standard deviations using the values of individual stars in the literature. Our own results are presented in the same format with mean from ML analysis and the *observed* intra-cluster spread (not the ML estimated internal dispersion) given in Table 2.6. We start with two open clusters and then continue with globular clusters, in order from the most metal-rich to the most metal-poor one.

NGC 3532

NGC 3532 is a young nearby metal-rich cluster at a heliocentric distance of $d_\odot \sim 0.5$ kpc (Clem et al. 2011; Fritzewski et al. 2019). The cluster has been extensively surveyed for variable and binary stars (González & Lapasset 2002), as well as for white dwarfs (Dobbie et al. 2009, 2012) that allowed accurate estimates of the cluster age of ~ 300 Myr from the white dwarf cooling sequence. Fritzewski et al. (2019) report a very low reddening towards the cluster of only 0.034 ± 0.012 mag. They also emphasize a systematic difference between the best-fit isochrones and the observed stellar parameters at the faint end of the cluster main-sequence.

Table 2.6:: Mean clusters abundances (ML estimate - avg) with observed intra-cluster spread (standard deviation - std) and mean systematic error (<err>).

Cluster	#stars N	[Fe/H]$_{\mathrm{NLTE}}$ dex avg std <err>	[Fe/H]$_{\mathrm{LTE}}$ dex avg std <err>	[Mg/Fe]$_{\mathrm{NLTE}}$ dex avg std <err>	[Mg/Fe]$_{\mathrm{LTE}}$ dex avg std <err>	[Ti/Fe]$_{\mathrm{NLTE}}$ dex avg std <err>	[Ti/Fe]$_{\mathrm{LTE}}$ dex avg std <err>
NGC 3532	12	-0.10 0.02 0.10	-0.09 0.03 0.11	-0.09 0.01 0.09	-0.07 0.01 0.12	0.01 0.03 0.10	0.01 0.03 0.11
NGC 5927	47	-0.48 0.05 0.16	-0.49 0.05 0.16	0.39 0.04 0.07	0.41 0.05 0.07	0.29 0.06 0.07	0.23 0.05 0.07
NGC 2243	84	-0.52 0.06 0.08	-0.57 0.07 0.11	0.15 0.07 0.08	0.26 0.09 0.09	0.02 0.08 0.09	0.01 0.09 0.10
NGC 104	68	-0.74 0.03 0.15	-0.75 0.03 0.17	0.38 0.05 0.08	0.42 0.04 0.08	0.30 0.07 0.08	0.26 0.07 0.08
NGC 1851	88	-1.11 0.04 0.14	-1.15 0.04 0.15	0.22 0.08 0.10	0.36 0.08 0.08	0.28 0.09 0.11	0.24 0.07 0.10
NGC 2808	25	-1.01 0.05 0.14	-1.03 0.05 0.15	0.11 0.14 0.08	0.22 0.15 0.06	0.33 0.04 0.07	0.30 0.04 0.07
NGC 362	62	-1.05 0.04 0.13	-1.09 0.04 0.16	0.15 0.06 0.09	0.26 0.07 0.08	0.29 0.06 0.09	0.26 0.06 0.09
M 2	78	-1.47 0.06 0.09	-1.54 0.06 0.12	0.17 0.11 0.09	0.34 0.13 0.08	0.23 0.07 0.10	0.25 0.06 0.09
NGC 6752	110	-1.48 0.06 0.09	-1.56 0.07 0.12	0.20 0.09 0.09	0.35 0.11 0.09	0.17 0.07 0.09	0.23 0.07 0.10
NGC 1904	44	-1.51 0.05 0.09	-1.60 0.07 0.12	0.16 0.09 0.09	0.31 0.11 0.09	0.21 0.08 0.10	0.24 0.09 0.10
NGC 4833	33	-1.88 0.06 0.08	-2.08 0.08 0.11	0.18 0.17 0.08	0.36 0.20 0.10	0.22 0.06 0.08	0.24 0.07 0.10
NGC 4372	45	-2.07 0.06 0.09	-2.34 0.08 0.13	0.31 0.07 0.09	0.51 0.09 0.09	0.20 0.06 0.08	0.22 0.07 0.10
M 15	46	-2.28 0.06 0.08	-2.58 0.07 0.10	0.22 0.19 0.11	0.36 0.23 0.09	0.21 0.05 0.09	0.19 0.05 0.12

On the basis of 12 main-sequence stars, we find the metallicity $[\mathrm{Fe/H}]_{\mathrm{NLTE}} = -0.10 \pm 0.02$ dex and $[\mathrm{Fe/H}]_{\mathrm{LTE}} = -0.09 \pm 0.03$ dex. This estimate is consistent, within the uncertainties, with estimates based on the analysis of high-resolution spectra by Santos et al. (2012), Conrad et al. (2014), and Netopil (2017). Fritzewski et al. (2019) reported the metallicity of [Fe/H] of -0.07 ± 0.10 dex using lower-resolution near-IR spectra.

Our NLTE abundance ratios suggest that the cluster is moderately α-poor, with $[\mathrm{Mg/Fe}]_{\mathrm{NLTE}}$ of -0.09 ± 0.01 dex, although the [Ti/Fe] ratio is solar $[\mathrm{Ti/Fe}]_{\mathrm{NLTE}} = 0.01 \pm 0.03$ dex. The [Mn/Fe] ratio is sub-solar, $[\mathrm{Mn/Fe}]_{\mathrm{NLTE}} = -0.16 \pm 0.03$ dex.

NGC 2243

NGC 2243 is an old Galactic open cluster located below the Galactic plane, at $z = -1.1 \pm 0.1$ kpc, and at a Galactocentric distance of 10.7 ± 0.02 kpc (Jacobson et al. 2011). The reddening towards the cluster was estimated to be E(B-V)$= 0.055 \pm 0.004$ mag (Anthony-Twarog et al. 2005). The age of the cluster was determined by several methods including spectroscopy, CMD isochrone fitting (Anthony-Twarog et al. 2005), using model age-luminosity and age-radius relations for a eclipsing binaries (Kaluzny et al. 2006), bracketing 4 ± 1 Gyr.

The cluster has been subject to a very detailed chemical abundance analysis (for example a review by Heiter et al. 2014). Gratton (1982) and Gratton & Contarini (1994) derived a spectroscopic metallicity of $[\mathrm{Fe/H}] = -0.42 \pm 0.05$ dex, as well as detailed chemical abundances of the elements from C to Eu for a few RGB stars in the cluster. Their estimates were confirmed by Friel et al. (2002) and Jacobson et al. (2011), who derived Fe, Ni, Ca, Si, Ti, Cr, Al, Na, and Mg abundances in a small sample of RGB stars. According to the latter study, this is one of the most metal-poor clusters at its $\mathrm{R_{GC}} \sim 11$ kpc. This cluster has also been observed within the OCCAM APOGEE survey (Cunha et al. 2016). Their estimates of NGC 2243 abundances are somewhat different from Jacobson et al. (2011), with Mg being -0.14 dex lower and more subtle differences for the other elements. In contrast to Jacobson et al. (2011), Cunha et al. (2016) also find a very large spread of metallicities in the cluster members, ranging from -0.4 to $+0.3$ dex. Magrini et al. (2018) employed Gaia-ESO iDR5 abundances obtained from the high-resolution UVES spectra of RGB stars in NGC 2243. They find that the cluster shows a noticeable enhancement of the s-process elements Zr, Ce, and La, whereby the abundances ratios of [Y/Fe] and [Eu/Fe] are consistent with the solar values.

François et al. (2013) reported detailed abundances for the main-sequence and subgiant stars in the cluster. Their [Fe/H] of −0.54 ± 0.10 dex is consistent with our NLTE estimate of $[\text{Fe/H}]_{\text{NLTE}} = -0.52 \pm 0.06$ dex. Our estimate of $[\text{Ti/Fe}]_{\text{NLTE}} = 0.02 \pm 0.08$ dex is also in agreement with the value obtained by François et al. (2013), [Ti/Fe] = 0.20 ± 0.22 dex, within the combined uncertainties of both measurements. In fact, our lower estimate of [Ti/Fe] corroborates the scaled-solar estimates of other α-elements reported by François et al. (2013), [Ca/Fe] = 0.00 ± 0.14 dex and [Si/Fe] = 0.12 ± 0.20 dex.

The NLTE abundances provide some evidence for the atomic diffusion. Particularly interesting is the dip of [Fe/H] at the cluster turn-off ($T_{\text{eff}} \sim 6400$ K), which is qualitatively consistent with the predictions of stellar evolution models that include radiative acceleration and gravitational settling (e.g. Deal et al. 2018).

NGC 5927

NGC 5927 is a metal-rich globular cluster located close to the Galactic plane, at an altitude $z \sim 0.6$ kpc (Casetti-Dinescu et al. 2007). With the age of 12 Gyr (Dotter et al. 2010) and metallicity of $[\text{Fe/H}] \sim -0.5$ dex (Mura-Guzmán et al. 2018), the cluster is among the oldest metal-rich clusters known in the Galaxy. The analysis of this cluster is complicated by a large reddening of $E(B-V) = 0.45$ mag (Heitsch & Richtler 1999). Casetti-Dinescu et al. (2007) favour the origin of the cluster in a thick disk, given its orbital parameters, resembling those of field stars in the rotationally-supported Galactic component. High-resolution spectroscopy of the cluster revealed the presence of multiple populations, especially prominent in the anti-correlation between Na and O (Pancino et al. 2017; Mura-Guzmán et al. 2018). The latter study also pointed out a similarity in the chemical properties of NGC 5927 and NGC 6440, a metal-rich GC in the Galactic bulge that could potentially hint at the common origin of the both systems.

Our NLTE estimate $[\text{Fe/H}]_{\text{NLTE}} = -0.48 \pm 0.05$ dex is in very good agreement with earlier spectroscopic studies (Mura-Guzmán et al. 2018, $[\text{Fe/H}] = -0.47 \pm 0.02$ dex). However, the abundance ratios are somewhat different. In particular, we find both Mg and Ti to be higher, $[\text{Mg/Fe}]_{\text{NLTE}} = 0.39 \pm 0.04$ dex and $[\text{Ti/Fe}]_{\text{NLTE}} = 0.29 \pm 0.06$ dex, compared to the results of the latter study. For Ti, our higher estimate is likely the consequence of NLTE over-ionisation, as the LTE abundance is $[\text{Ti/Fe}]_{\text{LTE}} = 0.23 \pm 0.05$ dex, which is consistent with the estimate of [Ti/Fe] = 0.32 ± 0.05 dex from Mura-Guzmán et al. (2018). In contrast, the difference in Mg abundance is not related to NLTE. Our LTE Mg abundance is $[\text{Mg/Fe}]_{\text{LTE}} = 0.41 \pm 0.05$ dex, which is much higher than that of Mura-Guzmán et al. (2018), [Mg/Fe] = 0.27 ± 0.02 dex. It is possible that the differences stem from the differences in atomic data and/or model atmospheres. Mura-Guzmán et al. (2018) employ the MOOG code, Kurucz model atmospheres, and linelists from Villanova & Geisler (2011, and references therein). Our linelists have been extensively updated over the past years, and in particular for Mg lines, we used the data from Pehlivan Rhodin et al. (2017). We were unable to find the atomic data in Villanova & Geisler (2011) and hence cannot provide a detailed analysis of the consistency of the models. Our average [Mn/Fe] abundance ratio in NGC 5927 is sub-solar $[\mathrm{Mn/Fe}]_{\mathrm{NLTE}} = -0.20 \pm 0.03$ dex, $[\mathrm{Mn/Fe}]_{\mathrm{LTE}} = -0.34 \pm 0.03$ dex. This estimate is much lower compared to [Mn/Fe] = −0.09 ± 0.08 dex derived by Mura-Guzmán et al. (2018), but it is mostly due to the difference of −0.16 in the adopted solar abundance (MARCS $\log A(\mathrm{Mn})_\odot = 5.37$ dex and MAFAGS-OS $\log A(\mathrm{Mn})_\odot = 5.53$ dex).

NGC 104 (47 Tuc)

The cluster NGC 104 (47 Tuc) is among the brightest and well-studied clusters of the Milky Way (e.g. Anderson et al. 2009; Campos et al. 2018; Carretta et al. 2009; Milone et al. 2012; Lapenna et al. 2014; Cordero et al. 2014; Thygesen et al. 2014; Černiauskas et al. 2017). The recent estimate of the distance to the cluster is $d_\odot = 4.45$ kpc (Chen et al. 2018), which was obtained on the basis of Gaia DR2 parallaxes. The reddening towards the system is very low, $E(B-V) = 0.03 \pm 0.1$ mag (Brogaard et al. 2017) allowing an accurate estimate of the cluster age of ∼ 12.5 Gyr (Brogaard et al. 2017) and initial He and metal abundances using observations of the horizontal branch and stellar evolutionary codes (e.g. Denissenkov et al. 2017). Several studies reported a complex morphology of the cluster, with multiple populations that show a considerable radial anisotropy (e.g. Milone et al. 2012; Cordero et al. 2014; Piotto et al. 2015) and high internal rotation (Bellini et al. 2017; Bianchini et al. 2018). Chemical abundance patterns, in the form of Na-O anti-correlations, enrichment in He and N, and depletion of C, indicate complex chemical evolution in the cluster (Cordero et al. 2014; Kučinskas et al. 2014; Marino et al. 2016).

Our NLTE estimate of the cluster metallicity, $[\mathrm{Fe/H}]_{\mathrm{NLTE}} = -0.74 \pm 0.03$ dex, is in very good agreement with previous estimates (Koch & McWilliam 2008; Cordero et al. 2014; Dobrovolskas et al. 2014; Thygesen et al. 2014). The latter study reports [Fe/H] = −0.78 ± 0.07 dex obtained by 1D LTE modelling of Fe lines. The authors also test the effect of NLTE, finding the effects to be of the order +0.02 dex on the Fe abundances. Indeed, this is fully confirmed by our LTE metallicities, which are 0.01 dex lower compared to our NLTE results. For Mg, Thygesen et al. (2014) report [Mg/Fe] = 0.44 ± 0.05 dex in LTE, which is in excellent agreement with our LTE value, $[\mathrm{Mg/Fe}]_{\mathrm{LTE}} = 0.42 \pm 0.04$ dex, and is only slightly higher than our NLTE result $[\mathrm{Mg/Fe}]_{\mathrm{NLTE}} = 0.38 \pm 0.05$ dex. Also the Ti abundances are consistent with Thygesen et al. (2014). We obtain $[\mathrm{Ti/Fe}]_{\mathrm{NLTE}} = 0.30 \pm 0.07$ dex and $[\mathrm{Ti/Fe}]_{\mathrm{LTE}} = 0.26 \pm 0.07$ dex, which agrees within the uncertainties with the measured value of [Ti/Fe]=0.28 ± 0.08 dex from Thygesen et al. (2014).

NGC 1851

NGC 1851 is a moderately metal-poor globular cluster at an R_{GC} of 17 kpc from the Galactic centre and ∼ 7 kpc below the disk plane (Harris 1996, 2010 edition). Wagner-Kaiser et al. (2017) find the cluster age of 11.5 Gyr. This cluster also has a complex morphology with tidal tails (Carballo-Bello et al. 2018) and a large diffuse stellar envelope (Kuzma et al. 2018). Some have argued for the evolutionary connection between NGC 1851 and several other clusters (NGC 1904, NGC 2808, and NGC 2298) on the basis of their spatial proximity (Bellazzini et al. 2001), as we confirm by our abundances below. An idea has been put forward that all four clusters are associated with the disrupted Canis Major dwarf galaxy (Martin et al. 2004). Others suggest that NGC 1851 is possibly a nucleus of a disrupted dwarf galaxy (Bekki & Yong 2012; Kuzma et al. 2018) or could have formed as a result of the merger of two globular clusters (Carretta et al. 2011). The cluster hosts multiple stellar populations, seen in photometric data on the main sequence, subgiant branch, and on RGB (Milone et al. 2008; Turri et al. 2015; Cummings et al. 2017). Also the spectroscopic analysis of C and N suggests the presence of several populations (Yong & Grundahl 2008; Yong et al. 2015; Simpson et al. 2017).

Our metallicities for NGC 1851 are slightly higher compared to previous studies. Gratton et al. (2012) find a range of metallicities in the cluster from [Fe/H] = −1.23 ± 0.06 dex (subgiant branch) to [Fe/H] = −1.14 ± 0.06 dex (RGB). Our analysis yields $[\mathrm{Fe/H}]_{\mathrm{NLTE}} = -1.11 \pm 0.04$ dex and $[\mathrm{Fe/H}]_{\mathrm{LTE}} = -1.15 \pm 0.04$ dex, whereas Yong et al. (2015) report [Fe/H] = −1.28 ± 0.05 and Marino et al. (2014) obtain [Fe/H] = −1.33 ± 0.09 dex.

For Mg, we find $[\mathrm{Mg/Fe}]_{\mathrm{NLTE}} = 0.22 \pm 0.08$ dex, which is lower than the value reported by Marino et al. (2014) [Mg/Fe] = 0.44 ± 0.16 dex. However, this difference can be almost entirely explained by NLTE. Indeed our LTE estimates of [Mg/Fe] are much higher, $[\mathrm{Mg/Fe}]_{\mathrm{LTE}} = 0.36 \pm 0.05$ dex, and are also in agreement with the LTE estimates by Carretta et al. (2011), [Mg/Fe] = 0.35 ± 0.03 dex. For Ti, we find the opposite offset, in the sense that our NLTE values,

$[\mathrm{Ti/Fe}]_{\mathrm{NLTE}} = 0.28 \pm 0.06$ dex, are higher compared to the LTE results by Carretta et al. (2011) $[\mathrm{Ti/Fe}] = 0.17 \pm 0.05$ dex. This can be explained by NLTE, as our LTE abundances of Ti are slightly lower, $[\mathrm{Ti/Fe}]_{\mathrm{LTE}} = 0.24 \pm 0.06$ dex, consistent with the latter study within the combined uncertainties of the both LTE measurements.

It is interesting, in the context of the common formation scenario of NGC 1851 and NGC 2808, as proposed by Martin et al. (2004), that our chemical abundances in the two clusters are similar. In fact, given the uncertainties of our measurements, both clusters are consistent with being formed from the same material, and having the same progenitor system.

NGC 2808

NGC 2808 is a moderately metal-poor cluster with an age of 11 Gyr (Wagner-Kaiser et al. 2017). The cluster is among the most massive 7.42×10^5 $\mathrm{M}_\odot$ (Baumgardt & Hilker 2018) GCs in the Milky Way, with multiple populations (Piotto et al. 2007; Milone et al. 2015), tidal tails (Carballo-Bello et al. 2018), and a complex evolutionary history (Simioni et al. 2016). NGC 2808 was among the first clusters, for which a prominent Na-O anti-correlation was reported (Carretta et al. 2006), along with a He spread (D'Antona et al. 2005), and a Mg - Al anti-correlation (Carretta 2006).

Our LTE metallicity, $[\mathrm{Fe/H}]_{\mathrm{LTE}} = -1.03 \pm 0.05$ dex, is slightly higher compared to the recent literature values. Carretta (2015) report $[\mathrm{Fe/H}] = -1.13 \pm 0.03$ dex using the Fe I lines and $[\mathrm{Fe/H}] = -1.14 \pm 0.03$ dex using the Fe II lines. They also find a large spread in [Mg/Fe] abundance ratios, which is corroborated by our results. In particular, we find that the individual LTE abundance ratios of [Mg/Fe] range from 0.08 to 0.45 dex, and the average value and its dispersion, $[\mathrm{Mg/Fe}]_{\mathrm{LTE}} = 0.22 \pm 0.15$ dex, is consistent with $[\mathrm{Mg/Fe}] = 0.26 \pm 0.16$ dex obtained by Carretta (2015). For Ti, our estimate $[\mathrm{Ti/Fe}]_{\mathrm{LTE}} = 0.29 \pm 0.04$ dex is slightly higher compared to $[\mathrm{Ti/Fe}] = 0.21 \pm 0.04$ dex derived by Carretta (2015). Our NLTE measurements are: $[\mathrm{Fe/H}]_{\mathrm{NLTE}} = -1.01 \pm 0.05$ dex, $[\mathrm{Mg/Fe}]_{\mathrm{NLTE}} = 0.11 \pm 0.14$ dex, and $[\mathrm{Ti/Fe}]_{\mathrm{NLTE}} = 0.33 \pm 0.04$ dex.

NGC 362

NGC 362 is one of the benchmark GC systems on a very eccentric orbit (Tucholke 1992). It has been extensively studied in the literature since the early work by Menzies (1967). A recent analysis of Gaia astrometric data places it at a heliocentric distance of 8.54 kpc (Chen et al. 2018), at a relative proximity to the Galactic disk plane. Similar to NGC 104, the cluster is seen in the direction of the Small Magellanic cloud (SMC) that allows a very accurate determination of its distance, by exploiting the astrometric properties of the background SMC stars and quasars to estimate systematic offset in parallax (Chen et al. 2018). Photometric studies of the cluster revealed multiple sequences on the horizontal branch (Bellazzini et al. 2001; Dotter et al. 2010; Gratton et al. 2010; Piotto et al. 2012). The spectroscopic follow-up confirmed its unique nature, with discrete groups of Na/O ratios (Carretta et al. 2013), a bimodal distribution of CN (Smith & Langland-Shula 2009; Lim et al. 2016), a very large spread of Al abundances, yet a relatively narrow dispersion of Li (D'Orazi et al. 2015).

Our NLTE metallicity for this cluster, $[\mathrm{Fe/H}]_{\mathrm{NLTE}} = -1.05 \pm 0.04$ dex, is somewhat higher compared to the results of the earlier studies. Our LTE estimate is lower, $[\mathrm{Fe/H}]_{\mathrm{LTE}} = -1.09 \pm 0.04$ dex and is consistent with the RR Lyr-based value from Székely et al. (2007). A very careful analysis of high-resolution spectra by Worley & Cottrell (2010) yielded $[\mathrm{Fe/H}] = -1.20 \pm 0.09$ (from the Fe II lines), which is consistent within the uncertainty with our LTE estimate. A somewhat lower value is reported by D'Orazi et al. (2015). They find [Fe/H] of -1.26 dex from the LTE analysis of RGB stars. The perhaps most extensive chemical study of the cluster, to date, is that by Carretta et al. (2013) employing UVES and Giraffe spectra of 138 RGB stars. For the UVES sample, they find a mean LTE metallicity of $[\mathrm{Fe/H}] = -1.17 \pm 0.05$ dex from the Fe I lines and $[\mathrm{Fe/H}] = -1.21 \pm 0.08$ dex from Fe II lines that is in agreement with our LTE metallicity. Their abundance of [Ti/Fe] (0.22 ± 0.04 dex based on the UVES spectra) and [Mg/Fe] (0.33 ± 0.04 dex) are also in good agreement with our LTE estimates, $[\mathrm{Ti/Fe}]_{\mathrm{LTE}} = 0.26 \pm 0.06$ dex and $[\mathrm{Mg/Fe}]_{\mathrm{LTE}} = 0.26 \pm 0.06$ dex. In contrast, our NLTE values are considerably different, $[\mathrm{Ti/Fe}]_{\mathrm{NLTE}} = 0.29 \pm 0.06$ dex and $[\mathrm{Mg/Fe}]_{\mathrm{NLTE}} = 0.15 \pm 0.06$ dex. To the best of our knowledge, this paper is the first study to provide estimates of NLTE abundances in this cluster.

M2 (NGC 7089)

M2 is a classical old cluster in the halo system, at a distance of ~ 7 kpc below the plane and a heliocentric distance of 11.5 kpc (Harris 1996, 2010 edition). The cluster was the first system, in which a bimodality in the CN distribution was detected (Smith & Mateo 1990; Lardo et al. 2012, 2013). Yong et al. (2014) argued for a trimodal metallicity distribution that has been, however, disputed by Lardo et al. (2016), who found bimodal distribution using Fe II lines. Milone et al. (2015)

employed HST photometry to detect a very rich stellar environment, composed of three main populations standing out in metallicity and a spread in He abundance from the primordial mass fraction of $Y \sim 0.25$ to $Y \sim 0.31$. They also suggest that there are six sub-populations with unique light element abundance patterns, that could potentially hint at either an independent enrichment and star formation of the individual components or at a unique merger formation history of the cluster. The imaging data by Kuzma et al. (2016) further strengthen the latter interpretation, by demonstrating a diffuse stellar envelope that could possibly indicate that the GC is a stripped dSph nucleus.

We find a modest metallicity spread in the cluster $[\mathrm{Fe/H}]_{\mathrm{NLTE}} = -1.47 \pm 0.06$ dex. Our LTE result $[\mathrm{Fe/H}]_{\mathrm{LTE}} = -1.54 \pm 0.06$ dex is in good agreement with the previous measurements, in particular with Lardo et al. (2016), who derive $[\mathrm{Fe/H}] = -1.50 \pm 0.05$ dex for the metal-poor component, using Fe II lines. Yong et al. (2014) report three groups with [Fe/H] ranging from -1.66 ± 0.06 dex to -1.02 ± 0.06 dex, as derived from the Fe II lines. It should be noted, however, that Lardo et al. (2016) suggest that the metal-rich component may not constitute more than 1 % of the cluster population. As to abundance ratios, comparing our LTE estimates with Yong et al. (2014), we find a good agreement in Mg with $[\mathrm{Mg/Fe}]_{\mathrm{LTE}} = 0.34 \pm 0.13$ dex, that should be compared to their estimates of 0.38 ± 0.08 dex. Yet, similar to the other clusters, our NLTE abundance of Mg is lower, $[\mathrm{Mg/Fe}]_{\mathrm{NLTE}} = 0.17 \pm 0.11$ dex. We obtain $[\mathrm{Ti/Fe}]_{\mathrm{NLTE}} = 0.23 \pm 0.07$ dex in NLTE, and $[\mathrm{Ti/Fe}]_{\mathrm{LTE}} = 0.25 \pm 0.06$ dex in LTE, which is lower than the estimates derived by Yong et al. (2014) $[\mathrm{Ti/Fe}] = 0.31 \pm 0.12$ dex. We note, however, that their approach leads to a significant ionisation imbalance of Ti I - Ti II in the two groups, and it is not clear which of the estimates is more reliable. Our measurement of [Ti/Fe] is more consistent with their estimate based on the Ti II lines.

NGC 6752

NGC 6752 is one of the benchmark clusters in the Milky Way, for its proximity at an R_{GC} of only 4 kpc (Harris 1996, 2010 edition) allows a detailed spectroscopic and photometric analysis of the cluster members. The cluster has been extensively observed with VLT (e.g. Carretta et al. 2007; Gruyters et al. 2014; Lee 2018) and with HST (e.g. Ross et al. 2013; Gruyters et al. 2017; Milone et al. 2019). In particular, deep narrow-band photometric observations have been essential to probe the substructure of this system, with multiple stellar populations identified on the RGB and MS (Milone et al. 2010, 2013, 2019; Nardiello et al. 2015; Dotter et al. 2015; Lee 2018). According to a detailed kinematical analysis by Dinescu et al. (1999), the orbital parameters of NGC 6752 are representative of a metal-rich disk cluster, that suggests the disk formation scenario. Some studies report a radial anisotropy in the system (Kravtsov et al. 2011), with fainter subgiant stars and redder RGB stars being more centrally concentrated. Signatures of atomic diffusion and mixing have been reported by Gruyters et al. (2014) from the analysis of chemical abundance distributions along the main sequence and subgiant branch.

A detailed chemical analysis of the cluster members was presented in different studies. The analysis of high-resolution UVES spectra of 38 RGB stars in NGC 6752 by Yong et al. (2005) showed a prominent α-enhancement at [Mg/Fe] = 0.47 ± 0.06 dex, and the iron abundances of [Fe/H] = -1.56 ± 0.10 dex. Both of these estimates are fully consistent with our LTE results of $[\mathrm{Fe/H}]_{\mathrm{LTE}} = -1.56 \pm 0.07$ dex and $[\mathrm{Mg/Fe}]_{\mathrm{LTE}} = 0.35 \pm 0.11$ dex. Furthermore, their LTE estimate of Ti abundance, [Ti/Fe] = 0.14 ± 0.14 dex, is consistent with our LTE value, $[\mathrm{Ti/Fe}]_{\mathrm{LTE}} = 0.23 \pm 0.07$ dex. Our sample is larger than that of Yong et al. (2005) and comprises 110 stars at the base of the RGB, which may account for minor differences between our and their results. On the other hand, our somewhat larger dispersion in abundance ratios is probably not an artefact, as large intra-cluster abundance spreads have also been reported by Yong et al. (2013) from the analysis of high-resolution spectra of RGB stars. Our NLTE estimates are slightly different, but they follow the general trends identified for other metal-poor clusters. The NLTE metallicity and slightly higher, $[\mathrm{Fe/H}]_{\mathrm{NLTE}} = -1.48 \pm 0.06$ dex, whereas the NLTE [Mg/Fe] ratio is correspondingly lower, $[\mathrm{Mg/Fe}]_{\mathrm{NLTE}} = 0.20 \pm 0.09$ dex.

NGC 1904 (M79)

NGC 1904 is a metal-poor globular cluster at a heliocentric distance of 12.9 kpc and 6.3 kpc below the Galactic plane (Harris 1996, 2010 edition). Kains et al. (2012) employed variable stars to determine accurate distance to the cluster, 13.4±0.4 kpc. The age of the system is 14.1±2.1 Gyr (Li & Deng 2018). Similar to NGC 1851, the outskirts of NGC 1904 reveal prominent streams signifying its possible accretion origin Carballo-Bello et al. (2018); Shipp et al. (2018). Fabbian et al. (2005) explore horizontal branch stars in NGC 1904 and find anomalous abundances for hotter stars $T_{\mathrm{eff}} \sim 11000$ K that is He depletions and overabundances of Fe, Ti, Cr, P and Mn, which can be attributed to the onset of diffusion and to radiation pressure in the stable atmospheres of hot horizontal branch stars. Remarkable Li-Al correlation was found in following study by D'Orazi et al. (2015).

Our NLTE metallicity of the cluster is $[\mathrm{Fe/H}]_{\mathrm{NLTE}} = -1.51 \pm 0.05$ dex. This is consistent, modulo the LTE - NLTE difference of -0.07 dex, with the value reported by Carretta et al. (2009), [Fe/H] = -1.58 ± 0.03 dex. Also their LTE Mg abundance, [Mg/Fe] = 0.28 ± 0.06 dex, is in good agreement with our LTE value of $[\mathrm{Mg/Fe}]_{\mathrm{LTE}} = 0.31 \pm 0.11$ dex. Our NLTE estimate is $[\mathrm{Mg/Fe}]_{\mathrm{NLTE}} = 0.16 \pm 0.09$ dex, which is lower than the LTE value. The cluster is also enriched in [Ti/Fe]. We find $[\mathrm{Ti/Fe}]_{\mathrm{NLTE}} = 0.21 \pm 0.08$ dex and $[\mathrm{Ti/Fe}]_{\mathrm{LTE}} = 0.24 \pm 0.09$ dex, and the latter is consistent with the LTE results obtained by Fabbian et al. (2005), [Ti/Fe] = 0.31 ± 0.15 dex.

NGC 4833

NGC 4833 is a nearby cluster at a $d_{\odot}$ of 6.6 kpc, ∼ 1 kpc away from the disk plane (Harris 1996, 2010 edition). The age of the system was estimated at 13.5 Gyr (Wagner-Kaiser et al. 2017). Its orbital eccentricity is consistent with the cluster being a part of the inner halo system Carretta et al. (2010). Yet, Casetti-Dinescu et al. (2007) propose that it could possible be dynamically associated with NGC 5986. The cluster is thought to host multiple populations (Carretta et al. 2014), based on chemical signatures, without photometric follow-up, due to high reddening to the cluster $E(B-V) = 0.32$ mag, with large variations across the cluster.

A detailed spectroscopic analysis of the cluster has been performed by several groups. Carretta et al. (2014) employed UVES and Giraffe spectra of 78 stars to determine the abundances of 20 elements from Na to Nd. They obtained relatively small dispersions for the majority of elements, including Fe. On the other hand, they also found very pronounced Na-O and Mg-Na anti-correlations and a large intra-cluster variation in the abundances of light elements. Specifically, the [Mg/Fe] abundance ratios in the cluster range from slightly sub-solar, [Mg/Fe] ~ -0.05 dex, to highly super-solar values, [Mg/Fe] $\gtrapprox 0.7$ dex. Another high-resolution study of the cluster was presented by Roederer & Thompson (2015), who obtained high S/N spectra with the MIKE spectrograph at the Magellan II telescope. Their estimates of elemental abundances are somewhat different from Carretta et al. (2014). In particular, they report [Fe/H] = -2.25 ± 0.02 dex from the neutral Fe lines, [Fe/H] = -2.19 ± 0.01 dex from the ionised Fe lines, attributing the differences with respect to Carretta et al. (2014) to the technical aspects of the analysis, such as the the linelist and the solar reference abundances. In terms of abundance inhomogeneities and correlations, their study is consistent with Carretta et al. (2014), with pronounced star-to-star variations in the light elements and signatures of bimodality in Na, Al, and Mg.

Our LTE estimates of metallicity and abundance ratios are consistent with the literature estimates. In particular, we find $[\mathrm{Fe/H}]_{\mathrm{LTE}} = -2.08 \pm 0.08$ dex and

$[\mathrm{Mg/Fe}]_{\mathrm{LTE}} = 0.36 \pm 0.20$ dex, which can be compared to $[\mathrm{Fe/H}] = -2.04 \pm 0.02$ dex and $[\mathrm{Mg/Fe}] = 0.36 \pm 0.15$ dex derived by Carretta et al. (2014) from the Giraffe spectra. We also confirm that there is negligible internal dispersion in Ti abundances, with $[\mathrm{Ti/Fe}]_{\mathrm{LTE}}$ of 0.24 ± 0.07 dex, consistent with Carretta et al. (2014) estimate of $[\mathrm{Ti/Fe}] = 0.17 \pm 0.02$ dex. On the other hand, our NLTE abundances are considerably different. For Fe, we infer $[\mathrm{Fe/H}]_{\mathrm{NLTE}} = -1.88 \pm 0.06$ dex, which is higher compared to $[\mathrm{Fe/H}]_{\mathrm{LTE}} = -2.08 \pm 0.08$ dex. Also, the [Mg/Fe] ratios are much lower, $[\mathrm{Mg/Fe}]_{\mathrm{NLTE}} = 0.18 \pm 0.17$ dex, with the abundances in the individual stars ranging from -0.03 to 0.70 dex. The NLTE Ti abundances are only slightly higher compared to the LTE estimates, $[\mathrm{Ti/Fe}]_{\mathrm{NLTE}} = 0.22 \pm 0.06$ dex.

NGC 4372

NGC 4372 is a metal-poor and old globular cluster, with the age of 12.5 Gyr (Kruijssen et al. 2018), at a distance of 1 kpc below the disk plane (Harris 1996, 2010 edition). The cluster suffers from a strong differential reddening, $0.3 \lesssim \mathrm{E(B\text{-}V)} \lesssim 0.8$ (Gerashchenko et al. 1999; Kacharov et al. 2014), which complicates the photometric analysis of the cluster. The mass of the system is estimated at $\sim 2 \times 10^5\ \mathrm{M}_\odot$ (Kacharov et al. 2014), placing it somewhat in the middle of the GC mass spectrum range (Baumgardt & Hilker 2018). Recent studies suggested that NGC 4372 is dynamically associated with another globular cluster NGC 2808 (Casetti-Dinescu et al. 2007). The cluster shows the classical signatures of multiple populations, with a remarkable dispersion in Na, Mg, Al, and O, a Na-O anti-correlation, and, possibly, an Al-Mg anti-correlation (San Roman et al. 2015).

Our average NLTE metallicity of stars in NGC 4372 is -2.07 ± 0.06 dex. Our LTE metallicity is much lower, $[\mathrm{Fe/H}]_{\mathrm{LTE}} = -2.33 \pm 0.08$ dex, following the general trend for all metal-poor clusters seen in Fig. 2.4. Comparing the latter estimate with the literature, we find a satisfactory agreement with a comprehensive study by San Roman et al. (2015), which is also based on the spectra acquired within the Gaia-ESO survey. Their estimate of [Fe/H] is -2.23 ± 0.10 dex[10], consistent with our results within the combined uncertainties of the both estimates. Also the value from Carretta et al. (2009), $[\mathrm{Fe/H}] = -2.19 \pm 0.08$ dex, is somewhat higher than our LTE metallicity. The detailed abundance ratios of our study are also in agreement with those measured by San Roman et al. (2015). We obtain $[\mathrm{Mg/Fe}]_{\mathrm{LTE}} = 0.51 \pm 0.09$ dex and $[\mathrm{Ti/Fe}]_{\mathrm{LTE}} = 0.22 \pm 0.07$ dex in LTE, whereas San Roman et al. (2015) derive $[\mathrm{Mg/Fe}] = 0.44 \pm 0.07$ dex and

---

[10] Note that this value depends on whether large outliers are included or not.

[Ti/Fe] = 0.31 ± 0.03 dex. Our NLTE estimates are $[\mathrm{Mg/Fe}]_{\mathrm{NLTE}} = 0.31 \pm 0.07$ dex and $[\mathrm{Ti/Fe}]_{\mathrm{NLTE}} = 0.20 \pm 0.06$ dex.

M15 (NGC 7078)

M15 is a very old and dense metal-poor Globular cluster located in the Galactic in halo at a $d_{\odot} = 10.4$ kpc and 5 kpc below the Galactic plane (Harris 1996, 2010 edition). It has been extensively studied in the literature, for its extreme metallicity and age, [Fe/H] = −2.3 and $\tau \sim 13$ Gyr (O'Malley et al. 2017; Monelli et al. 2015), rich stellar environment (Arnason et al. 2015; Otsuka et al. 2010), complex morphology (fast-spinning decoupled core, van den Bosch et al. (2006)), and the properties consistent with a core-collapse scenario (den Brok et al. 2014). Several studies report multiple stellar populations in the cluster (Larsen et al. 2015; Nardiello et al. 2018; Bonatto et al. 2019).

M15 has the lowest metallicity in our sample and shows the largest NLTE effects: $[\mathrm{Fe/H}]_{\mathrm{NLTE}} = -2.28 \pm 0.06$ dex, but $[\mathrm{Fe/H}]_{\mathrm{LTE}} = -2.58 \pm 0.07$ dex. Our LTE estimate compares favourably well with Sobeck et al. (2011), who derived [Fe/H] = −2.62 ± 0.08 dex[11] from the analysis of high-resolution spectra of several red giant branch and red horizontal branch stars in the cluster collected with the HIRES spectrograph at the Keck telescope. Worley et al. (2013) report [Fe/H] in the range from −2.4 to −2.3 dex with an uncertainty of 0.1 dex, which is closer to the estimate of [Fe/H] = −2.37 dex derived by Letarte et al. (2006) and [Fe/H] = −2.32 dex by Carretta et al. (2009). Our average LTE abundances of Mg is $[\mathrm{Mg/Fe}]_{\mathrm{LTE}} = 0.36 \pm 0.23$ dex, with the star-to-star variation in the range from −0.26 to 0.66 dex. This is consistent with Carretta et al. (2009), within the uncertainties, and also with the abundances derived by Sobeck et al. (2011), who measured [Mg/Fe] ratios from −0.01 to 0.6 dex. In contrast, the cluster stars exhibit very tight [Ti/Fe] ratios with the mean of $[\mathrm{Ti/Fe}]_{\mathrm{LTE}} = 0.19 \pm 0.05$ dex. Our NLTE results for Mg are much lower than the LTE ones, $[\mathrm{Mg/Fe}]_{\mathrm{NLTE}} = 0.22 \pm 0.19$ dex, whereas the NLTE Ti abundances are nearly consistent with LTE, $[\mathrm{Ti/Fe}]_{\mathrm{NLTE}} = 0.21 \pm 0.05$ dex.

2.4.2 Comparison with Milky Way field stars

It is useful to combine our chemical characterisation of the clusters with their kinematics, in order to compare our results with Galactic field stars. We use the

---

[11] We recompute value using the mean of all measurements from nine red giant branch and red horizontal branch stars.

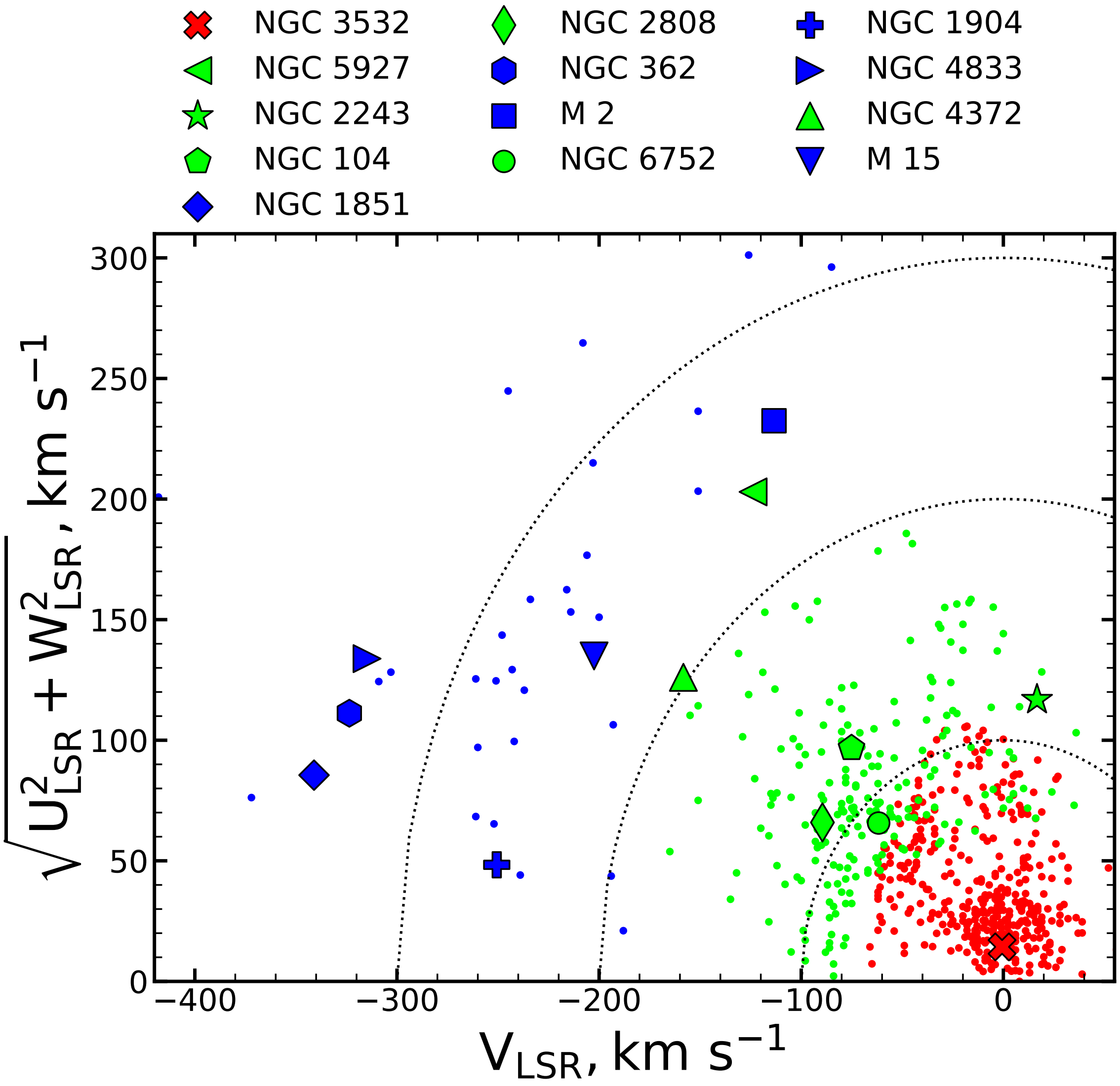

Figure 2.12: The Toomre diagram for clusters and Bensby et al. (2014) field stars. The thin disk population is shown with red colour, the thick disk population with green colour, and the halo population with blue colour. The isolines for total velocity $V_{\rm tot} = \sqrt{U^2_{\rm LSR} + V^2_{\rm LSR} + W^2_{\rm LSR}} = 100,\ 200,\ 300\ \ {\rm km\,s^{-1}}$ are shown as dotted lines.

kinematic selection criteria from Bensby et al. (2014) to assign Galactic population membership to the clusters.

We employ the cluster distances listed in Table 2.3. They were obtained from the colour magnitude diagram horizontal branch (globular clusters Harris (1996, 2010 edition)) or turn-off point (open clusters WEBDA database) fitting. The same distance is assumed for all stars within given cluster. We also take proper motions from Gaia DR2 (Gaia Collaboration et al. 2018) and radial velocities from our analysis and compute galactocentric rectangular velocity components (U,V,W) for all stars in the clusters, with respect to solar motion from Schönrich et al. (2010).

The computed velocities are used to calculate the probability ratios TD/D and TD/H (Bensby et al. 2014, Appendix 1), which allow us to assign population membership to the clusters. We use the following selection criteria: thick disk if $TD/D > 2$ and $TD/H > 1$; thin disk if $TD/D < 0.5$; halo if $TD/H < 1$. Only the open cluster NGC 2243 has a probability ratio of $TD/D = 1.25$ in between the thin and the thick disk. We therefore decide to assign it to the thick disk on the basis of its large separation ($|z| = 1$ kpc) from the Galactic plane. The Toomre diagram for the clusters and field stars is shown in Fig. 2.12.

In Fig. 2.13 and 2.14, we overlay our LTE and NLTE abundance ratios in the clusters with the literature measurements in the Galactic field stars. The field sample is taken from Bensby et al. (2014) and Bergemann et al. (2017). The former dataset represents populations in the solar neighbourhood and has a large coverage in metallicity, $-2.7 \lesssim$ [Fe/H] $\lesssim 0.5$. The Fe abundances were derived in NLTE, while Mg and Ti were derived in LTE analysis. The dataset Bergemann et al. (2017) lacks a thin disk component, [Fe/H] > -0.5, but contains a significant fraction of the thick disk and halo stars. The study provides LTE and NLTE estimates of [Fe/H] and [Mg/Fe] derived using 1D and <3D> atmospheric models. For consistency with our 1D analysis, we use their 1D LTE and 1D NLTE results.

There are several important results, which stand out by comparing our LTE and NLTE measurements in clusters against Galactic field stars. Firstly, our LTE abundances in GCs trace the Galactic field population remarkably well, at least as long as LTE field distributions are employed for the comparison. This supports the conclusions drawn by Pritzl et al. (2005). NGC 3532 and NGC 2243, the two metal-rich clusters with disk-like kinematic properties, occupy the chemical locus of the thin disk. The metal-poor globular clusters trace the thick disk and the halo. Despite a difference of two orders of magnitude in metallicity, all metal-poor GCs follow very tight trends of the average [Mg/Fe] and [Ti/Fe] with [Fe/H]. In particular, all of them occupy the locus situated at [Ti/Fe] ≈ 0.25 dex with small dispersion. On the other hand, the intra-cluster dispersions of [Mg/Fe] increase substantially. This is not unexpected and has been extensively discussed in the literature (Gratton et al. 2004; Carretta et al. 2014; Carretta 2014). The large variation of Mg abundances is usually attributed to the nuclear processing associated with high temperature hydrogen burning and multiple star formation episodes. In such a scenario first generation massive stars evolve fast, converting their Mg into Al. Second generation stars, formed from the material of first generation stars, are

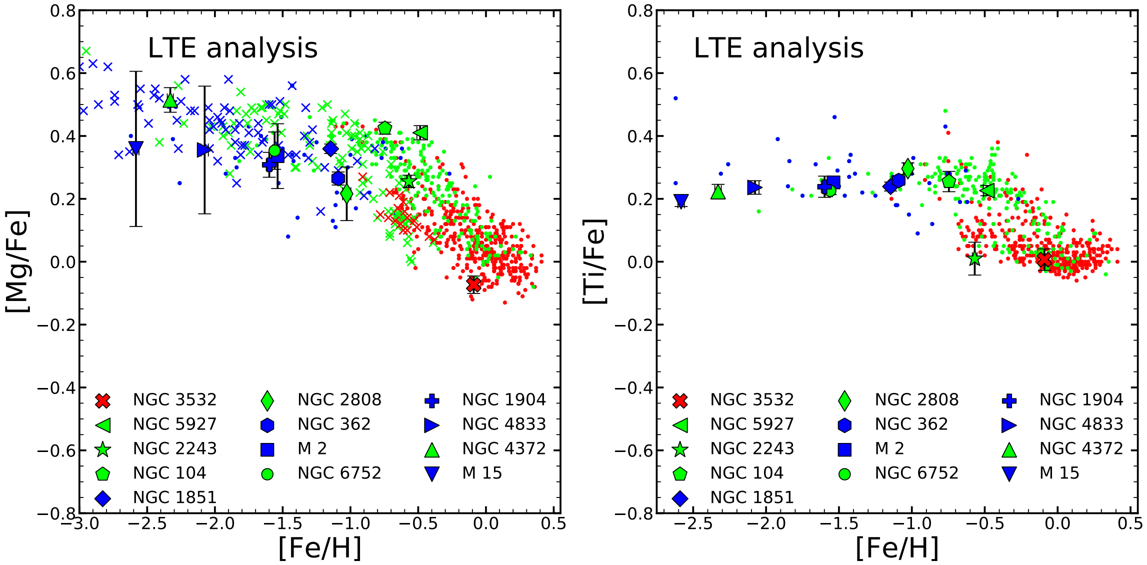

Figure 2.13: Mean LTE metallicities and [Mg/Fe] and [Ti/Fe] abundance ratios for all clusters and for Milky Way field stars from Bensby et al. (2014)(NLTE [Fe/H], LTE [Mg/Fe] and LTE [Ti/Fe] – small dots) and Bergemann et al. (2017)(1D LTE results – small crosses). Error bars represent the 1σ intra-cluster abundance variations. Colours are the same as in Fig. 2.12.

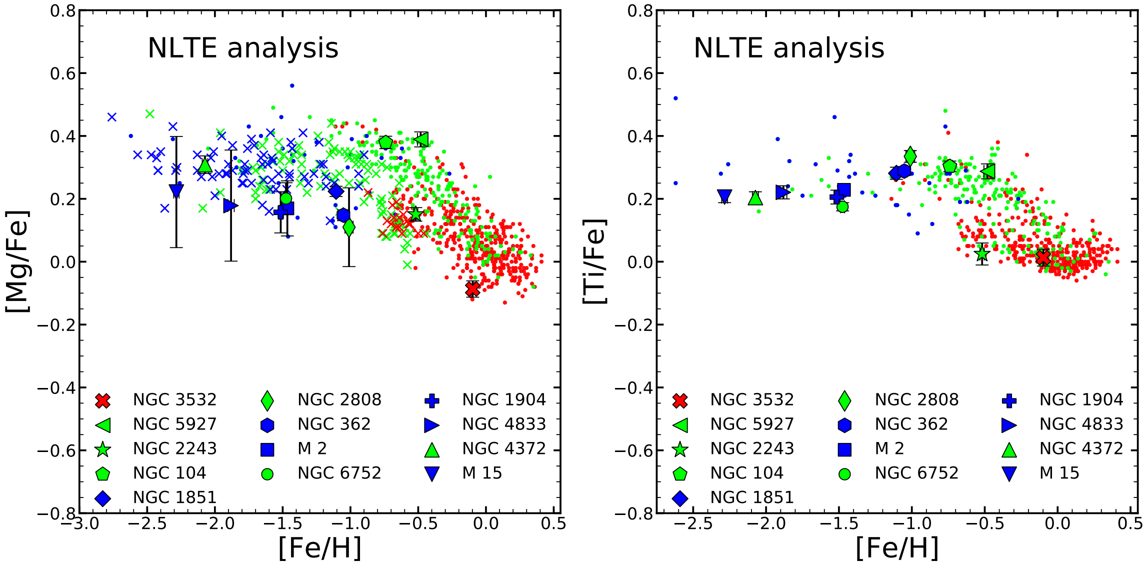

Figure 2.14: Mean NLTE metallicities and [Mg/Fe] and [Ti/Fe] abundance ratios for all clusters and for Milky Way field stars from Bensby et al. (2014)(NLTE [Fe/H], LTE [Mg/Fe] and LTE [Ti/Fe] – small dots) and Bergemann et al. (2017)(1D NLTE results – small crosses). Error bars represent the 1σ intra-cluster abundance variations. Colours are the same as in Fig. 2.12.

depleted in Mg and enriched in Al. The absence of any noticeable dispersion in [Ti/Fe] in all GCs corroborates this interpretation.

Notwithstanding the good agreement of our LTE results with earlier LTE studies, we find important differences between LTE and NLTE results (Fig. 2.14), which impact the astrophysical interpretation of the results. When comparing our NLTE abundances for globular clusters with the NLTE abundances of field stars, only two metal-rich clusters with the thick disk kinematics (NGC 104 and NGC 5927) and the metal-poor cluster NGC 4372 appear to be consistent with the field stars. All other metal-poor clusters are systematically depleted in [Mg/Fe] relative to the metal-poor disk and the halo. Additionally in Fig. 2.15 we compare our results with abundance ratios observed in three dwarf spheroidal galaxies (dSph) from Kirby et al. (2009); Hendricks et al. (2014), and Mucciarelli et al. (2017). These observations are shown as a sliding mean, which is computed using the metallicity bins of 0.25 dex. There is significant overlap of the metal-poor GCs with the Sculptor dSph, however it can be caused by the large scatter in this galaxy. The globular clusters at [Fe/H] ~ -1.5 dex are also overlapping with Sagittarius dSph. This may imply that the metal-poor clusters were not formed *in-situ*, but were accreted from disrupted dwarf satellite galaxies.

2.5 Conclusions

In this chapter we employed NLTE radiative transfer models and *the Payne* code to determine chemical abundances for 13 stellar clusters in the Milky Way. The observed spectra are taken from the third public data release of the Gaia-ESO survey, and we focus on the $R \sim 19\,800$ spectra taken with the Giraffe instrument. The NLTE synthetic spectra are computed using the model atoms presented in earlier works (Bergemann, M. & Gehren, T. 2008; Bergemann 2011; Bergemann et al. 2012, 2017). *The Payne* code is used to interpolate in the grids of synthetic spectra to maximise the efficiency of the analysis, where we simultaneously fit for all spectral parameters, exploring more information from the full spectrum. The spectral grids are computed at random nodes in stellar parameter space and a χ^2 minimisation is employed to find the best-fit stellar parameters and chemical abundances by comparing the models with the observations.

We validate our method and the models on the Gaia-ESO benchmark stars, for which stellar parameters are well constrained by parallaxes, asteroseismology, and interferometric angular diameter measurements. The calibration sample includes 19 main-sequence dwarfs, subgiants, and red giants in the [Fe/H] range from -2.5 to

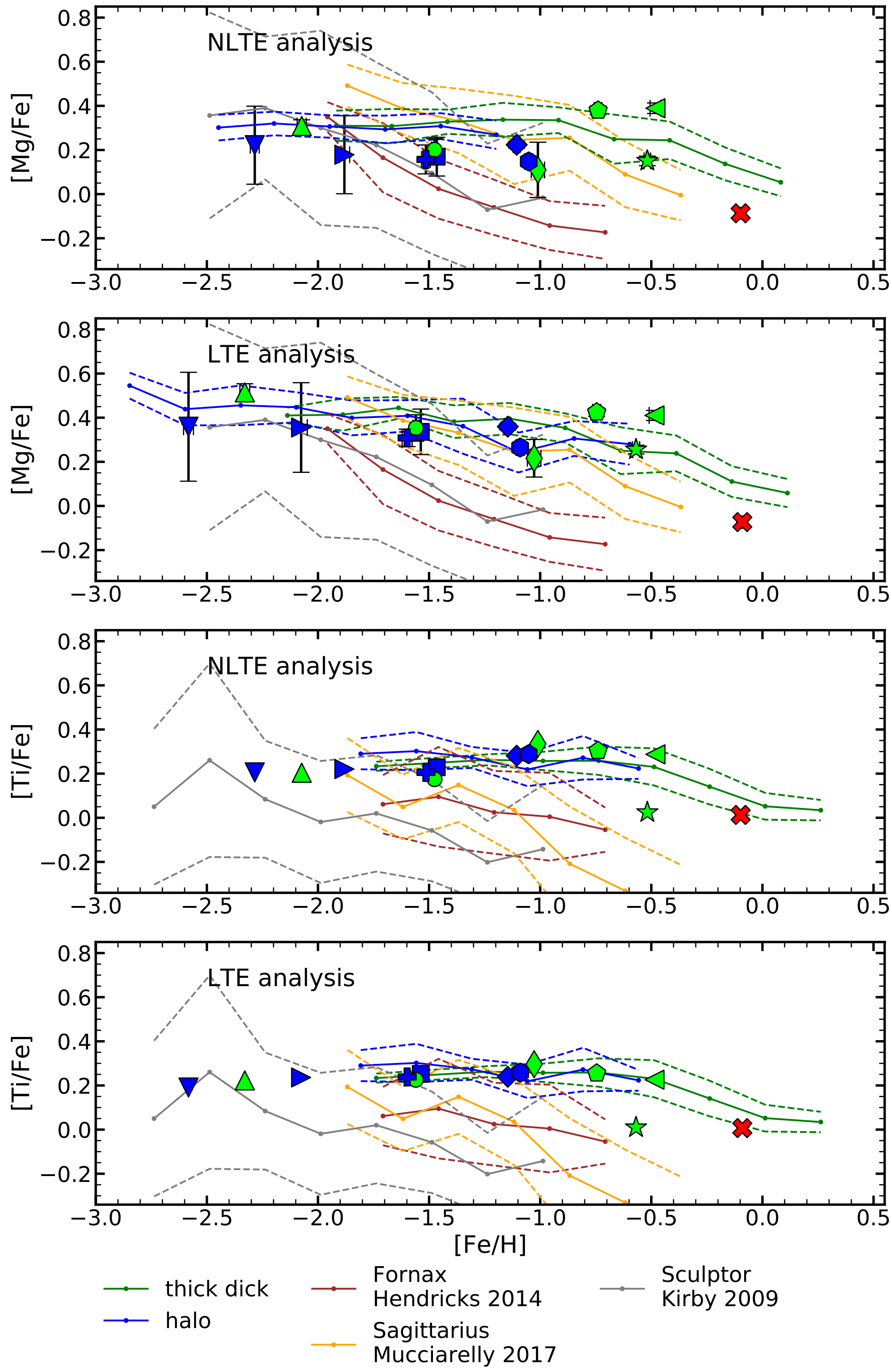

Figure 2.15: The average abundance ratios of the clusters in comparison with the Galactic halo, thick disk, and three dSph galaxies, shown as sliding mean with a 1σ interval. Colours and symbols are the same as in Fig. 2.12

0.3 dex with spectra taken at different exposure times spanning the S/N range of 100 to 2600 Å^{-1}. We find a very good agreement between our NLTE spectroscopic results and the independently determined stellar parameters. The residuals are within -29 ± 88 K in $T_{\rm eff}$, 0.09 ± 0.16 dex in log(g), and 0.02 ± 0.09 dex in [Fe/H]. The analysis of repeat observations of the same stars indicates the absence of a systematic bias or correlation of the abundance error with the quality the spectra within the full range of S/N probed in this work.

We compute stellar parameters and abundances for 742 stars in two open clusters and 11 globular clusters in the Milky Way galaxy. The typical S/N of the spectra is 200 Å^{-1}. We find that spectroscopic estimates of stellar parameters ($T_{\rm eff}$, $\log g$, and [Fe/H]) agree with evolutionary expectations, based on isochrones. However, different isochrones are needed to match the LTE and NLTE data. At low metallicity, the difference between LTE and NLTE parameters is significant, confirming earlier studies (i.e. Bergemann et al. 2012; Lind et al. 2012; Ruchti et al. 2013). The systematic error of LTE increases in proportionality with decreasing metallicity, and amounts to 300 K in $T_{\rm eff}$, 0.6 dex in $\log g$, and 0.3 dex in [Fe/H] for the RGB stars with $[\mathrm{Fe/H}]_{\rm NLTE} = -2.3$. The [Mg/Fe] abundance ratios are typically lower in NLTE compared to LTE. Our abundances show no significant trends with stellar parameters, supporting their relative accuracy.

Our results for the Galactic open and globular clusters can be summarised as follows:

- NGC 3532, a young metal-rich open cluster, is consistent in its chemical abundance pattern and its kinematics with the Galactic thin disk. The cluster is slightly depleted in Mg compared to the solar neighbourhood, although the difference is generally within the uncertainties of the abundance measurements.

- NGC 2243, a relatively old open cluster lies on the metal-poor end of the thin disk track, and shows a noticeable dispersion in [Fe/H], [Mg/Fe], and [Ti/Fe] ratios contrasting with the tight chemical patterns in the field stars. This is the only cluster in our sample that is represented by main-sequence and turn-off stars, and this spread likely has an astrophysical origin. In particular, the pronounced dip in [Fe/H] at the turn-off signifies the action of atomic diffusion consistent with depletion predicted by detailed stellar evolution models.

- Two metal-rich clusters with thick disk like kinematics NGC 104 and NGC 5927 are also very similar to the thick disk in their abundance ratios of [Mg/Fe] and [Ti/Fe]. They show small dispersions in all elements $\lesssim 0.06$ dex, which are much smaller then the typical systematic uncertainties of our measurements, and are consistent with being chemically homogeneous populations.

- The metal-poor clusters NGC 2808 and NGC 6752, despite being kinematically similar to the thick disk, appear to be depleted in [Mg/Fe] compared to the field stars, based on NLTE analysis. On the other hand, their [Ti/Fe] ratios are representative of the halo clusters.

- NLTE analysis suggests that the majority of metal-poor clusters with [Fe/H] < -1 dex and halo-like kinematics, show a prominent, ~ 0.15 dex, depletion of [Mg/Fe] compared to field stars of the same metallicity. This may indicate their *ex situ* formation history.

- NGC 2808 and NGC 1851 exhibit remarkably similar chemical abundance patterns and overlap in metallicity that reinforces the evidence for their common origin proposed in the literature.

- Large intra-cluster spreads in [Mg/Fe], compared to the field population, are seen in the clusters M 2, NGC 2808, NGC 4833 and M15, corroborating with the long-postulated scenario that globular clusters have undergone multiple episodes of star formation and self-enrichment. On the other hand, the clusters are homogeneous in [Ti/Fe].

- The metal-poor globular cluster NGC 4372 stands out in comparison with the other globular clusters with a similar metallicity. Its [Mg/Fe] spread is relatively small, consistent with the study by San Roman et al. (2015). Given our standard abundance uncertainties of ~ 0.1 dex, which exceed the intra-cluster dispersion, the cluster is homogeneous in [Fe/H], [Mg/Fe] and [Ti/Fe].

- For M15 and NGC 4833, which are the most metal-poor clusters in our sample, we find strong evidence for a multi-modality in [Mg/Fe]. However, our samples are too small to draw statistically robust conclusions on whether these clusters host two or more sub-populations.

The combination of NLTE models and *the Payne* is a powerful tool for homogeneous analysis of the stellar parameters and chemical abundances. Our results for a large sample of stars in wide range of metallicity suggests that NLTE effects are significant for metal-poor regime ([Fe/H] < -1) and should be always taken into account.

Chapter 3

Analysis of Gaia-ESO Milky Way field stars

3.1 Introduction

The stellar atmospheric abundances are presumed to reflect the chemical composition of the interstellar media from which they were born[1]. Combining this information with kinematics for a large stellar sample allows us to separate different stellar populations in the Milky Way and explore their evolution.

The main reservoir of Milky Way stars, the galactic disk, is divided into two components the thin and the thick disk, based on the results of stellar counts Gilmore & Reid (1983). The spectroscopic observations in the solar neighbourhood suggested that these disks have different chemical compositions: the thin disk contains more metal-rich and less α-enhanced stars in comparison with the thick disk (Adibekyan et al. 2012; Bensby et al. 2014). At the same time kinetically, thick disk is much hotter and rotates slower than the thin disk (Minchev et al. 2014). The analysis of the stellar ages suggests that the thick disk population is older then the thin disk (Haywood et al. 2013; Bensby et al. 2014; Bergemann et al. 2014; Buder et al. 2018a).

However the exact origin of these disk sub-structures, especially thick disk, remains poorly known and needs to be investigated. There are four main scenarios

---

[1] Several studies claim that atomic diffusion effects can be non-negligible (Gruyters et al. 2013; Bertelli Motta et al. 2018). However, these effects are not fully understood yet and thus are usually neglected in the Galactic archaeology.

that have been proposed to explain the origin of the thick disk:

- direct accretion of stars from disrupted satellites (Abadi et al. 2003),
- dynamical heating by an infalling satellites (Freeman 1987; Quinn et al. 1993; Villalobos & Helmi 2008; Villalobos et al. 2010),
- radial migration of the stars (Roškar et al. 2008; Schoenrich & Binney 2009a,b; Loebman et al. 2011),
- *in-situ* formation after gas-rich merger (Brook et al. 2004, 2007).

All such scenarios leave some imprints in the dynamical and chemical properties of the thick disk, which can be extracted from statistically significant stellar sample. For example, analysis of the orbital eccentricities distributions indicate a dominant formation mechanism, as proposed by Sales et al. (2009).

Many previous observational studies focused on the Galactic disk. For example, Ruchti et al. (2011) studied high-resolution spectra for the metal-poor stars, finding that the thick disk was formed primarily in the Galaxy, with direct accretion origin of stars from dwarf galaxies contributing little. Bovy et al. (2012) analysed a large sample of SEGUE low-resolution spectra and found that if the selection function of the survey is carefully taken into account the Galactic disk can be represented by a single population with no need for an additional thick disk at all. However, Bensby et al. (2014) found clear evidence that the solar neighbourhood contains two distinct populations in the [α/Fe]-[Fe/H] plane, based on 714 dwarf stars with high-resolution spectra. This study suggests that old and α-enhanced stars are born in inner Galactic regions, but young and low-α stars are formed in outer regions. The following analysis of large scale spectroscopic surveys (Recio-Blanco et al. 2014; Hayden et al. 2015) confirmed presence of bimodal structure in $[\alpha/\mathrm{Fe}]-[\mathrm{Fe/H}]$ plane, but when binned into small $[\alpha/\mathrm{Fe}]-[\mathrm{Fe/H}]$ bins, stars show a smooth transition between the thin and thick disks. Minchev et al. (2014) found interesting turnoffs in the velocity dispersions for high-[α/Fe] stars in RAVE DR6 giants, suggesting that several formation scenarios played a significant role in thick disk formation.

The Gaia-ESO spectroscopic survey (GES) (Gilmore et al. 2012) data are very useful to study disk evolution. First analysis of the GES high-resolution data was done by Bergemann et al. (2014) where the age-metalicity relation was studied and evidences for inside-out disk formation were found. Recio-Blanco et al. (2014); Mikolaitis et al. (2014) analysed the low resolution part of first internal GES data release and explored metallicity and velocity gradients for the thin and thick disk samples. Kordopatis et al. (2015); Guiglion et al. (2015) analysed the second internal

GES data release focusing on velocity dispersions and characterisation of high-[α/Fe] and low-[α/Fe] disk components. Hayden et al. (2017) have found that migration processes have played an important role in the evolution of the Milky Way using the forth internal GES data release.

In this chapter we apply analysis developed in the previous chapter to the full sample of Milky Way field stars, using the third public data release of Gaia-ESO survey. We combine our NLTE chemical abundances with high-quality astrometric information from the second data release of Gaia satellite mission (Gaia Collaboration et al. 2018) to explore the kinematics and chemistry of the Galactic disk in the context of the thick disk formation.

3.2 Spectral sample

We use the spectra of FGK stars observed within the Gaia-ESO spectroscopic survey (Gilmore et al. 2012; Randich et al. 2013). These spectra are now publicly available as a part of the third data release (DR3.1)[2]. The data were obtained with the Giraffe spectrograph (Pasquini et al. 2002) at the ESO (European Southern Observatory) VLT (Very Large Telescope). We use the spectra taken with the HR10 setting, which covers ~ 280 Å from 5334 Å to 5611 Å, at a resolving power of $R = \lambda/\Delta\lambda \sim 19\,800$. The average signal-to-noise ratio (S/N) of a spectrum ranges from 90 to 800 per Å with the majority of the spectra sampling the S/N in range of 120 Å^{-1}. All these stars have been previously analysed and have 1D LTE estimates of their spectral parameters and chemical abundances in the GES catalogue.

We selected only stars which were observed in Milky Way (MW) fields, not including the bulge, standard stars and stellar clusters. The distribution of the stars in the sky coordinates is shown in Figure 3.1. In total the spectral sample includes 6639 spectra. All these spectra were analysed using the same method as described in Chapter 2. The stars with spectroscopic parameters estimates close to edges of the synthetic model grid were excluded. All remaining 6457 stars have a 5D solution from Gaia DR2 (Gaia Collaboration et al. 2018) and a distance estimate from Bailer-Jones et al. (2018). Unfortunately, our stars are too faint ($G > 13$ mag) and do not have line-of-sight velocity estimates from Gaia RVS spectrograph (Katz et al. 2019), therefore we cannot compare our line-of-sight velocities with Gaia RV estimates and use distance estimates from Schoenrich et al. (2019). We checked that 5314 stars have a relative parallax uncertainty smaller than 20%. Many studies

---

[2] `http://archive.eso.org/wdb/wdb/adp/phase3_spectral/form?collection_name=GAIAESO`

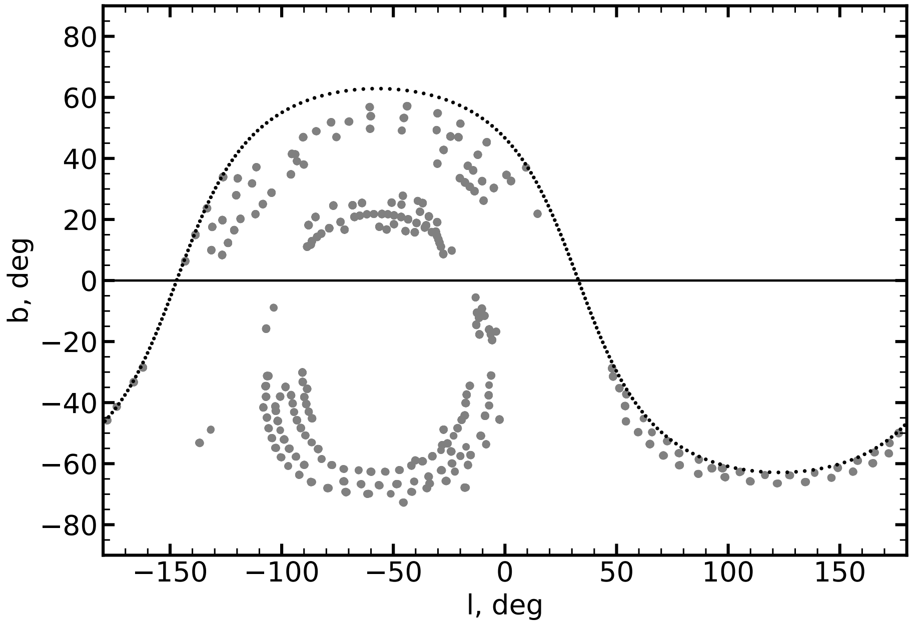

Figure 3.1: The Galactic coordinates for stars in our sample. The celestial and galactic equator are shown with dotted and solid lines respectively.

recommend to use only stars satisfying this criterion (Andrae et al. 2018). However, such a cut is less sensitive for bright stars and mostly removes faint stars with increasing distance (Luri et al. 2018). This changes age distribution of the observed population and introduces kinematic bias. We decided to keep all stars since a large fraction of the sample (18%) can be removed by this cut. We explore how such a cut can affect observed distributions in Section 3.5.

The Gaia colour-magnitude diagram (CMD) and Kiel ($T_{\rm eff}$-log(g)) diagram are shown in Figure 3.2. The CMD is computed using the distances from Bailer-Jones et al. (2018), assuming zero extinction and reddening for all stars. We find out that main sequence stars with $T_{\rm eff} < 5000$ K do not have realistic surface gravities, therefore we do not use them in further analysis. Thus our sample contains 5408 FG stars with reliable spectroscopic parameters, where vast majority (80%) are dwarf stars.

3.3 Kinematic and dynamics.

For all stars in the sample we computed Galactocentric coordinates and velocities using our line-of-sight velocities with proper motions from Gaia DR2 (Gaia

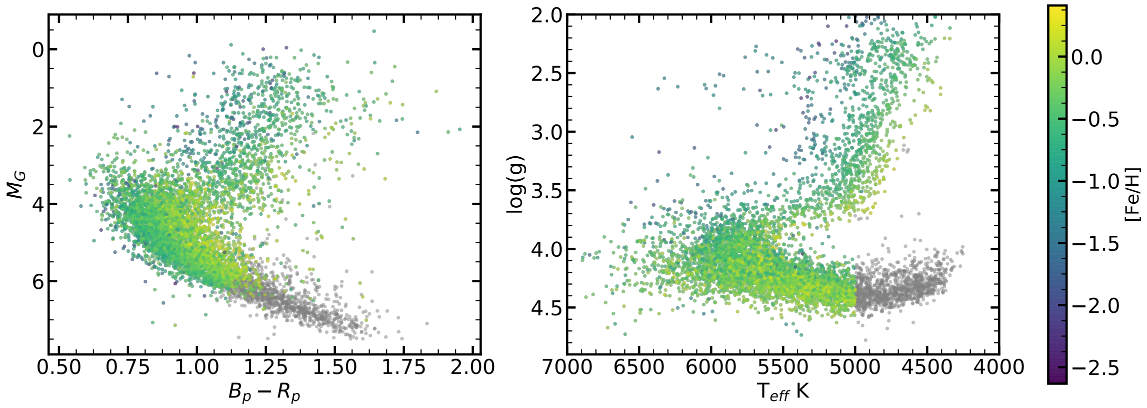

Figure 3.2: The Gaia colour-magnitude diagram (left panel) and The Kiel diagram (right panel) for our sample of Gaia-ESO MW field stars. The CMD is computed using distances from Bailer-Jones et al. (2018), assuming zero extinction and zero reddening. Note the cool main sequence end shown as grey dots. These stars were excluded from further analysis because of their non-realistic upturn in log(g).

Collaboration et al. 2018) and distances from Bailer-Jones et al. (2018), see Section 1.5.1. Such purely geometric distances were derived in Bayesian interference taking a length-scale $L(l, b)$[3] as a prior. For each star we run 1000 Monte-Carlo realisations, sampling proper motions, line-of-sight velocities assuming a Gaussian uncertainty distribution. The distances were sampled using an asymmetric uncertainty distribution:

$$d_i = \begin{cases} d - |N(0, d - d_{min})| & i \leq 500 \\ d + |N(0, d_{max} - d)| & i > 500 \end{cases}, i = 1, .., 1000, \tag{3.1}$$

where $N(\mu, \sigma)$ is a Gaussian distribution and values d, d_{min}, d_{max} are provided in Bailer-Jones et al. (2018). We plot example of this sampling for two stars of different parallax quality on Figure 3.3. The star with precise parallax, $\sigma(\varpi)/\varpi$ =2%, has almost symmetric distribution, but star with large uncertainty, $\sigma(\varpi)/\varpi$ =47%, shows a long tail extended towards large distances.

We computed the median and standard deviation across 1000 Monte-Carlo realisations as an estimated value and error for position and velocity of each star. Thanks to the high quality of Gaia data, typical errors, taken as median across all stars, are very small: $\sim$ 0.06 kpc in coordinates and $\sim$ 3 $\mathrm{km\,s^{-1}}$ in velocities. We show error distributions in Figure 3.4.

---

[3] Length-scale is based on Gaia DR2 mock catalogue (Rybizki et al. 2018).

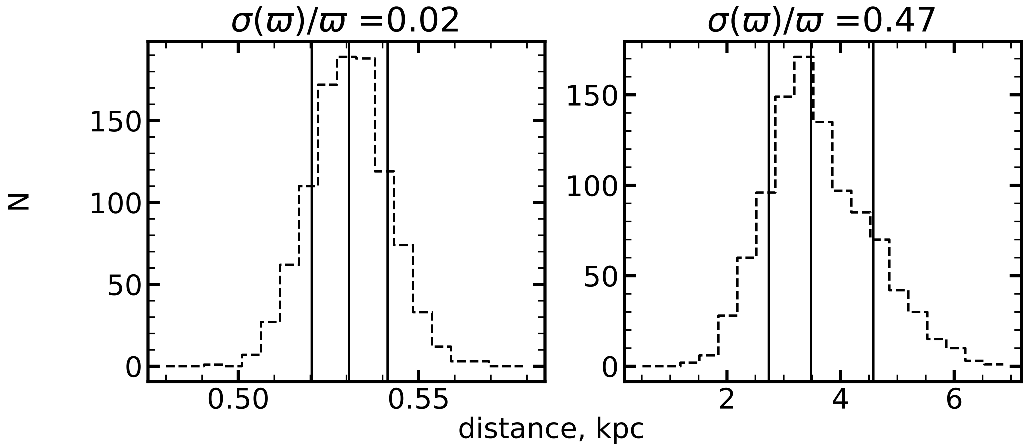

Figure 3.3: The distribution of the distance sampling for two stars. Left panel star with small parallax uncertainty and right panel star with large parallax uncertainty. Vertical lines are d_{min}, d, d_{max} distances (Bailer-Jones et al. 2018) respectively.

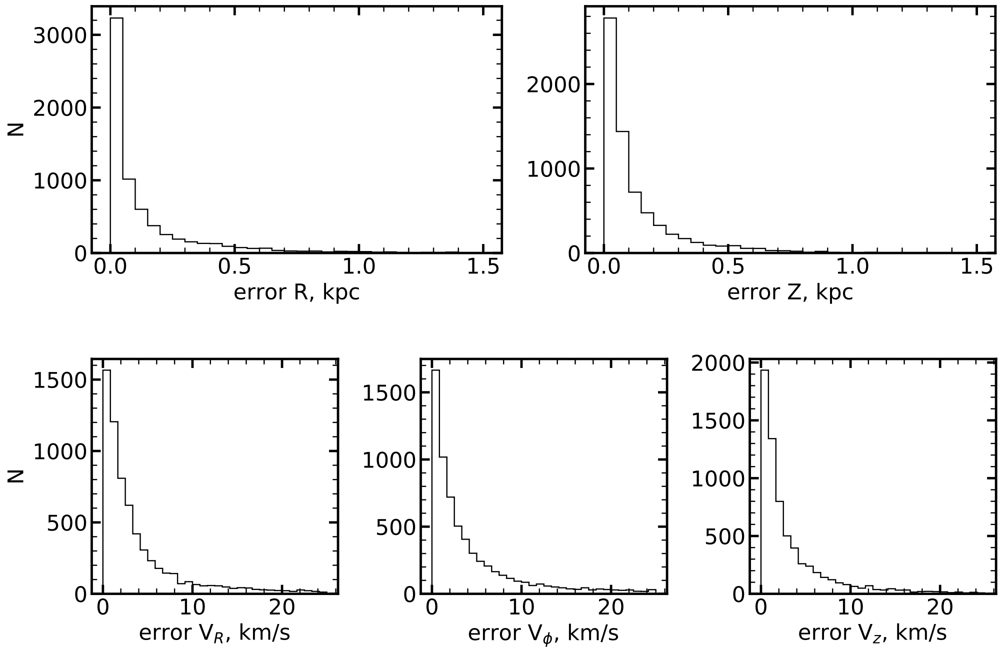

Figure 3.4: The uncertainties in cylindrical coordinates (top panels) and in velocity components (bottom panels).

The velocities and positions allow us to compute orbits for all stars by adopting a model of the Galactic potential. We used *Galpy* (Bovy 2015) with the Stäckel analytic approximations outlined in Mackereth & Bovy (2018) and the default *MWPotential2014* potential, that includes a bulge, disk and halo (see Bovy (2015) for details) to estimate $e, Z_{max}, r_{peri}, r_{apo}$ using positions and velocities from the previous 1000 Monte-Carlo realisations. The final value and uncertainty are taken as a median and a standard deviation. The typical uncertainties are $\sigma(e) = 0.02$ for eccentricity and $\sigma(Z_{max})$, $\sigma(r_{peri})$, $\sigma(r_{apo}) = 0.10,\ 0.13,\ 0.11\,\mathrm{kpc}$ for maximal height, pericentric and apocentric distances respectively (taken as median across all stars).

3.4 Galactic population selection

Separation of disk populations is not a trivial operation. Many studies utilised stellar kinematics (Ruchti et al. 2011; Bensby et al. 2014; Xing & Zhao 2018) to assign stars into the thick and thick disks. However, kinetically defined disks heavily depend on assumed kinematic model and can have significant mixture of the high-[α/Fe] and low-[α/Fe] populations (Schoenrich & Binney 2009a). Another method is chemical separation based on position of less populated region in the [α/Fe]-[Fe/H] plane (Adibekyan et al. 2012; Recio-Blanco et al. 2014; Mikolaitis et al. 2014). Such selection is more robust, although is not universal since each study introduces it's own separation line.

As an exercise we applied kinematic selection criteria from Bensby et al. (2014) to assign populations for each star. In this method we assume that the Galactic velocities (U_{LSR}, V_{LSR}, W_{LSR}) have a Gaussian distribution given by the equation (Bensby et al. 2014):

$$f(U,V,W) = k \cdot \exp\left(\frac{U_{\mathrm{LSR}}^2}{2\sigma_U^2} - \frac{(V_{\mathrm{LSR}} - V_{\mathrm{asym}})^2}{2\sigma_V^2} - \frac{W_{\mathrm{LSR}}^2}{2\sigma_W^2}\right), \tag{3.2}$$

where

$$k = \frac{1}{(2\pi)^{3/2}\sigma_U\sigma_V\sigma_W}. \tag{3.3}$$

Here, σ_U, σ_V, and σ_W are the characteristic velocity dispersions, and V_{asym} is the asymmetric drift, and their values are listed in Table 3.1 (Bensby et al. 2014). U_{LSR}, V_{LSR}, W_{LSR} are the stellar velocity relative to Local Standard of Rest. By dividing probabilities of the thick disk (TD), the thin disk (D), and halo (H), we obtain the relative probabilities for the thick-disk-to-thin-disk (TD/D) and the thick-disk-to-halo (TD/H) as follows:

$$\mathrm{TD/D} = \frac{X_{\mathrm{TD}} \cdot f_{\mathrm{TD}}}{X_{\mathrm{D}} \cdot f_{\mathrm{D}}}, \tag{3.4}$$

$$\mathrm{TD/H} = \frac{X_{\mathrm{TD}} \cdot f_{\mathrm{TD}}}{X_{\mathrm{H}} \cdot f_{\mathrm{H}}}. \tag{3.5}$$

Here, X is the observed fraction of stars for the populations in the solar neighbourhood, and thus X_{TD},X_{H} and X_{D} represent the fraction for the thick disk, halo and the thin disk, respectively. Their values are listed in Table 3.1. f_{TD}, f_{H} and f_{D} represent the Gaussian distribution of Galactic velocities for the thick disk, halo and thin disk, and they can be calculated with Eq. 3.2 and Eq. 3.3 for a given star with Galactic velocities (U_{LSR}, V_{LSR}, W_{LSR}) . TD, H and D are the probabilities that the given stars belong to the thick disk, halo and the thin disk, respectively. We selected TD/D > 2 (including those stars that are two times more likely to be thick disk stars than thin disk stars) from the high-[α/Fe] population to be the thick disk stars, and those with TD/D < 0.5 from the low-[α/Fe] population as the thin disk stars. We assign a star to the halo if TD/H< 0.5 or total velocity $V_{\mathrm{tot}} = (U_{\mathrm{LSR}}^2 + V_{\mathrm{LSR}}^2 + W_{\mathrm{LSR}}^2)^{1/2} > 180\,\mathrm{km\,s^{-1}}$.

These criteria assign 3118 stars to the thin disk, 1332 to the thick disk stars and 206 as halo stars. For 752 stars we cannot determine the explicit population because they are in between the thin and thick disk ($0.5 <$ TD/D < 2). We show the results of this operation in Figure 3.5. The top panel shows the spatial distribution of the stars in cylindrical coordinates, the middle panel is a Toomre diagram and the bottom panel shows the cylindrical velocity components. The thick disk stars are represented by green dots, thin disk stars are red dots while halo stars are blue dots. We can see that thin disk stars are mostly concentrated in an interval ±1kpc around the Galactic mid-plane. The thick disk stars, as expected, surround the thin disk up to 3 kpc vertically. However, some disk stars appear even at $Z \sim -4$kpc. The halo stars are uniformly distributed at all distances from mid-plane.

In the Toomre diagram we show that halo stars have a large total velocity relative to the Local Standard of Rest. Also, the thin and thick disk overlap in a small region around $V_{\mathrm{LSR}} = 0, (U_{\mathrm{LSR}}^2 + W_{\mathrm{LSR}}^2)^{1/2} = 70\ \mathrm{km\,s^{-1}}$. The dashed lines show the values of the total spatial velocity $V_{\mathrm{tot}} = (U_{\mathrm{LSR}}^2 + V_{\mathrm{LSR}}^2 + W_{\mathrm{LSR}}^2)^{1/2} = 50, 100, 150, 200$ km s^{-1}.

In cylindrical coordinates we can see that all thin disk stars occupy a small ellipse centred at $V_R = 0, V_\phi \sim 230\,\mathrm{km\,s^{-1}}$, spanning $\sim 150\,\mathrm{km\,s^{-1}}$ in V_R and

Table 3.1:: Kinematic parameters of the Galactic populations.

	X	σ_U km/s	σ_V km/s	σ_W km/s	V_{asym} km/s
Thin disk (D)	0.94	35	20	16	-15
Thick disk (TD)	0.0585	67	38	35	-46
Halo (H)	0.0015	160	90	90	-220

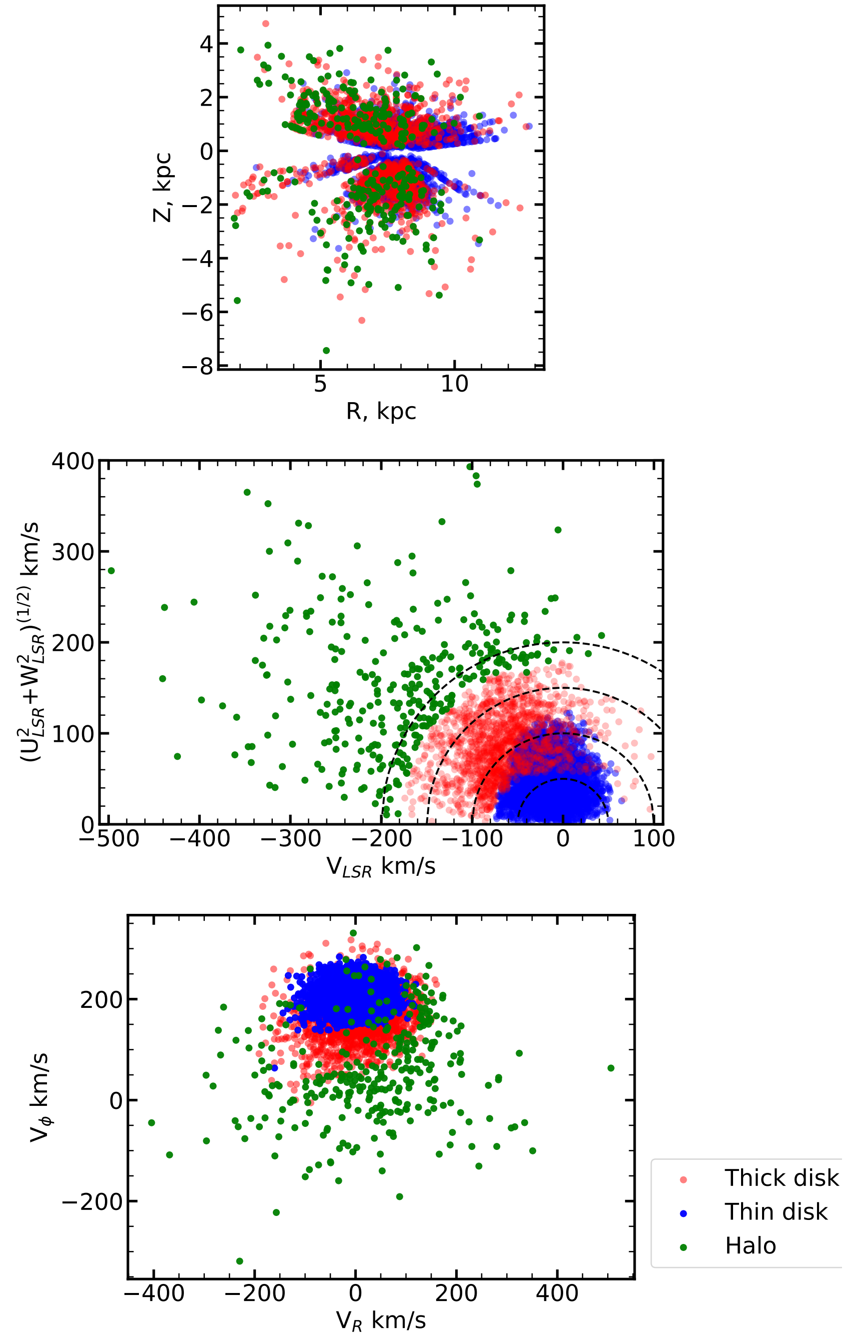

Figure 3.5: The spatial and kinematic distributions for stars in our sample. The top panel shows spatial distribution of the stars, the middle panel is a Toomre diagram and the bottom panel shows the cylindrical velocity components. The populations were assigned using the kinematic criteria.

$\sim 100\,\mathrm{km\,s^{-1}}$ in V_ϕ. The thick disk population spans roughly two times the large region with mean $V_\phi = 200\,\mathrm{km\,s^{-1}}$. The halo stars are distributed around zero with V_ϕ, V_R in the range $\pm 200, 350\,\mathrm{km\,s^{-1}}$ respectively. A significant part of the halo stars have a relatively high metallicity [Fe/H] ~ -1 dex, therefore they can be part of the "accreted" halo (Belokurov et al. 2018).

In all following Figures we use same colours to distinguish different populations: "red" for the high-[α/Fe] thick disk, "blue" for the low-[α/Fe] thin disk and "green" for the halo stars.

In Figure 3.6 we show the [Mg/Fe]-[Fe/H] distribution with contours for the kinetically selected thin/thick disk populations, which are shown as red/green lines. It is clear that if we use such a selection our thick disk will contain a significant number of low-α stars. Therefore, for further analysis we decide to use a purely chemical selection, based on [Mg/Fe], where kinematic selection is used only to select halo stars in the sample.

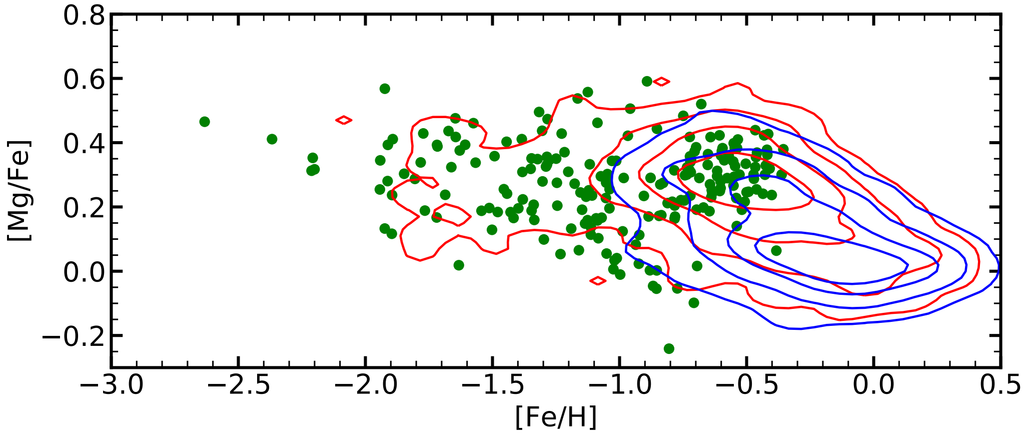

Figure 3.6: The results of the kinematic selection of the stars in our sample. Contours show the thick disk as red lines and thin disk as blue lines. They are shown for areas containing 33%, 66%, 90% and 99% of the data-points. Halo stars are shown with green dots.

The high-[α/Fe] and low-[α/Fe] populations are usually separated by a dividing line that goes through the less populated "gap" in the [α/Fe]-[Fe/H] abundance distribution (Adibekyan et al. 2012; Mikolaitis et al. 2014; Recio-Blanco et al. 2014). In this work we use [Mg/Fe] as a representation of [α/Fe]. As shown in the left panel of Figure 3.7 we split the sample into six metallicity bins and determine four separation points ([Fe/H], [α/Fe]): (-1.0, 0.16), (-0.5, 0.16), (0.0, 0.1), (0.5, 0.1) dex. The separation curve is the simple linear connection of these separation points. The high-[α/Fe] population is defined as stars above the separation line plus 0.09 dex (thick dashed line in the left panel of Figure 3.7), while the low-[α/Fe] population is defined as stars below the separation curve minus 0.09 dex. The width of the interval around separation line was taken as a typical uncertainty in [Mg/Fe] from our analysis of the stellar clusters in Table 2.4. The high-[α/Fe] population extends from [Fe/H] $\approx$ -2.2 to 0.0 dex and the low-[α/Fe] population have [Fe/H] from $\approx$ -0.8 to 0.4 dex.

In total, we selected 5202 stars as a full disk sample, where 1284 stars were assigned as a high-[α/Fe] disk and 1498 stars as low-[α/Fe]. We did not include 2420 stars close to separation line to reduce a possible cross-contamination due to [Mg/Fe] uncertainties. In the full disk sample 174 stars have metallicity [Fe/H] < -1 dex.

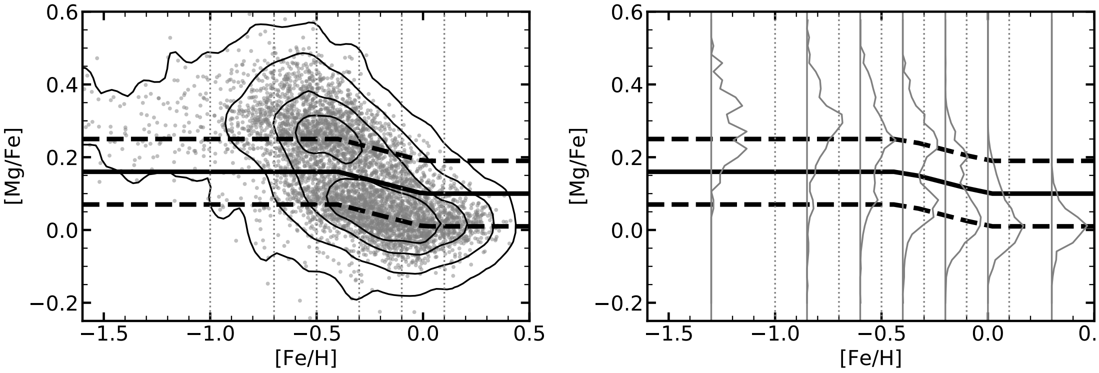

Figure 3.7: Chemical separation line used in this work. Left panel: abundances of Mg relative to iron versus [Fe/H]. Contour lines show for areas containing 33%, 66%, 90% and 99% of the data-points. Right panel: normalised distributions of [Mg/Fe] computed for different metallicity bins.

We verify our separation using azimuthal velocity distributions. In Figure 3.8 the distributions of azimuthal velocity are shown for metal-rich stars in the upper panels and for metal-poor stars in the bottom panels. In each panel, high-[α/Fe] population has lower mean V_ϕ than low-[α/Fe] population, as expected for the thick and thin disks. The intermediate component is well mixed by high-[α/Fe] and low-[α/Fe] populations. Additionally, we can see that the relative number of the high-[α/Fe] stars is decreasing with increasing galactocentric radius in comparison to number of low-[α/Fe] stars. This may imply that the thick disk have a shorter scale length than the thin disk (Bensby et al. 2011; Cheng 2012).

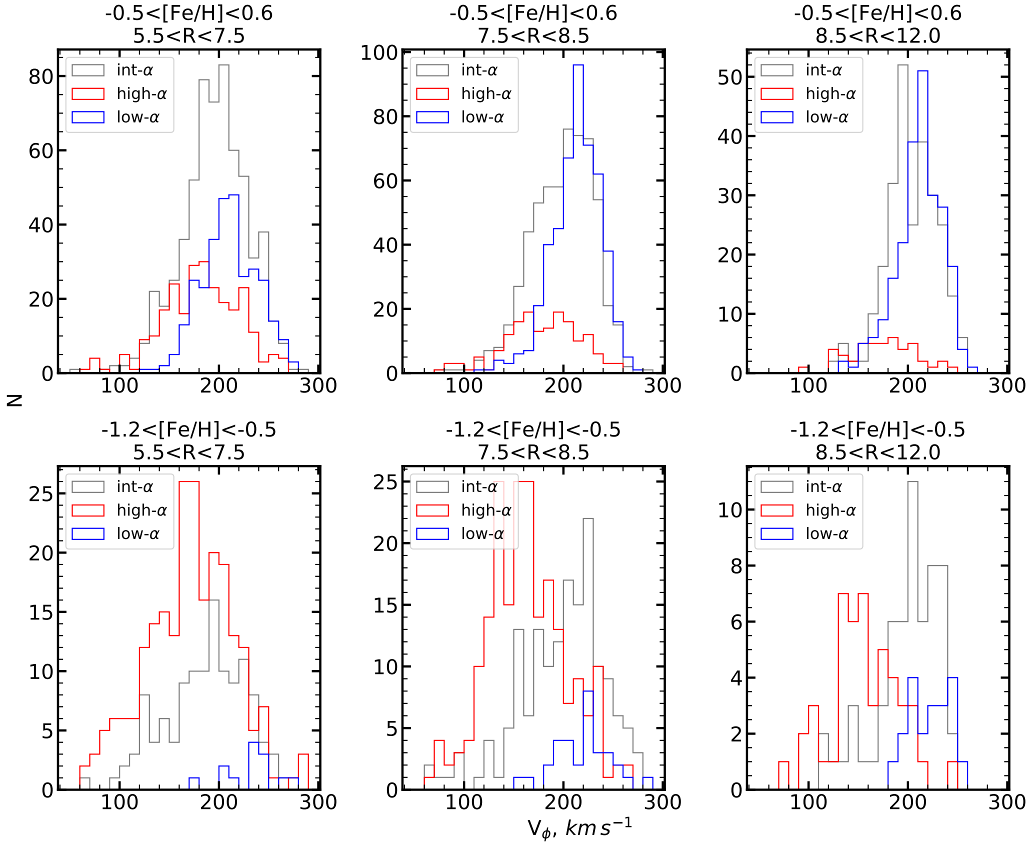

Figure 3.8: Distributions of V_ϕ computed for three $[\alpha/\mathrm{Fe}]$ populations at the different Galactocentric radii and metallicity bins.

3.5 Survey selection function and an impact of the parallax quality cut

The Gaia-ESO fields were selected to represent the main sequence stars, the turn-off stars and red giants branch stars centred on the red clump (Stonkutė et al. 2016). The selection was based on magnitudes and colours using photometry from the *VISTA* hemisphere survey catalogue (McMahon et al. 2013). The target stars were distributed between two selection boxes :

$$\text{Blue} = \begin{cases} 0.0 \leq (J - K_s) \leq 0.45 \\ 14 \leq J \leq 17.5 \end{cases}, \ \text{and Red} = \begin{cases} 0.4 \leq (J - K_s) \leq 0.7 \\ 12.5 \leq J \leq 15.0 \end{cases} \tag{3.6}$$

with relative ratio “Blue box”:“Red box”≈4:1. We can explore how survey selection effects can bias [Fe/H] and e distributions in our stellar sample adopting weights from Stonkutė et al. (2016). Such weights were computed for each star observed in the given Milky Way field as

$$W = \frac{N_A}{N_F}\frac{N_O}{N_B}, \tag{3.7}$$

where N_A is the number of stars with allocated spectrograph fibres, N_F is the total number of stars in the field of view (25 arcmin), N_B is the total number of stars inside a 2D bin (0.5 mag in J × 0.05 mag in $J - K_s$) in the selection box on the colour magnitude diagram for the field of view and N_O is the number of stars that have successful observations in this bin.

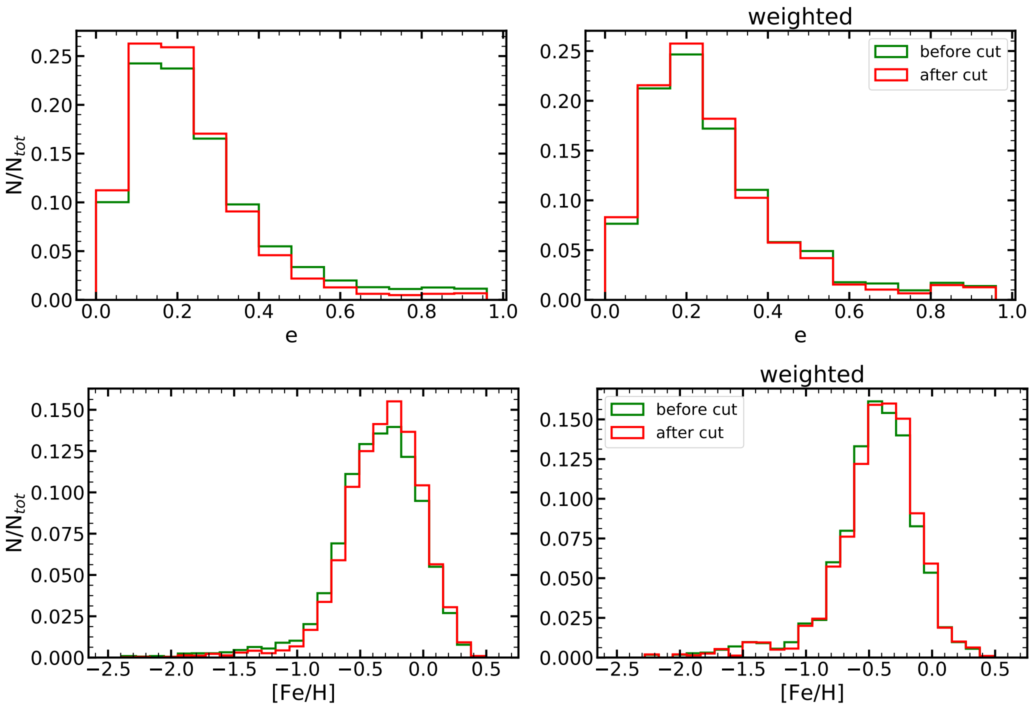

Figure 3.9: Eccentricities (upper panels) and metallicities (lower panels) distributions before and after the parallax quality cut. Left panel shows observed distribution, right panel shows distributions corrected using weights from Stonkutė et al. (2016).

If we apply a parallax quality cut $\sigma(\varpi)/\varpi < 0.2$ we remove almost one sixth of the stellar sample. We explore an impact of such selection operations on observed metallicity and e distributions of the full sample in Figure 3.9. The parallax cut is rejecting majority of the faint stars at large distances and leaving only bright ones. It biases eccentricity distribution to lower e by removing stars on highly elongated orbits. This is due to the fact that high-e stars mostly can be found at large heights from the Galactic plane and therefore they will be affected. The similar effect is seen for the metallicity. If there is vertical metallicity gradient in the Galactic disk such parallax cut will reduce number of metal-poor stars at high altitudes. The total distribution is slightly shifted to the high metallicity end. However, if these distributions are corrected for the selection function effects, shift due to parallax cut is smaller, but is not gone completely. Therefore, in the following sections we always use full sample, without parallax cut, and always apply weights from Stonkutė et al. (2016) to correct selection bias in the distributions.

3.6 Results

3.6.1 Eccentricity and metallicity distributions

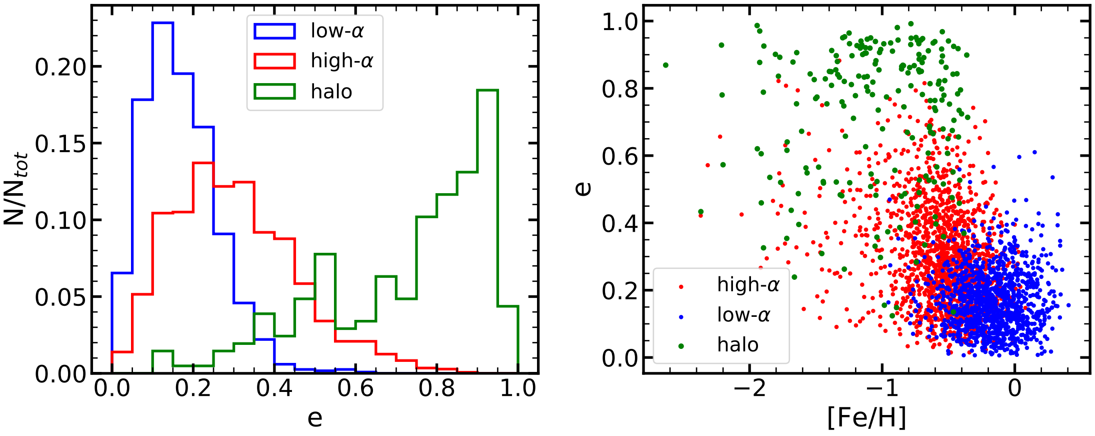

Figure 3.10: Eccentricities for low-[α/Fe] and high-[α/Fe] disks and halo. Left panel shows observed distribution corrected using weights from Stonkutė et al. (2016). Right panel shows e versus [Fe/H].

Orbital eccentricity distributions are presented in the left panel of the Figure 3.10. As expected, thin disk stars have nearly circular orbits and a narrow distribution with peak eccentricity at $e \sim 0.10 - 0.15$. The thick disk stars have larger eccentricities with a wider distribution and maximum at $e \sim 0.20 - 0.25$. They also show high-e tail down to $e = 0.8$. The halo stars mostly have very high eccentricities, which may indicate their accretion origin. In the right panel of the Figure 3.10 we present e-[Fe/H] diagram. Low-[α/Fe] stars are occupying relatively small region in the lower right corner of the plot, but several stars with [Fe/H] > 0 dex have relatively large eccentricity values $e > 0.4$. According to Hayden et al.

(2017) such stars may migrate from central regions of the Galaxy. At metallicity [Fe/H] ~ -0.6 dex high-[α/Fe] population have highest density and it smoothly span to the high-e end at $e \sim 0.8$. Halo stars show slight over-density in the high eccentricity regime, although some of them have almost near-circular orbits with $e \sim 0.1$.

In Figure 3.11 we present weighted metallicity distribution functions for the stars in our sample. The halo distribution shows presence of the relatively metal-rich stars with [Fe/H] ~ -0.75 dex and several other peaks with low-metallicity tail down to [Fe/H] $= -2.7$ dex. The full disk have maximum at [Fe/H] ~ -0.25 dex, with the high-[α/Fe] and the low-[α/Fe] components having their maximal values at [Fe/H] ~ -0.5, [Fe/H] ~ -0.2 dex respectively. The high-[α/Fe] disk also have a low-metallicity tail, indicating the presence of the metal-weak thick disk stars.

3.6.2 Orbital properties

We explore orbital properties for different populations in Figure 3.12. The low-[α/Fe] stars mostly populates galactocentric distances from $r_{peri} = 4 - 10$ kpc to $r_{apo} = 6 - 15$ kpc and do not move away from the Galactic mid-plane. The high-[α/Fe] stars have orbits with $r_{peri} = 2 - 10$ kpc to $r_{apo} = 2 - 15$ kpc and can be found at heights above 9 kpc. The halo stars mostly have very elongated orbits with high-e and come close to the Galactic center and then move to to $r_{apo} = 6 - 30$ kpc. Their orbits also can be highly inclined with respect to the Galactic mid-plane and reach heights of 20 kpc. We can see that some of the halo stars overlaps with high-[α/Fe] population at [Fe/H] > -1 in the Z_{max} and r_{apo} planes. The similar

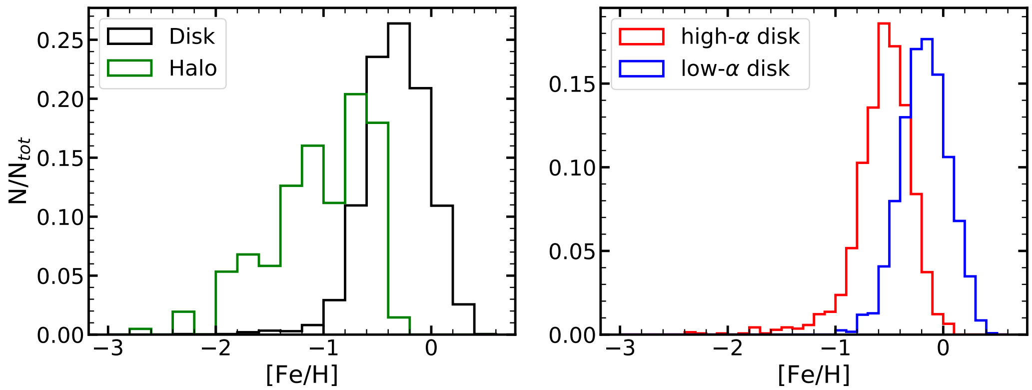

Figure 3.11: Weighted metallicity distributions. Left panel shows distribution for the halo and the full disk samples, right panel shows distribution for low-[α/Fe] and high-[α/Fe] disks components.

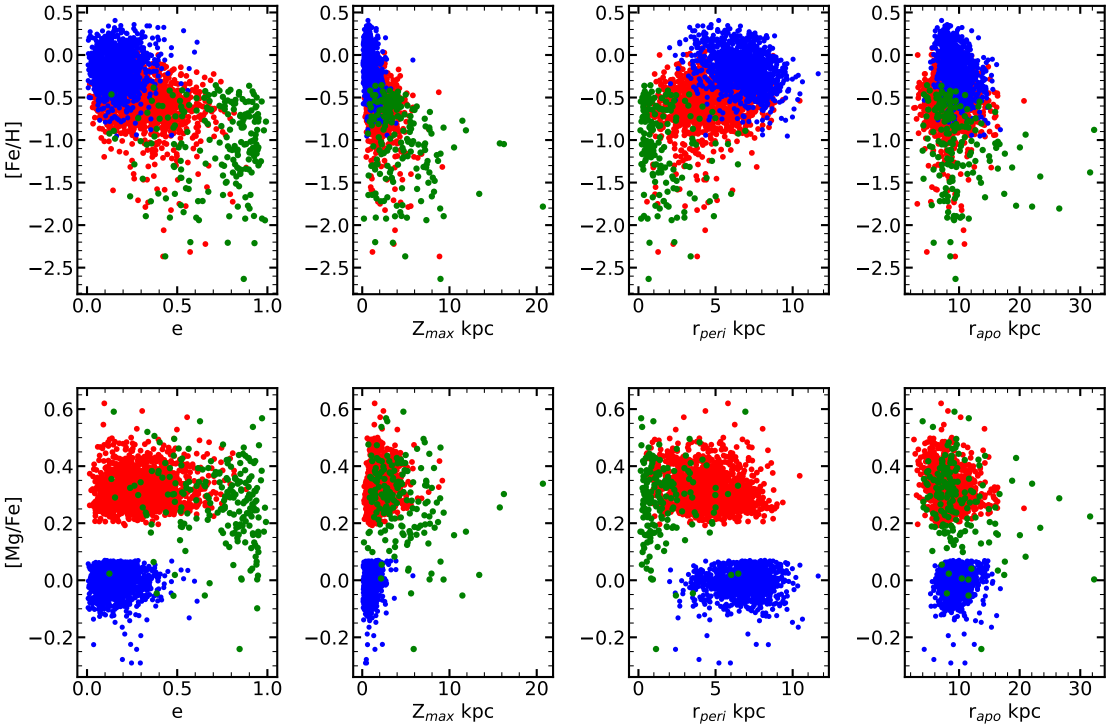

Figure 3.12: Chemical abundances as a function of eccentricity, maximal height, r_{peri} and r_{apo} distances respectively. Top panels: metallicity, bottom panels: magnesium to iron ratio. Colours are the same as in Figure 3.10

effect also visible in [Mg/Fe]-[Fe/H] plane in Figure 3.6. Some of them can be disk stars, miss-classified as a halo based on their high velocity with respect to the local standard of rest $V_{tot} > 180$ km s^{-1}. However, the majority of the halo population is clearly separated from the high-[α/Fe] disk stars if we use eccentricity and pericentric distances. The stars with largest apocentric distances r_{apo} are mostly have [Mg/Fe] smaller than mean halo value. In combination with the large eccentricities and height it may indicate that they were accreted from dwarf satellites of the Milky Way.

3.6.3 Chemical gradients with R and $|Z|$

We use our abundances and cylindrical coordinates to compute the observed gradients of metallicity with R and $|Z|$, as well as the gradient of [Mg/Fe] with $|Z|$ for the high-[α/Fe] and low-[α/Fe] disk populations. All gradients have been calculated using the slope of the line fitted with weighted least-square minimisation.

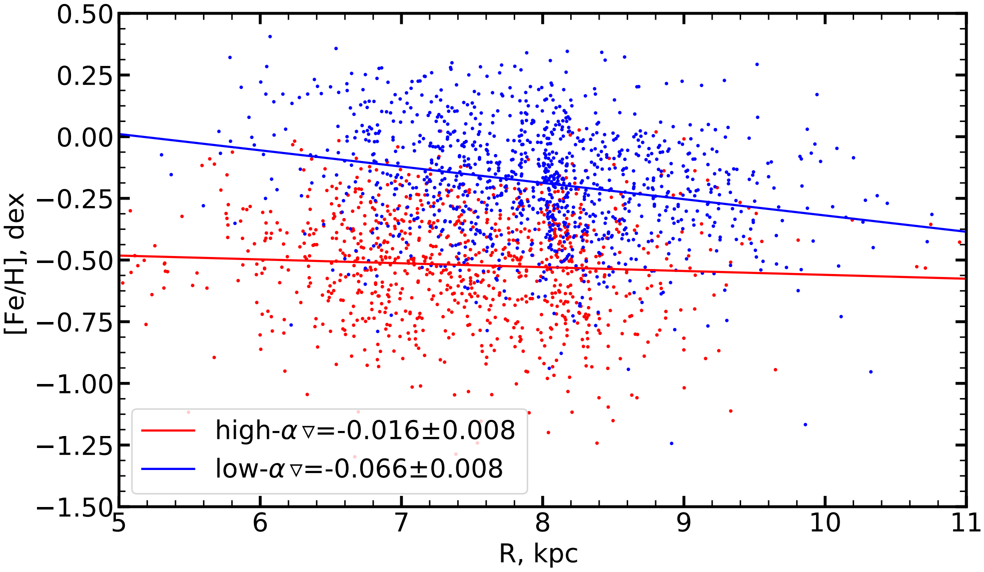

Figure 3.13: Radial metallicity gradients.

In Figure 3.13 we display radial metallicity gradients. We find an almost flat gradient for the high-α disk $\mathrm{d[Fe/H]}/\mathrm{d}R = -0.016 \pm 0.008$ dex kpc^{-1} and a slightly negative gradient for low-α disk $\mathrm{d[Fe/H]}/\mathrm{d}R = -0.066 \pm 0.008$ dex kpc^{-1}.

The vertical metallicity gradients are presented in the top panel of the Figure 3.14. For the thick disk the slope is $\mathrm{d[Fe/H]}/\mathrm{d}|Z| = -0.128 \pm 0.010$ dex kpc^{-1}. For the thin disk vertical metallicity gradient is much steeper $\mathrm{d[Fe/H]}/\mathrm{d}|Z| = -0.145 \pm 0.018$ dex kpc^{-1}.

The [Mg/Fe] abundance ratio gradients with vertical distance for the thin disk and thick disk stars are given in bottom panel of the Figure 3.14. The [Mg/Fe] vertical gradient of the thin disk is $\mathrm{d}[\alpha/\mathrm{Fe}]/\mathrm{d}|Z| = +0.023 \pm 0.002$ dex kpc^{-1}. For a thick disk we found a similar gradient of $\mathrm{d}[\alpha/\mathrm{Fe}]/\mathrm{d}|Z| = +0.017 \pm 0.004$ dex kpc^{-1}.

Our results suggests that radial and vertical metallicity gradients become flatter in transition from the thin to the thick disk. The vertical [Mg/Fe] gradient does not change in that transition. These results are consistent with the previous studies by Recio-Blanco et al. (2014), Mikolaitis et al. (2014) and Duong et al. (2018).

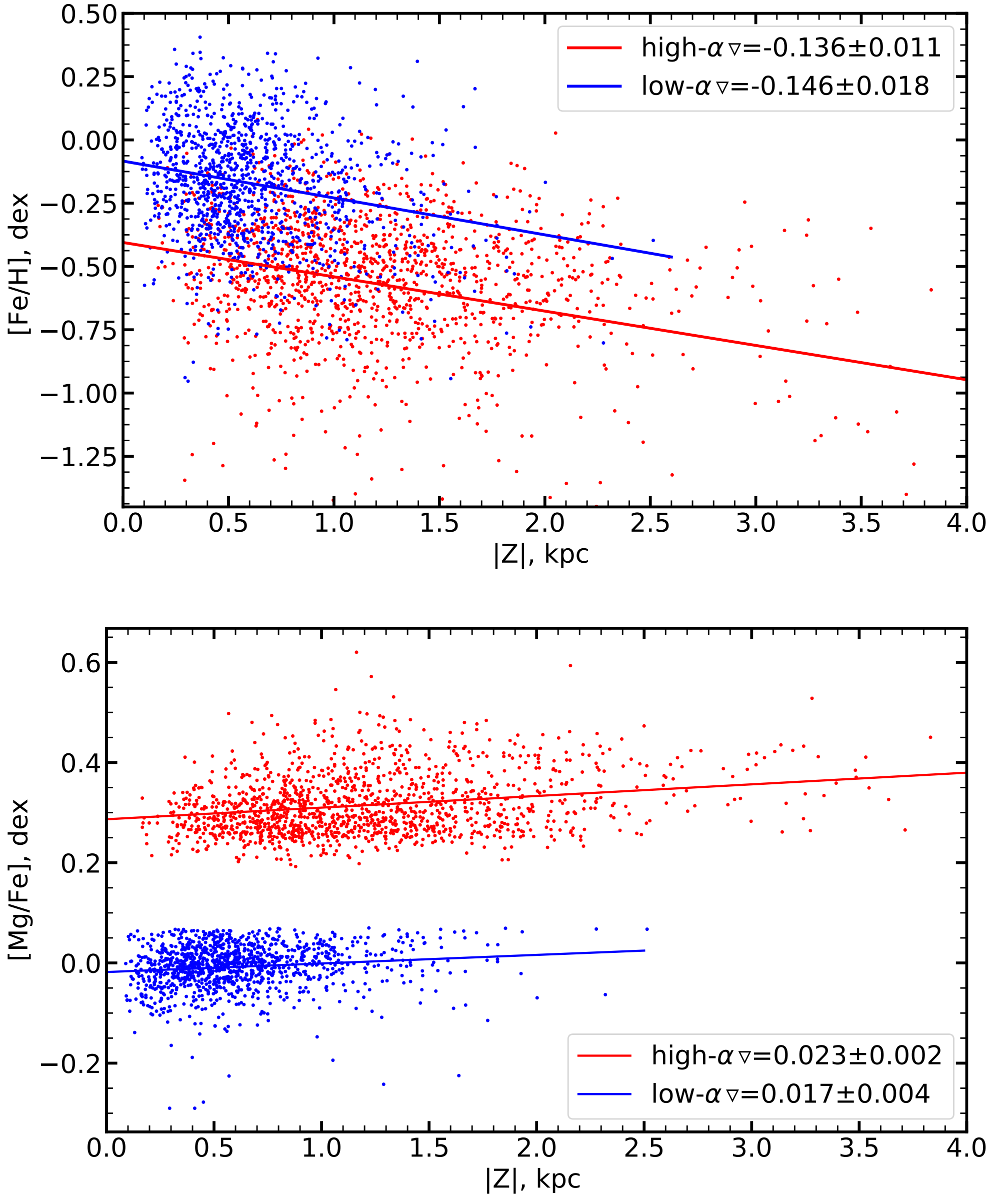

Figure 3.14: Vertical metallicity (top panel) and [α/Fe] (bottom panel) gradients.

3.6.4 Velocity gradients with R, $|Z|$ and [Fe/H].

Similar to the metallicity gradient we also computed azimuthal velocity gradients with R and $|Z|$, which can be useful in comparison with dynamical heating models for formation of the thick disk (Villalobos et al. 2010).

The radial gradients are shown on the top panel of the Figure 3.15. The

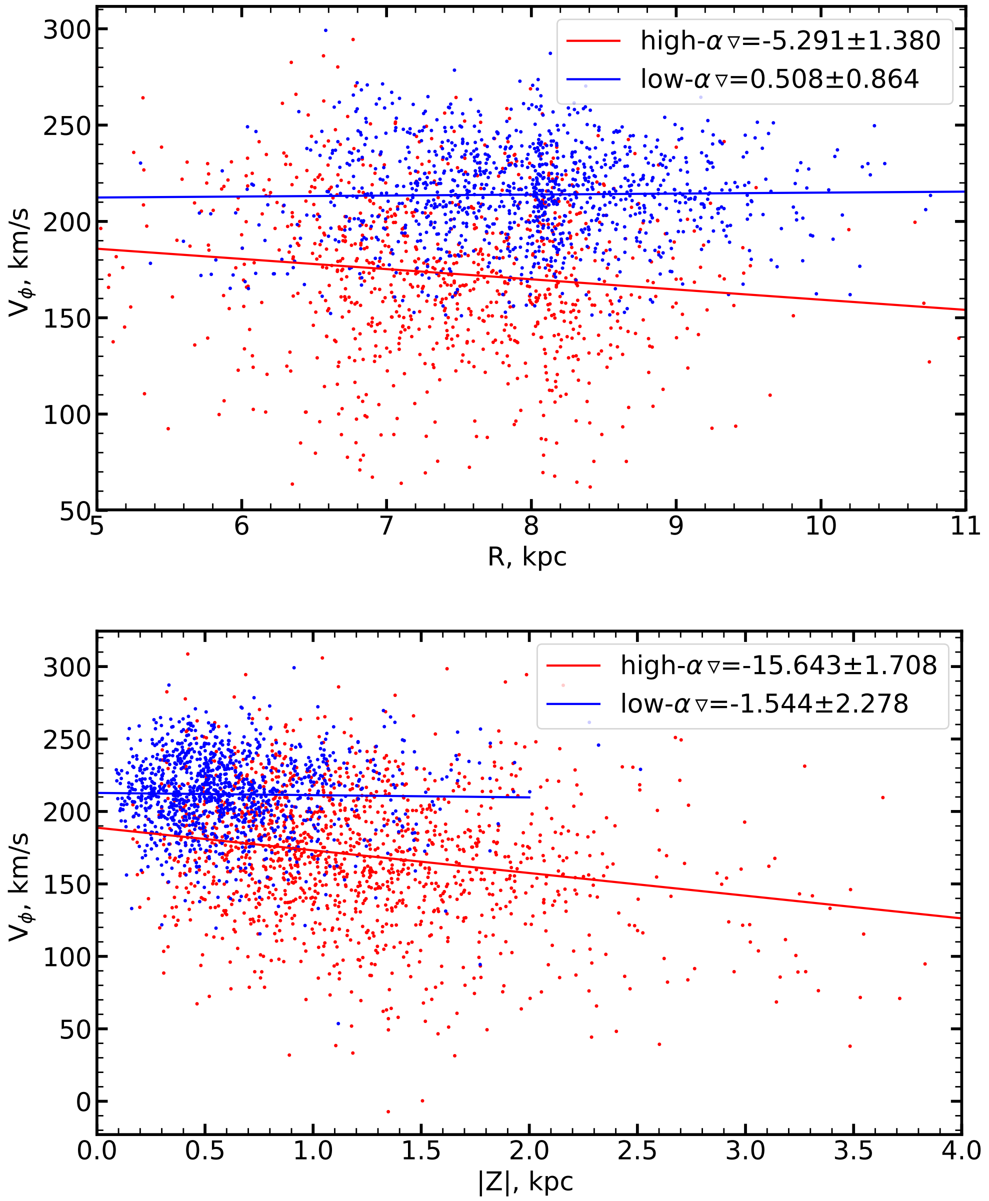

Figure 3.15: Radial (top panel) and vertical (bottom panel) gradients for azimuthal velocity.

high-[α/Fe] component has $dV_\phi/dR = -5.29 \pm 1.38$ km s^{-1} kpc^{-1} and low-[α/Fe] component has $dV_\phi/dR = -0.51 \pm 0.86$ km s^{-1} kpc^{-1}. The vertical gradients are shown on the bottom panel of Figure 3.15. The high-[α/Fe] component has $dV_\phi/d|Z| = -15.64 \pm 1.71$ km s^{-1} kpc^{-1} and the low-[α/Fe] component has $dV_\phi/d|Z| = -1.54 \pm 2.28$ km s^{-1} kpc^{-1}.

These results indicate different kinematic properties of the thin and thick disks. We find flat gradients for the thin disk and steep negative gradients for the thick disk. We will discuss these findings in comparison with dynamical heating and gas-rich merger thick disk formation scenarios in Section 3.7.2.

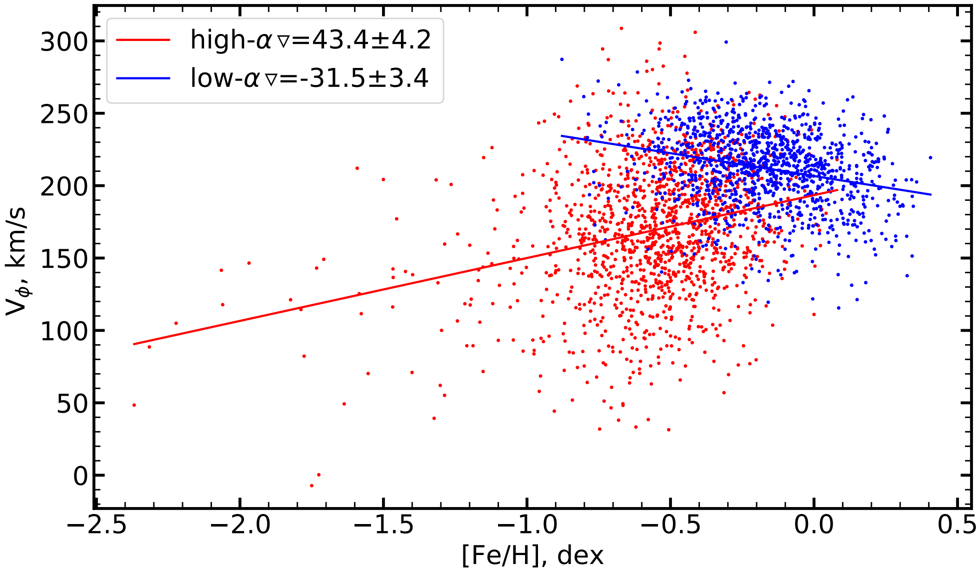

Figure 3.16: Azumuthal velocity gradients with metallicity.

We display the azimuthal velocity as a function of metallicity in Figure 3.16. The low-[α/Fe] component shows a negative gradient dV_ϕ/d[Fe/H] $= -31.5 \pm 3.4$ km s^{-1} dex^{-1}, however the high-[α/Fe] stars show a positive gradient dV_ϕ/d[Fe/H] $=$ 43.4 ± 4.2 km s^{-1} dex^{-1}. Such a negative slope of the azimuthal velocity with metallicity for the thin disk and a positive slope for the thick disk were derived in many other studies (Adibekyan et al. 2012; Recio-Blanco et al. 2014; Minchev et al. 2019; Yan et al. 2019), and we will discuss them in Section 3.7.2.

We collect all numeric values for derived gradients in Table 3.2.

Table 3.2:: Gradients for the thick and thin disk.

gradient	units	Thick disk	Thin disk
d[Fe/H]/dR	dex kpc^{-1}	-0.018±0.011	-0.063±0.010
d[Fe/H]/d$\|Z\|$	dex kpc^{-1}	-0.128±0.010	-0.145±0.018
d[Mg/Fe]/d$\|Z\|$	dex kpc^{-1}	0.023±0.002	0.017±0.004
dV$_\phi$/dR	km s^{-1} kpc^{-1}	-5.291±1.380	0.508±0.864
dV$_\phi$/d$\|Z\|$	km s^{-1} kpc^{-1}	-15.64±1.71	-1.54±2.28
dV$_\phi$/d[Fe/H]	km s^{-1} dex^{-1}	43.4±4.2	-31.5±3.4

3.6.5 Velocity and velocity dispersions with [α/Fe]

In this section we explore the observed velocity and its dispersions with [α/Fe] for the full disk sample, without separation on the high and low-[α/Fe] sub-samples. We split the data set into 6×7 2D bins in the [α/Fe]-[Fe/H] plane and compute the mean and dispersion values using a maximum likelihood estimate for all bins containing ≥ 10 stars, with velocity errors less than 10 km s^{-1}.

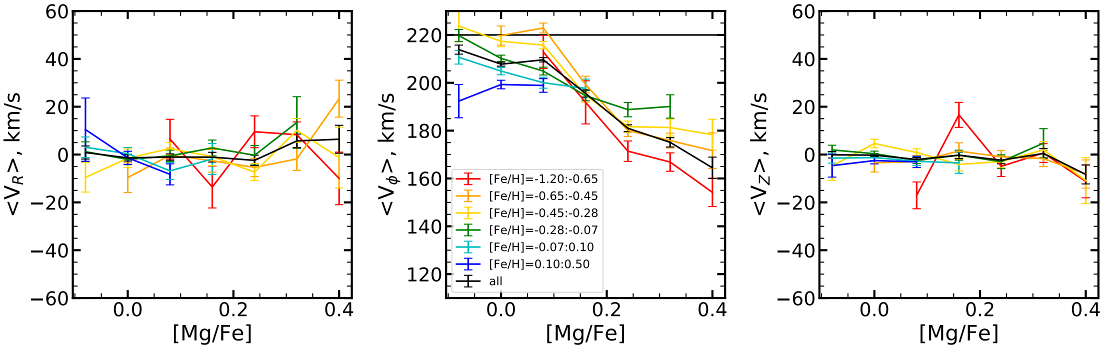

Figure 3.17: Mean velocities with [α/Fe] for different metallicity bins. The black lines indicate values that are computed for all bins.

In Figure 3.17 we present mean values for all three velocity components. The radial and vertical velocities are close to zero, with some metallicity bins showing noticeable deviations. In the azimuthal velocity plot, shown in the middle panel, metal-rich stars ([Fe/H] > -0.07 dex) move $\approx 20\,\mathrm{km\,s^{-1}}$ slower than local circular velocity, anti-correlated with the [Mg/Fe]. The stars with intermediate metallicities slow down from $V_\phi = 220$ km s^{-1} in the low-[α/Fe] regime to $V_\phi = 170$ km s^{-1} for the high-[α/Fe] part, with steeper gradients for more metal-poor bins. At the same time, all metallicity bins with [Fe/H] < -0.07 dex have the same mean azimuthal velocity $V_\phi = 200$ km s^{-1} at [Mg/Fe] $= 0.15$ dex. The metal-poor bins have velocity around

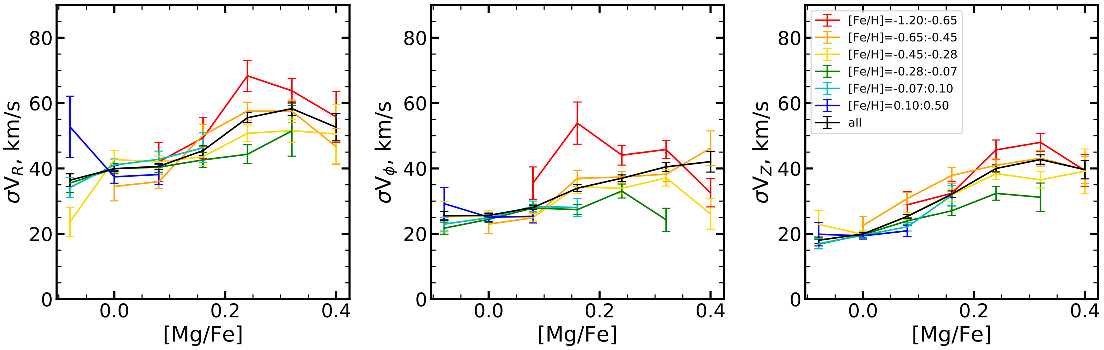

Figure 3.18: Velocity dispersions with [α/Fe] for different metallicity bins. The black lines indicate values that are computed for all bins.

$V_\phi = 170\ \mathrm{km\,s^{-1}}$ for the high-[α/Fe] part, which is consistent with our positive gradient dV_ϕ/d[Fe/H] for the thick disk. These results also qualitatively agree with previous studies by Recio-Blanco et al. (2014); Guiglion et al. (2015) and Hayden et al. (2017).

The velocity dispersions are shown in Figure 3.18, with trends for all metallicity bins presented as colour-coded lines. Dispersions are increasing for all velocity components, however the trend becomes flat for radial and vertical velocities in the high-[α/Fe] regime. If we consider some particular metallicity bins we observe an inversion of the trend for [Mg/Fe]-rich bins. This behaviour is in line with results from Minchev et al. (2014), where the turnoff in velocity dispersions is explained by an early merger event that has started radial migration of the inner disk stars with cool kinematics into the solar neighbourhood. The dispersion in radial velocity is usually large than the dispersion in the other velocity component, taken at the same [α/Fe]. For the [Mg/Fe] > 0.3 dex we have $\sigma V_z/\sigma V_R \sim 0.7$. Generally our results agree with previous works by Guiglion et al. (2015); Hayden et al. (2017).

3.7 Discussion

3.7.1 Comparison with stellar clusters

We compare chemical abundance results for field stars with the previous analysis of the stellar clusters from Chapter 2 in Figure 3.19. In this case all [Mg/Fe] and [Fe/H] values were derived using the same NLTE-*Payne* method, therefore analysis is completely homogeneous. We present maximum likelihood estimates of clusters mean abundance together with intra-cluster scatter, computed as one standard deviation. The only one thin disk open cluster NGC 3532 lie in the bottom of the low-[α/Fe] disk population. Another open cluster NGC 2243 is located exactly in the "gap" of the disk population and in Chapter 2 we assigned it to the thick disk based on high height relative to the galactic mid-plane ($|Z| \sim$ 1kpc). Two globular clusters with [Fe/H] > -1 dex lie in the upper part of the high-[α/Fe] disk population. The metal-poor globular clusters overlap with field halo and metal-poor disk populations.

Our results for the Milky Way disk and halo stars are in good agreement with other 1D NLTE magnesium abundances from Bergemann et al. (2017) and Mashonkina et al. (2019). The mean value for the metal-poor thick disk and halo stars is [Mg/Fe] $\sim$ 0.3 dex. The star-to-star scatter in [Mg/Fe] is around 0.1 dex. The sliding mean, computed using [Fe/H] bins of 0.25 dex width, is flat for the metal-weak thick disk, but the halo shows a notable (Δ[Mg/Fe] $\sim$ 0.15 dex) depletion around [Fe/H] $= -1.0$ dex, which is due to the presence of halo stars with [Mg/Fe] $\sim$ 0.0 dex. Ishigaki et al. (2012) found that outer halo population exhibits decline in [Mg/Fe] around [Fe/H] $= -1$ dex which agrees with our results. For the thick disk disk they also found flat trend of [Mg/Fe] with [Fe/H]. In Bergemann et al. (2017) <3D> NLTE results for the halo population show the descending trend, from high [Mg/Fe] for metal-poor stars to the solar-[Mg/Fe] around [Fe/H] ~ -1 dex, which was explained as a result of accretion from dwarf galaxies. Several low-[α/Fe] stars with thick disk kinematics were found in LAMOST DR3 by Xing & Zhao (2018), where their accretion origin was proposed. As we already discussed in Chapter 2 a location of the clusters next to the lower end of the field [Mg/Fe] distribution together with halo kinematics possibly indicates the *ex-situ* origin of such clusters. The broad eccentricity distribution for the halo population at high-e end and high r_{apo} distances (see Figure 3.18) also support the accretion origin for many halo stars.

The magnesium is mainly produced in the cores of massive stars during their explosions as a Type II supernovae (SN II). The iron is also produced in SN II explosions, although its main sources are the less-massive stars in binary systems which explode as a Type Ia supernovae (SN Ia) (Timmes et al. 1995). The SNe Ia explosion require one star to evolve to the white dwarf stage and therefore they start to contribute to the metal-enrichment of the interstellar media significantly later ($10^8 - 10^9$ years) than SNe II (Tolstoy et al. 2009). The moment when SNe Ia become the dominant source of the iron production can be seen in [Mg/Fe]-[Fe/H] diagram as a knee when [Mg/Fe] ratio starts to decrease. In Galactic chemical evolution model by Kobayashi et al. (2006) Mg show a plateau for metal-poor regime and have a knee at [Fe/H] ~ -1 dex, which agrees with our results. Tolstoy et al. (2009, and

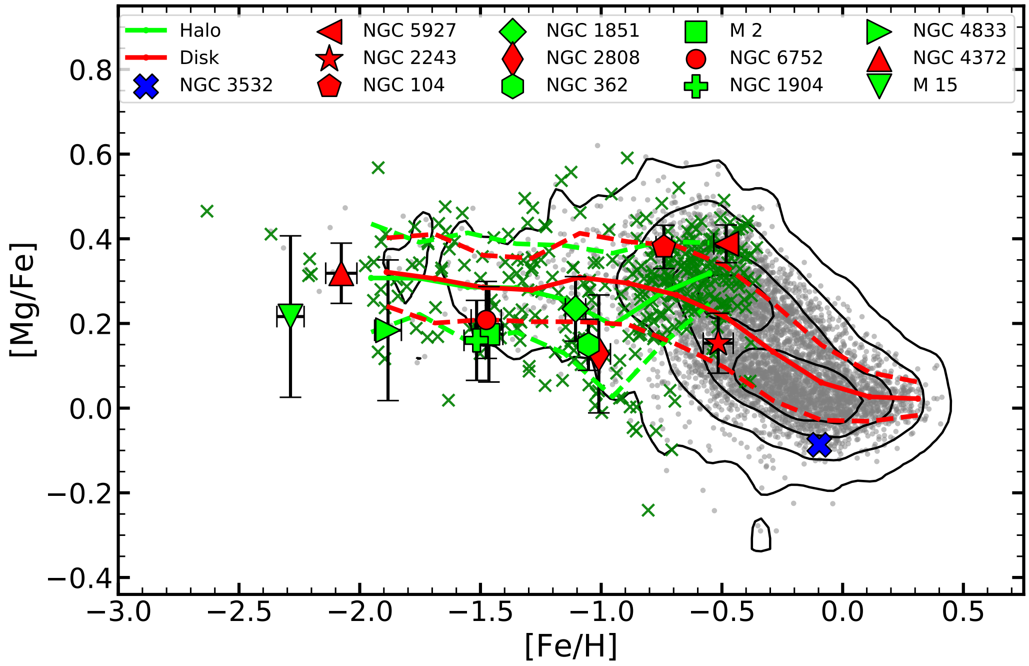

Figure 3.19: Comparison of field stars with NLTE results for open and globular clusters. The symbols are the same as in Figures 2.12 and 3.7. The disk stars are shown similarly to Figure 3.7 as a grey dots with contours showing 33%, 66%, 90% and 99% of the population. Sliding mean for the halo stars is shown as a thick lime line with 1σ interval around, with individual halo stars are shown as green crosses. The red sliding mean represents all disk stars including the thin and thick disk, but in [Fe/H] < -1 dex it shows only thick disk alone. Thin disk cluster is shown in blue, thick disk clusters are shown in red and halo clusters shown using lime colour.

references therein) shown that nearby dSph galaxies have solar or sub-solar [Mg/Fe] for metallicities [Fe/H] > -1.5 dex, therefore low-[α/Fe] halo stars were probably accreted from Milky Way satellites with different star formation history as it was proposed in Nissen & Schuster (2010, 2011).

3.7.2 Formation of the thick disk

In this section we discuss our results and their implication for formation and evolution of the Galactic disk. The problem of the origin of dual thick/thin disk structure in the Galaxy is still open. The published models or simulations can suffer from many assumptions and numeric effects that make them not complete realisation of the real Galaxy. Thus our measurements can be only qualitatively compared to model expectations. As it was outlined in previous sections our observational sample consists only of FG stars that is a quite special population, which can lack some hot or cool stars. We do not make forward modelling[4] of the Galactic disk evolution, therefore fair comparison of our sample to the model of the overall Galactic population is possible only if the sample is good representation for this population. In other words our sample should have same age distribution as a whole population. The high-[α/Fe] disk population have age of 9-11 Gyr (Haywood et al. 2013; Bensby et al. 2014; Buder et al. 2018a), therefore our high-[α/Fe] sample can be a fair representation of the thick disk, because this population consists of the old stars with small spread in age 1-3 Gyr (Kobayashi et al. 2006). For the low-[α/Fe], thin disk age distribution is significantly broader: from zero to 8-10 Gyr (Haywood et al. 2013; Bensby et al. 2014; Buder et al. 2018a) and our survey selection and quality cuts can introduce significant bias in the observed age and [Fe/H] distribution and change observed metallicity and kinematic gradients. For example our sample does not include young hot stars with $T_{\rm eff} > 6900$ K and main sequence dwarfs with $T_{\rm eff} < 5000$ K. Based on this we will discuss our results mostly for the thick disk population and not for the thin disk where our results are less reliable.

Sales et al. (2009) proposed using the eccentricity distribution of the thick disk stars to select a dominant formation scenario (See Figure 1.5). In their analysis stellar particles, representing the thick disk were selected in solar neighbourhood using cuts at height $1 < |Z/Z_0| < 2$ where Z_0 is a thick disk scale height of the modelled galaxy respectively. We apply a height cut using $Z_0 = 0.9\,\mathrm{kpc}$ from Jurić et al. (2008) and compare our observed high-[α/Fe] population e-distribution to the model predictions in Figure 3.20. The distribution for the accretion scenario is too wide and shifted to the high e values, in comparison to observed one. In the dynamical heating scenario the eccentricities show a bimodal distribution with a higher peak at $e \sim 0.2$ and a lower peak at $e \sim 0.8$, where the observed distribution have only one peak at low e. The radial migration scenario has a narrow distribution that is centred at $e \sim 0.2$ and has a sharp cut-off at high eccentricities at $e = 0.7$, which is not matching shape of the observed distribution, because it has less high-e stars and much more stars with $e < 0.3$. For the gas-rich merger scenario, the e distribution is centred at $e = 0.25$ and has a long tail down to $e = 0.9$, which is also in agreement with the observed distribution, however the high-e tail is less populated. Therefore, our results favours last the two scenarios: radial migration and gas-rich merger. However, the lack of the stars in the high-e accreted part can be due to the selection effects, because such stars are not numerous and usually located at high altitudes with respect to the galactic mid-plane. Also a different

---

[4] In this context it means that we do not convolve model with errors and do not apply quality cuts to model, before model-to-data comparison.

choice of the Galactic potential can lead to an offset (~ 5 %) in derived eccentricities and change the observed distribution (Mackereth & Bovy 2018).

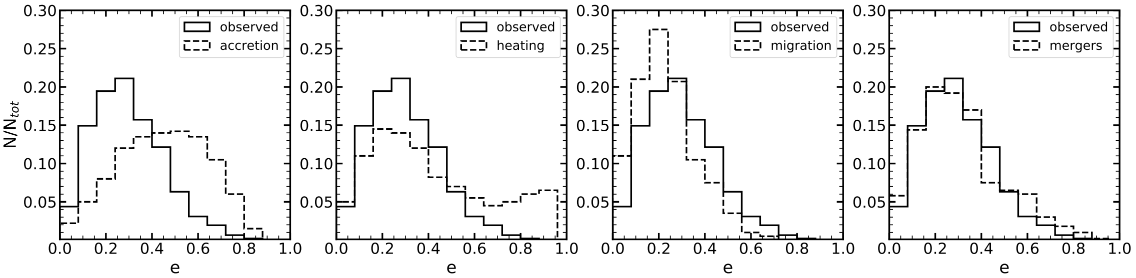

Figure 3.20: Comparison of the observed e-distribution to the model predictions from Figure 3 of Sales et al. (2009). We use the same bin sizes for our high-[α/Fe] sample as in comparison paper.

In the radial migration, stars with different birth radii can move to inner and outer regions of the disk. As stellar density in the central part of the Galaxy is higher and the interstellar gas there is more metal-rich, the average effect of migration will be seen as the presence of metal-rich stars in outer regions with more metal-poor interstellar medium. In other words, radial migration will make disk more homogeneous in metallicity with time. Our results indicate negative radial metallicity gradients for the thin disks and almost flat gradient for the thick disk. This may be explained by radial migration scenario that lead to the flattening of the radial metallicity gradient with time. Loebman et al. (2011) reported the thin disk gradient of $\mathrm{d[Fe/H]/d}R = -0.02$ dex kpc^{-1} based on N-body simulations of the Galaxy (see their Figure 12), which is qualitatively in agreement with our value of $\mathrm{d[Fe/H]/d}R = -0.063 \pm 0.010$ dex kpc^{-1}. For the thick disk they report a flat gradient $\mathrm{d[Fe/H]/d}R = 0.00$ dex kpc^{-1}, which is consistent with our estimate $\mathrm{d[Fe/H]/d}R = -0.018 \pm 0.011$ dex kpc^{-1}. For the azimuthal velocity gradient with metallicity Loebman et al. (2011) suggested that the gradient will diminish and fade with time. They provided three values $\mathrm{dV}_{\phi}/\mathrm{d[Fe/H]} = -29, -19, 8$ km s^{-1} dex^{-1} for young, intermediate and old stars respectively (see their Figure 9). Minchev et al. (2014); Bergemann et al. (2014) showed that [α/Fe] can be a good indicator for stellar age in a narrow range of galactocentric radii. Taking this into account, predictions of Loebman et al. (2011) are in good agreement with our observed results for the thin disk stars with low-[α/Fe], which are considered to be young: $\mathrm{dV}_{\phi}/\mathrm{d[Fe/H]} = -31.5 \pm 3.4$ km s^{-1} dex^{-1}. For high-[α/Fe] stars we measure $\mathrm{dV}_{\phi}/\mathrm{d[Fe/H]} = 43.4 \pm 4.2$ km s^{-1} dex^{-1}, which is much steeper than prediction by Loebman et al. (2011). We do not measure such gradients in chemical intermediate [Mg/Fe] stars, because this bin may contain a large fraction of high- and low-[α/Fe] stars, due to abundance uncertainties. Schoenrich & McMillan (2017) explained such behaviour of a metallicity-velocity relation in the context of the inside-out formation of the disk. The young thin disk stars are formed from the material with a negative radial metallicity gradient, therefore metal-rich stars have lower velocities than metal-poor thin disk stars and we can observe them in the solar neighbourhood due to radial migration. The old metal-poor stars in the thick disk have a low azimuthal velocity, because they were formed in inner disk regions with slower rotation, so the metal-poor thick disk has $\mathrm{d}V_\phi/\mathrm{d}[\mathrm{Fe/H}] > 0$. However, if radial metallicity gradient was negative in the star-forming thick disk, velocity metallicity relation will change slope, since the knee in $[\mathrm{Fe/H}] - [\alpha/\mathrm{Fe}]$ plane locates at lower [Fe/H] for outer disk region. Schoenrich & McMillan (2017) suggest that the position of the turn-off in $\mathrm{d}V_\phi/\mathrm{d}[\mathrm{Fe/H}]$ for high-$[\alpha/\mathrm{Fe}]$ population can provide us constraints on the initial metal enrichment and SN Ia enrichment in the thick disk.

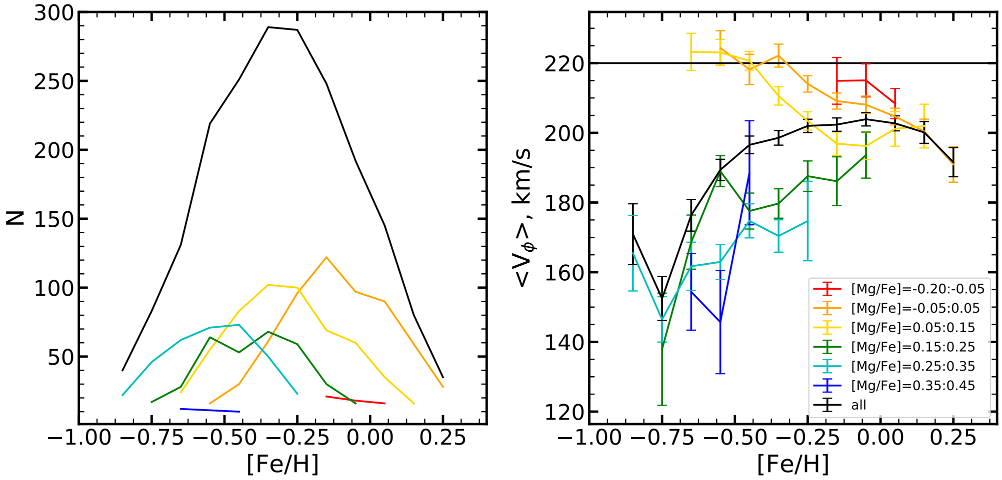

Figure 3.21: Distributions of the stars in [Mg/Fe] bins with metallicity (left panel) and average azimuthal velocity with [Fe/H] for different [Mg/Fe] bins (right panel). The black lines indicate values that are computed for all bins. Only bins with ≥ 10 stars are shown.

In Minchev et al. (2019) the positive $\mathrm{d}V_\phi/\mathrm{d}[\mathrm{Fe/H}]$ gradient in the RAVE results was explained as a result of a combination of the negative $\mathrm{d}V_\phi/\mathrm{d}[\mathrm{Fe/H}]$ of mono-age populations with large abundance uncertainties (See their Figure 5). We also explore such a possibility for a sub-sample of 2047 GES stars in a narrow cylinder with galactocentric radii $7.5 < R < 8.5$ kpc, taking [Mg/Fe] abundance ratio as a proxy for age. We apply a similar analysis to one in Section 3.6.5 and show the result in Figure 3.21. Note the negative gradient for the metal-poor end of the populations with $0.25 < [\mathrm{Mg/Fe}] < 0.35$ dex. This turn-off happens only in the part where such a population was dominating at the $-0.9 < [\mathrm{Fe/H}] < -0.8$ dex regime. For the other metallicity regimes different [Mg/Fe] population distributions overlap significantly and the cross-contamination due to abundance uncertainties can lead to an inversion of the $dV_\phi/d[Fe/H]$. Therefore, our results qualitatively agree with the Minchev et al. (2019) explanation.

The dispersions for different velocity components increase with [Mg/Fe] and become flat for [Mg/Fe] > 0.3 dex. Similar trends were observed by Minchev et al. (2014) in RAVE fourth data release, however their sample includes much more stars with [Mg/Fe] > 0.4 dex, where our sample is underpopulated. In the high-[Mg/Fe] part Minchev et al. (2014) found turnoffs in the velocity dispersions, which were explained by radial migration of the inner disk stars with cool kinematics into the solar neighbourhood. This radial migration was ignited by a merger event in the early stage (~ 9 Gyr ago) of Galactic evolution. Our results of the velocity dispersions with [Mg/Fe] qualitatively agree with previous studies by Guiglion et al. (2015) and Hayden et al. (2017), despite the fact that we use NLTE spectroscopic analysis and more precise astrometric data. Therefore, it is worthwhile to compare our findings with the study that uses the same astrometric information from Gaia DR2. Hayden et al. (2019) has combined GALAH chemistry with Gaia DR2 data and explored chemo-kinematic relations for $\sim 60\,000$ stars in the solar neighbourhood. With such a large dataset they obtain very clean and smooth relations for the mean azimuthal velocity and dispersions. Similar to our results, based on much smaller sample (~ 4000 stars), they show increasing dispersions with increasing [Mg/Fe].

The homogeneity of the thick disk is indeed a sign of efficient migration processes in the past, however this is not only one explanation. If the thick disk was formed from a well-mixed material in short timescale, gas-rich merger scenario can explain the observed gradients as well. Haywood et al. (2013) explored ages and kinematics of the local stars from Adibekyan et al. (2012) and found that radial migration cannot be a main contributor to the thick disk formation. According to the observations disk asymmetries have appeared in large spiral galaxies only during last 8 Gyr (Sheth et al. 2008), therefore radial migration was efficient in this time. This should be seen as a presence of numerous, young (< 8 Gyr) stars with significant vertical velocities W and maximal height Z_{max} in the solar neighbourhood. However, Haywood et al. (2013) found no such stars.

In the gas-rich merger scenario by Brook et al. (2007) the kinetically hot thick disk forms during the quick starburst following the merger, accompanied by large number of SNe II explosions. Then star formation drops and the thin disk forms from the gas which was already polluted by SNe Ia. In these simulations the azimuthal velocity shows a steep negative radial gradient for thin disk stars and a slightly negative gradient for thick disk stars at $R \sim 8$ kpc. The [α/Fe] show no correlation with R and $|Z|$ for thin disk. The thick disk has slightly positive trends of the $[\alpha/\mathrm{Fe}]$ with R and $|Z|$. Our observations show a flat $\mathrm{dV}_\phi/\mathrm{dR} = 0.5 \pm 0.9\,\mathrm{km\,s^{-1}}$ kpc^{-1} and a slightly positive correlation for $[\alpha/\mathrm{Fe}]$ with $|Z|$ the low-$[\alpha/\mathrm{Fe}]$ stars. High-$[\alpha/\mathrm{Fe}]$ stars also show a non-zero correlation of $[\alpha/\mathrm{Fe}]$ with vertical distance and a small radial velocity gradient $\mathrm{dV}_\phi/\mathrm{dR} = -5.3 \pm 1.4\,\mathrm{km\,s^{-1}}$ kpc^{-1}. Therefore, the gas-rich merger model from Brook et al. (2007) may explain our measurements for the thick disk.

In Villalobos et al. (2010) the thick disk originated from the dynamical heating of the primordial disk by an infalling satellite. Their N-body simulations predict that azimuthal velocity gradients with R and $|Z|$ in thick dick contain information about orbital inclination of an infalling satellite relative to Galactic mid-plane. The orbits with high inclination angles produce strong $\mathrm{dV}_\phi/\mathrm{dR}$ and weak $\mathrm{dV}_\phi/\mathrm{d|Z|}$ gradients, but for low inclinations the slopes show the opposite behaviour (see their Figure 14). Additional information can be extracted from the ratio $\sigma\mathrm{V_z}/\sigma\mathrm{V_R}$ that increases with inclination angle (see their Figure 15). Our measurement of a steep vertical gradient for the thick disk favours a model with low inclination for the orbit of the infalling satellite, however the steep gradient $\mathrm{dV}_\phi/\mathrm{d|Z|} = -13.3 \pm 2.5\,\mathrm{km\,s^{-1}}$ kpc^{-1} and high dispersion ratio for the high-[Mg/Fe] regime $\sigma V_z/\sigma V_R \sim 0.7$ prefers moderately to highly inclined orbits. Therefore, the dynamic heating model scenario have difficulties to explain the observed properties of the thick disk.

In brief summary for this section, our observational results indicate that gas-rich merger scenario may have played a major role in the thick disk formation, although the influence of other formation processes like radial migration could also be important. The dynamical heating scenario and direct accretion are neglected mostly due to absence of high-e accreted stars in eccentricity distribution.

3.8 Summary and conclusions

We analysed stars in the Milky Way disk and halo, for which spectra from the public data release of Gaia-ESO survey are available. We employed NLTE spectral models and *the Payne* code to derive spectral parameters and chemical abundances from these spectra. All stars in our sample have reliable astrometric information from Gaia DR2, which allowed us to explore their velocities and orbits. We applied different methods to assign Galactic populations for the stars in our sample and found that purely kinematic selection can lead to a significant mixture of the high-$[\alpha/\mathrm{Fe}]$ and low-$[\alpha/\mathrm{Fe}]$ populations. Therefore, we applied a simple chemical separation based on the less-populated "gap" in the $[\alpha/\mathrm{Fe}]$-$[\mathrm{Fe/H}]$ plane, similar to

Adibekyan et al. (2012); Recio-Blanco et al. (2014); Mikolaitis et al. (2014). We selected 1284 stars as a high-[α/Fe], 1498 stars as a low-[α/Fe] disk and 206 halo stars and analysed their chemical and kinematic properties.

We summarise our results and conclusions as follows:

- metal-poor thick disk population and halo have mean [Mg/Fe] $\sim$ 0.3 dex in a good agreement with previous NLTE studies. In the metal-poor regime these two populations are chemically indistinguishable. The metal-poor disk stars are detected down to [Fe/H] $= -2.2$ dex. The flat behaviour of the [Mg/Fe] in metal-poor regime indicates that Mg was mostly produced in SNe II, with negligible contribution from SNe Ia. The star-to-star scatter is relatively small $\lesssim$ 0.1 dex, which indicates that interstellar medium was well-mixed in the early Galaxy.

- several halo stars have solar-[Mg/Fe] ratio at [Fe/H] ~ -1 dex. Such stars may have been accreted from the dwarf satellite galaxies with different star formation history. The orbital properties also support accretion origin for many halo stars.

- the eccentricity distribution for high-[α/Fe] population rules out violent formation scenarios, like accretion and disk heating, due to lack of a high-e accreted part. The quiescent *in-situ* thick disk origin scenarios are more likely, like formation after a gas-rich merger or radial migration mechanism.

- The thin disk shows a negative radial metallicity gradient, but for the thick disk such a gradient appears to be flat. We find negative vertical metallicity gradients for both disk populations. The azimuthal velocity gradient with metallicity is negative for the young thin disk population and positive for the older thick disk population. These measurements support the inside-out disk formation.

- the velocity dispersions are increasing with [Mg/Fe] suggesting that the disk become kinetically hotter with time. However, dispersions decrease at high-[Mg/Fe] ends for the radial and vertical velocity. It can indicate that radial migration cools the disc during mergers (Minchev et al. 2014).

- our measurements of the vertical [α/Fe] and dV_ϕ/dR gradients for the high-[α/Fe] disk can be explained by gas-rich merger scenario model by Brook et al. (2007).

- $dV_\phi/d|Z|$ gradient and velocity dispersion ratio favour quite different orbital inclinations for an infalling satellite, therefore we discount dynamic heating scenario for the thick disk formation.

Our observed properties for disk stars qualitatively agree with previous works which have analysed earlier Gaia-ESO data releases. The new NLTE spectroscopic analysis with accurate astrometric information from Gaia DR2, allows us to find out that a combination of the gas-rich merger event with radial migration may play a dominant role in the formation of the Galactic thick disk. Soon the final Gaia-ESO data release will bring much better statistics and coverage and will allow a much more complete description of the structure and evolution of the Galactic components.

Chapter 4

NLTE online-service

In this chapter I will describe the online service http://nlte.mpia.de/ which I have developed in order to make results of the NLTE calculations more accessible to the members of the astronomy community.

4.1 Introduction

The stellar chemical abundance are usually computed with LTE spectral analysis methods and the derived abundance values can be biased due to LTE assumptions. Most common way to deal with this problem is to use NLTE abundance correction:

$$\Delta_{\mathrm{NLTE-LTE}} = \log A(\mathrm{X})_{\mathrm{NLTE}} - \log A(\mathrm{X})_{\mathrm{LTE}}, \tag{4.1}$$

the change in LTE abundance of the element X, which compensate the difference between NLTE and LTE analysis. Such corrections are usually provided for large grids of stellar parameters on line-by-line basis. For example, INSPECT database of NLTE corrections at http://inspect-stars.com/. However, not all spectral lines and spectral parameter combinations are covered by this service. There are several studies of the NLTE effects in many chemical elements like Mn (Bergemann, M. & Gehren, T. 2008), H (Mashonkina et al. 2008), Co (Bergemann et al. 2010), Cr (Bergemann & Cescutti 2010), Si (Bergemann et al. 2013), O (Sitnova et al. 2013), Ti (Bergemann 2011), Mg (Bergemann et al. 2017) and Fe (Bergemann et al. 2012), which share common methodology and use the same codes. In these studies usually only a relatively small number (typically < 50) of the most important spectral lines is discussed, although statistical equilibrium calculations were done for atomic models that include many more transitions. Therefore, to fully explore the potential of the previous NLTE studies one can extend results to all lines that have available statistical equilibrium calculations and make these results available. The most convenient and flexible way to publish such results is to provide an online interface where anyone can check if NLTE effects are strong for specific lines or computed NLTE synthetic spectra.

4.2 Methods

In this work we use the same methods and codes as in previously mentioned NLTE studies. Here we just provide a brief description. We use the well-tested code DETAIL (Butler & Giddings 1985) to compute atomic level populations $N_{\rm NLTE}$ by solving statistical equilibrium equations. The spectral line profile is computed by the spectrum synthesis code SIU (Reetz 1991), which uses departure coefficients $b_i = N_{\rm NLTE}/N_{\rm LTE}$ from DETAIL for both upper and lower energy levels of the given NLTE transition. Both DETAIL and SIU are using the two grids of stellar atmospheres MAFAGS-OS (Grupp 2004a,b) and MARCS (with red super giant subgrid RSG-MARCS) (Gustafsson et al. 2008). The atomic models are adopted from the original NLTE studies together with Drawins cross-sections scaling factors $S_{\rm H}$ for rates due to inelastic collisions with neutral hydrogen atoms[1]. We list scaling factors used in calculations in Table 4.1.

Table 4.1:: Scaling factors $S_{\rm H}$

grid	H	O	Mg	Si	Ti	Cr	Mn	Fe	Co
MAFAGS-OS	1	1	0	1	0.5	0	0.05	0.5	0.05
MARCS	1	1	0	1	0.05	0	0.05	1	0.05
RSG-MARCS	...	...	0	1	1	...	...	1	...
Model atom	LM08	TS13	MB17	MB13	MB11	MB10b	MB08	MB12	MB10a

References: LM08 - Mashonkina et al. (2008), TS13 - Sitnova et al. (2013), MB17 - Bergemann et al. (2017), MB13 - Bergemann et al. (2013), MB11 - Bergemann (2011), MB10b - Bergemann & Cescutti (2010), MB08 - Bergemann, M. & Gehren, T. (2008), MB12 - Bergemann et al. (2012), MB10a - Bergemann et al. (2010)

Ones the grids of departure coefficients are computed we can find all the spectral lines with available NLTE information by cross-matching the spectral line list with the energy levels provided in the atomic models. This is non-trivial in some cases due

---

[1] The rates of transitions due to inelastic collisions with neutral hydrogen atoms are calculated according to Drawins formula (Drawin 1968, 1969) in the version of Steenbock & Holweger (1984).

to incomplete information for certain lines in the line list and different designations for the same energy levels in atomic model and line list. In such complicated cases we use additional information from Kurucz[2] and NIST[3] databases. The resulting set of spectral lines is provided to the SIU spectrum synthesis code. At the moment such cross-match procedure is done for the main ($2010 < \lambda < 13000$ Å) and infrared (IR $13000 < \lambda < 24600$ Å) line lists. The total number of lines with available NLTE information is given in Table 4.2.

Table 4.2:: Number of available NLTE lines for each element.

line list	O	Mg	Si	Ti	Cr	Mn	Fe	Co
Main	27	41	120	4992	2160	3037	6626	7447
IR	188	208	375	1192	373	541	2102	477

4.3 Functionality

Our online service provides NLTE results for cool stars. As a preparation step we interpolate the stellar atmospheric structure and the departure coefficients for a given combination of spectral parameters ($T_{\rm eff}$, log(g) , [Fe/H]) using linear interpolation. The possible ranges of input parameters for each atmospheric grid are listed in Table 4.3.

Table 4.3:: Coverage of atmospheric model grids.

grid	$T_{\rm eff}$, K	log(g), cm s^{-2}	[Fe/H], dex	comment
MAFAGS-OS	4600:8800	1.0:5.0	-4.8:0.9	plane-parallel
MARCS	2500:7750	-0.5:3.5	-5.0:1.0	spherical-symmetric, mass=1 $M_\odot$
RSG-MARCS	3400:4400	-1.0:1.0	-1.5:1.0	spherical-symmetric, mass=15 $M_\odot$

Unlike INSPECT, our web-service computes NLTE abundance corrections on the fly. We run spectral synthesis for a given spectral line in NLTE at ± 5 Å interval and compute its equivalent width. If the line is stronger than 1 mÅ we compute 21 LTE spectral profiles, with varying abundance between -1 and 1 dex relative to the value in the atmospheric model. After that we compute the equivalent widths for all LTE profiles and we use them to interpolate the LTE abundance variation that

---

[2] https://www.cfa.harward.edu/amp/ampdata/kurucz23/sekur.html

[3] https://physics.nist.gov/PhysRefData/

will match best the equivalent width of the NLTE profile. The NLTE abundance correction $\Delta_{\mathrm{NLTE-LTE}}$ is equal to this interpolated LTE abundance variation taken with minus sign. For NLTE lines weaker than 1 mÅ no correction is provided. The online interface allows the user to compute a table with the corrections for several lines of different chemical elements in a given list of stellar parameters. For convenience we provide interactive selection boxes for each element which allows us to select available NLTE spectral lines. If necessary, figures with spectral profiles can be provided for visual inspection.

A different part of the online interface allows us to compute synthetic LTE/NLTE spectrum and compare it with the observed one using an interactive plot. The observed spectrum can be uploaded by the user as a standard ASCII file with the wavelength in Å and a normalised spectral flux. The several chemical elements can be modelled in NLTE simultaneously, using all available NLTE lines. The synthetic spectrum can be convoluted with a Gaussian profile or a rotational profile in order to reproduce resolution and line broadening of the observed spectrum. The part of the line list used in the calculations is included in the output as an interactive selection box that also allows the user to identify particular spectral lines. The best use of this interface is to visually fit stellar parameters in a narrow spectral window ($<$ 300 Å) or to explore the strength of NLTE effects for a given set of stellar parameters.

With slight modification of the previous interface we can allow for a batch computations of NLTE spectral models for a given list of stellar parameters and chemical abundances. Unlike spectrum synthesis, this interface does not provide an interactive plot and therefore can be used for much larger spectral intervals, limited only by the size of the line list. The best use of this interface is the computation of spectral model grids, which can be used in other applications, for example to train *the Payne* spectral model (see Chapter 2).

4.4 Summary and future plans

The NLTE online-service is publicly available at the internet address `http://nlte.mpia.de/` since March 2017 and is consequently updated. It allows the computation of the spectral models and NLTE abundance corrections for a wide range of stellar parameters for nine chemical elements. This service is intensively used by astronomers from all around the world and we got very positive feedback from them.

We plan to implement several updates:

- add NLTE results for singly ionised Ti, Cr and Co,
- add NLTE results for several new elements like Ca, Ba and Ni,
- recompute and update results for Mn using new atomic model from Bergemann et al. (2019),
- add NLTE results for all elements for RSG-MARCS grid,
- include NLTE results for plane-parallel MARCS atmospheric models.

We acknowledge help and support from IT-department of the Max Planck Institute for Astronomy that provided the infrastructure and hosted this service. This service was developed using *PHP* and *Gnuplot*.

Chapter 5

Summary

In the first part of this work we developed the spectral analysis pipeline that combines the NLTE synthetic spectra with *the Payne* - the forward spectral model, based on neural-networks (Ting et al. 2018). We computed two grids of synthetic spectra of FGK stars, one grid with all elements treated in LTE and a second grid with transitions of the iron, magnesium, titanium and manganese modelled in NLTE. This allowed us to study the NLTE effects on the determination of the stellar parameters and chemical abundances.

This pipeline is applied to medium-resolution spectra from the third public data release of Gaia-ESO spectroscopic survey (Gilmore et al. 2012), where we select a sample of Gaia benchmark stars and members of the galactic open and globular clusters. These stars allow us to verify the performance of our method on a wide range of stellar parameters. We find out that our approach accurately recovers the effective temperatures, surface gravities and chemical abundances of the benchmark stars and the clusters members. However, the abundances of Mn can be recovered only for the metal-rich regime [Fe/H] > -1 dex. The differences between NLTE and LTE are significant in the metal-poor regime, [Fe/H] $\lesssim -1$. The NLTE [Fe/H] values are systematically higher, whereas the average NLTE [Mg/Fe] abundance ratios are ~ 0.15 dex lower, compared to LTE.

Our LTE measurements of metallicities and abundances of stars in Galactic clusters are in a good agreement with the literature values. Contrary to common assumptions, the NLTE analysis changes the mean abundance ratios in the clusters, but it does not influence the intra-cluster abundance dispersions. All clusters are homogeneous in Fe and Ti, with intra-cluster abundance variations of less than 0.04 dex. Several globular clusters (NGC 2808, NGC 4833, M2, and M 15) showed significant dispersion in [Mg/Fe], which is commonly attributed to the scenario of globular clusters that have undergone multiple episodes of star formation and self-enrichment (Bastian & Lardo 2018). NLTE analysis suggests that the majority of metal-poor clusters with [Fe/H] < -1 dex and halo-like kinematics, show a prominent, ~ 0.15 dex, depletion of [Mg/Fe] compared to field stars of the same metallicity. This may indicate their *ex-situ* formation history, with these clusters being accreted from disrupted satellite galaxies.

In the second part, we use our NLTE method to study the chemo-dynamical evolution of the Milky Way. We compute [Fe/H] and [Mg/Fe] abundances for a big sample of Galactic field stars from the third public data release of Gaia-ESO spectroscopic survey (Gilmore et al. 2012). We use Gaia DR2 (Gaia Collaboration et al. 2018) astrometric data to derive positions, 3D velocities and orbits for each star. We apply chemical separation to select high-[α/Fe] and low-[α/Fe] disk populations, with halo stars are selected using kinematics.

The mean [Mg/Fe] abundance ratios for the field stars confirm model predictions that SNe II were the main contributors to the metal-enrichment of the early Galaxy as indicated by super-solar Mg abundance in the metal-poor regime. The SNe Ia enrichment becomes active later and decreases [Mg/Fe] to the solar abundances in the metal-rich regime. Our NLTE results show a constant [Mg/Fe] ~ 0.3 dex for both metal-poor disk and halo with relatively small star-to-star scatter $\lesssim 0.1$ dex. This indicates that interstellar medium was well-mixed in the early Galaxy. A notable fraction of the halo stars with [Fe/H] ~ -1 dex and with solar [Mg/Fe] may be accreted from the disrupted satellites of the Milky Way with different chemical enrichment history, which is also supported by their dynamical properties.

The observed eccentricity distribution for high-[α/Fe] disk population rules out a violent thick disk formation mechanisms like direct accretion and dynamic heating due to the lack of high-e accreted part. The observed chemical and kinematic gradients together with velocity dispersions for the high-[α/Fe] population can be explained by the gas-rich merger scenario with the non-negligible contribution from the radial migration.

In the last Chapter 4, we present the NLTE online service, which provides NLTE spectral data for nine chemical elements in cool stars. It allows astronomers to calculate NLTE corrections for LTE abundances, visually fit observed spectra and compute grids of synthetic spectra.

5.1 Perspectives

This results of this work have many future applications. First and most direct, is to use our results as constraints on Galactic chemical evolution and nucleosynthesis models. Secondly, our NLTE-*Payne* method can be applied to the final data release of Gaia-ESO spectra, which should be published soon. Additionally in order to fully explore information content in observed spectra, the spectral models can be upgraded in order to fit more chemical elements in NLTE. The results for new data release together with Gaia DR2 data will allow us to estimate the stellar ages which are very useful in the Galactic population assignment as it was indicated in Bensby et al. (2014); Buder et al. (2018a). The combination of temporal (ages), chemical (abundances) and kinematic (velocities) data will definitely improve our understanding of the Galactic structure and evolution.

List of publications

First author:

Kovalev, M., Bergemann, M., Ting, Y.-S. and Rix, H.-W., 2019, A&A, 628, A54, used in this thesis.

Co-authored:

Emelyanov, N. V. and Kovalyov, M. Yu., 2013, MNRAS, 429, 3477E

Emelyanov, N. V., Kovalyov, M. Yu., Chernin, A. D., 2015, Astronomy Reports, 59, 510

Bergemann, M., Serenelli, A., Schönrich, R., Ruchti, G., Korn, A., et al. 2016, A&A, 594, A120

Bergemann, M., Collet, R., Amarsi, A. M., Kovalev, M., Ruchti, G., et al. 2017, ApJ, 847, 15

Bergemann, M., Collet, R., Schönrich, R., Andrae R., Kovalev, M., et al. 2017, ApJ, 847, 16, used in this thesis

Kirby, E. N., Xie, J. L., Guo, R., Kovalev, M., Bergemann, M. 2018, The Astrophysical Journal Supplement Series, 237, 18

References

Abadi, M. G., Navarro, J. F., Steinmetz, M., & Eke, V. R. 2003, ApJ, 597, 21

Adibekyan, V. Z., Sousa, S. G., Santos, N. C., et al. 2012, A&A, 545, A32

Amarsi, A. M., Barklem, P. S., Asplund, M., Collet, R., & Zatsarinny, O. 2018, A&A, 616, A89

Amarsi, A. M., Lind, K., Asplund, M., Barklem, P. S., & Collet, R. 2016, MNRAS, 463, 1518

Anderson, J., Piotto, G., King, I. R., Bedin, L. R., & Guhathakurta, P. 2009, ApJ, 697, L58

Andrae, R., Fouesneau, M., Creevey, O., et al. 2018, A&A, 616, A8

Anthony-Twarog, B. J., Atwell, J., & Twarog, B. A. 2005, AJ, 129, 872

Arnason, R. M., Sivakoff, G. R., Heinke, C. O., Cohn, H. N., & Lugger, P. M. 2015, ApJ, 807, 52

Auer, L. H., & Mihalas, D. 1969, ApJ, 156, 157

Bailer-Jones, C. A. L. 2000, A&A, 357, 197

Bailer-Jones, C. A. L., Irwin, M., Gilmore, G., & von Hippel, T. 1997, MNRAS, 292, 157

Bailer-Jones, C. A. L., Rybizki, J., Fouesneau, M., Mantelet, G., & Andrae, R. 2018, AJ, 156, 58

Barklem, P. S. 2016, A&A Rev., 24, 9

—. 2018, A&A, 612, A90

Barklem, P. S., Osorio, Y., Fursa, D. V., et al. 2017, A&A, 606, A11

Bastian, N., & Lardo, C. 2018, ARA&A, 56, 83

Baumgardt, H., & Hilker, M. 2018, MNRAS, 1804.08359v2

Bautista, M. A., Lind, K., & Bergemann, M. 2017, A&A, 606, A127

Bekki, K., & Yong, D. 2012, MNRAS, 419, 2063

Bellazzini, M., Pecci, F. F., Ferraro, F. R., et al. 2001, AJ, 122, 2569

Bellini, A., Bianchini, P., Varri, A. L., et al. 2017, ApJ, 844, 167

Belokurov, V., Erkal, D., Evans, N. W., Koposov, S. E., & Deason, A. J. 2018, MNRAS, 478, 611

Belyaev, A. K., & Yakovleva, S. A. 2017, A&A, 606, A147

Bensby, T., Alves-Brito, A., Oey, M. S., Yong, D., & Meléndez, J. 2011, ApJ, 735, L46

Bensby, T., Feltzing, S., & Oey, M. S. 2014, A&A, 562, A71

Bergemann, M. 2011, MNRAS, 413, 2184

Bergemann, M., & Cescutti, G. 2010, A&A, 522, A9

Bergemann, M., Collet, R., Amarsi, A. M., et al. 2017, ApJ, 847, 15

Bergemann, M., Collet, R., Schönrich, R., et al. 2017, ApJ, 847, 16

Bergemann, M., Kudritzki, R.-P., Plez, B., et al. 2012, ApJ, 751, 156

Bergemann, M., Kudritzki, R.-P., Würl, M., et al. 2013, ApJ, 764, 115

Bergemann, M., & Nordlander, T. 2014, NLTE Radiative Transfer in Cool Stars, 169–185

Bergemann, M., Pickering, J. C., & Gehren, T. 2010, MNRAS, 401, 1334

Bergemann, M., Ruchti, G. R., Serenelli, A., et al. 2014, A&A, 565, A89

Bergemann, M., Gallagher, A. J., Eitner, P., et al. 2019, arXiv e-prints, arXiv:1905.05200

Bergemann, M., & Gehren, T. 2008, A&A, 492, 823

Bertelli Motta, C., Pasquali, A., Richer, J., et al. 2018, MNRAS, 478, 425

Bianchini, P., van der Marel, R. P., del Pino, A., et al. 2018, MNRAS, 481, 2125

Binney, J., & Merrifield, M. 1998, Galactic Astronomy

Blanco-Cuaresma, S., Soubiran, C., Jofré, P., & Heiter, U. 2014, A&A, 566, A98

Bland-Hawthorn, J., & Gerhard, O. 2016, ARA&A, 54, 529

Böhm-Vitense, E. 1958, Zeitschrift fur Astrophysik, 46, 108

Bonatto, C., Chies-Santos, A. L., Coelho, P. R. T., et al. 2019, A&A, 622, A179

Bovy, J. 2015, ApJS, 216, 29

Bovy, J., Rix, H.-W., & Hogg, D. W. 2012, ApJ, 751, 131

Brogaard, K., VandenBerg, D. A., Bedin, L. R., et al. 2017, MNRAS, 468, 645

Brook, C., Richard, S., Kawata, D., Martel, H., & Gibson, B. K. 2007, ApJ, 658, 60

Brook, C. B., Kawata, D., Gibson, B. K., & Freeman, K. C. 2004, ApJ, 612, 894

Buder, S., Lind, K., Ness, M. K., et al. 2018a, ArXiv e-prints, arXiv:1804.05869

Buder, S., Asplund, M., Duong, L., et al. 2018b, MNRAS, 478, 4513

Butler, K., & Giddings, J. 1985, Newsletter on the analysis of astronomical spectra No. 9, University of London

Campos, F., Pelisoli, I., Kamann, S., et al. 2018, MNRAS, 481, 4397

Carballo-Bello, J. A., Martínez-Delgado, D., Navarrete, C., et al. 2018, MNRAS, 474, 683

Carretta, E. 2006, AJ, 131, 1766

—. 2014, ApJ, 795, L28

Carretta, E. 2015, ApJ, 810, 148

Carretta, E., Bragaglia, A., Gratton, R., & Lucatello, S. 2009, A&A, 505, 139

Carretta, E., Bragaglia, A., Gratton, R. G., et al. 2006, A&A, 450, 523

Carretta, E., Bragaglia, A., Gratton, R. G., Lucatello, S., & Momany, Y. 2007, A&A, 464, 927

Carretta, E., Bragaglia, A., Gratton, R. G., et al. 2010, A&A, 516, A55

Carretta, E., Lucatello, S., Gratton, R. G., Bragaglia, A., & D'Orazi, V. 2011, A&A, 533, A69

Carretta, E., Bragaglia, A., Gratton, R. G., et al. 2013, A&A, 557, A138

—. 2014, A&A, 564, A60

Casetti-Dinescu, D. I., Girard, T. M., Herrera, D., et al. 2007, AJ, 134, 195

Casey, A. R., Hogg, D. W., Ness, M., et al. 2016a, arXiv e-prints, arXiv:1603.03040

Casey, A. R., Hawkins, K., Hogg, D. W., et al. 2016b, ArXiv e-prints, arXiv:1609.02914

Castelli, F. 2005, Memorie della Societa Astronomica Italiana Supplementi, 8, 25

Castelli, F., & Kurucz, R. L. 2004, ArXiv Astrophysics e-prints, astro-ph/0405087

Černiauskas, A., Kučinskas, A., Klevas, J., et al. 2017, A&A, 604, A35

Chen, S., Richer, H., Caiazzo, I., & Heyl, J. 2018, ApJ, 867, 132

Cheng, J. 2012, in American Astronomical Society Meeting Abstracts, Vol. 219, American Astronomical Society Meeting Abstracts #219, 205.03

Clem, J. L., Landolt, A. U., Hoard, D. W., & Wachter, S. 2011, AJ, 141, 115

Comerón, S., Salo, H., Knapen, J. H., & Peletier, R. F. 2019, A&A, 623, A89

Conrad, C., Scholz, R.-D., Kharchenko, N. V., et al. 2014, A&A, 562, A54

Cordero, M. J., Pilachowski, C. A., Johnson, C. I., et al. 2014, ApJ, 780, 94

Creevey, O., Grundahl, F., Thévenin, F., et al. 2019, A&A, 625, A33

Cui, X.-Q., Zhao, Y.-H., Chu, Y.-Q., et al. 2012, Research in Astronomy and Astrophysics, 12, 1197

Cummings, J. D., Geisler, D., & Villanova, S. 2017, ApJ, 1704.02349v1

Cunha, K., Frinchaboy, P. M., Souto, D., et al. 2016, AN, 1601.03099v1

Damiani, F., Bonito, R., Magrini, L., et al. 2016, A&A, 591, A74

D'Antona, F., Bellazzini, M., Caloi, V., et al. 2005, ApJ, 631, 868

De Silva, G. M., Freeman, K. C., Bland-Hawthorn, J., et al. 2015, MNRAS, 449, 2604

Deal, M., Alecian, G., Lebreton, Y., et al. 2018, A&A, 1806.10533v1

den Brok, M., van de Ven, G., van den Bosch, R., & Watkins, L. 2014, MNRAS, 438, 487

Denissenkov, P. A., VandenBerg, D. A., Kopacki, G., & Ferguson, J. W. 2017, ApJ, 849, 159

Dinescu, D. I., Girard, T. M., & van Altena, W. F. 1999, AJ, 117, 1792

Dobbie, P. D., Day-Jones, A., Williams, K. A., et al. 2012, MNRAS, 423, 2815

Dobbie, P. D., Napiwotzki, R., Burleigh, M. R., et al. 2009, MNRAS, 395, 2248

Dobrovolskas, V., Kučinskas, A., Bonifacio, P., et al. 2014, A&A, 565, A121

D'Orazi, V., Gratton, R. G., Angelou, G. C., et al. 2015, MNRAS, 449, 4038

Dotter, A., Ferguson, J. W., Conroy, C., et al. 2015, MNRAS, 446, 1641

Dotter, A., Sarajedini, A., Anderson, J., et al. 2010, ApJ, 708, 698

Drawin, H.-W. 1968, Zeitschrift fur Physik, 211, 404

Drawin, H. W. 1969, Zeitschrift fur Physik, 225, 470

Duong, L., Freeman, K. C., Asplund, M., et al. 2018, MNRAS, 476, 5216

Fabbian, D., Recio-Blanco, A., Gratton, R. G., & Piotto, G. 2005, A&A, 434, 235

Fabbro, S., Venn, K. A., O'Briain, T., et al. 2018, MNRAS, 475, 2978

François, P., Pasquini, L., Biazzo, K., Bonifacio, P., & Palsa, R. 2013, A&A, 552, A136

Freeman, K. C. 1987, ARA&A, 25, 603

Friel, E. D., Janes, K. A., Tavarez, M., et al. 2002, AJ, 124, 2693

Fritzewski, D. J., Barnes, S. A., James, D. J., et al. 2019, A&A, 1901.04507v1

Fu, X., Bressan, A., Marigo, P., et al. 2018, MNRAS, 476, 496

Gaia Collaboration, Brown, A. G. A., Vallenari, A., et al. 2018, A&A, 616, A1

Gerashchenko, A. N., Kadla, Z. I., & Malakhova, Y. N. 1999, Astronomy Reports, 43, 20

Gilmore, G., & Reid, N. 1983, MNRAS, 202, 1025

Gilmore, G., Randich, S., Asplund, M., et al. 2012, The Messenger, 147, 25

González, J. F., & Lapasset, E. 2002, AJ, 123, 3318

Gratton, R., Sneden, C., & Carretta, E. 2004, ARA&A, 42, 385

Gratton, R. G. 1982, ApJ, 257, 640

Gratton, R. G., Carretta, E., Bragaglia, A., Lucatello, S., & D'Orazi, V. 2010, A&A, 517, A81

Gratton, R. G., & Contarini, G. 1994, A&A, 283, 911

Gratton, R. G., Villanova, S., Lucatello, S., et al. 2012, A&A, 544, A12

Gray, D. F. 2005, The Observation and Analysis of Stellar Photospheres (Cambridge University Press)

Grevesse, N., Asplund, M., & Sauval, A. J. 2007, Space Sci. Rev., 130, 105

Grevesse, N., & Sauval, A. J. 1998, Space Sci. Rev., 85, 161

Grupp, F. 2004a, A&A, 420, 289

—. 2004b, A&A, 426, 309

Gruyters, P., Casagrande, L., Milone, A. P., et al. 2017, A&A, 603, A37

Gruyters, P., Korn, A. J., Richard, O., et al. 2013, A&A, 555, A31

Gruyters, P., Nordlander, T., & Korn, A. J. 2014, A&A, 567, A72

Guiglion, G., Recio-Blanco, A., de Laverny, P., et al. 2015, A&A, 583, A91

Gustafsson, B., Edvardsson, B., Eriksson, K., et al. 2008, A&A, 486, 951

Harris, W. E. 1996, AJ, 112, 1487

Hayden, M. R., Bovy, J., Holtzman, J. A., et al. 2015, ApJ, 808, 132

Hayden, M. R., Recio-Blanco, A., de Laverny, P., et al. 2017, A&A, 1711.05751v1

Hayden, M. R., Bland-Hawthorn, J., Sharma, S., et al. 2019, 1901.07565v1

Haywood, M., Di Matteo, P., Lehnert, M. D., Katz, D., & Gómez, A. 2013, A&A, 560, A109

Heiter, U., Soubiran, C., Netopil, M., & Paunzen, E. 2014, A&A, 561, A93

Heitsch, F., & Richtler, T. 1999, A&A, 347, 455

Hendricks, B., Koch, A., Walker, M., et al. 2014, A&A, 572, A82

Ishigaki, M. N., Chiba, M., & Aoki, W. 2012, ApJ, 753, 64

Jacobson, H. R., Friel, E. D., & Pilachowski, C. A. 2011, AJ, 141, 58

Jofré, P., Heiter, U., Soubiran, C., et al. 2015, A&A, 582, A81

Jurić, M., Ivezić, Ž., Brooks, A., et al. 2008, ApJ, 673, 864

Kacharov, N., Bianchini, P., Koch, A., et al. 2014, A&A, 567, A69

Kains, N., Bramich, D. M., Figuera Jaimes, R., et al. 2012, A&A, 548, A92

Kaluzny, J., Pych, W., Rucinski, S. M., & Thompson, I. B. 2006, actaa, 56, 237

Karovicova, I., White, T. R., Nordlander, T., et al. 2018, MNRAS, 475, L81

Katz, D., Sartoretti, P., Cropper, M., et al. 2019, A&A, 622, A205

Kirby, E. N., Guhathakurta, P., Bolte, M., Sneden, C., & Geha, M. C. 2009, ApJ, 705, 328

Kobayashi, C., Umeda, H., Nomoto, K., Tominaga, N., & Ohkubo, T. 2006, ApJ, 653, 1145

Koch, A., & McWilliam, A. 2008, AJ, 135, 1551

Kordopatis, G., Wyse, R. F. G., Gilmore, G., et al. 2015, A&A, 582, A122

Kovalevsky, J., Lindegren, L., Perryman, M. A. C., et al. 1997, A&A, 323, 620

Kravtsov, V., Alcaíno, G., Marconi, G., & Alvarado, F. 2011, A&A, 527, L9

Kruijssen, J. M. D., Pfeffer, J. L., Reina-Campos, M., Crain, R. A., & Bastian, N. 2018, MNRAS, arXiv:1806.05680

Kučinskas, A., Dobrovolskas, V., & Bonifacio, P. 2014, A&A, 568, L4

Kuzma, P. B., Da Costa, G. S., & Mackey, A. D. 2018, MNRAS, 473, 2881

Kuzma, P. B., Da Costa, G. S., Mackey, A. D., & Roderick, T. A. 2016, MNRAS, 461, 3639

Lapenna, E., Mucciarelli, A., Lanzoni, B., et al. 2014, ApJ, 797, 124

Lardo, C., Mucciarelli, A., & Bastian, N. 2016, MNRAS, 457, 51

Lardo, C., Pancino, E., Mucciarelli, A., & Milone, A. P. 2012, A&A, 548, A107

Lardo, C., Pancino, E., Mucciarelli, A., et al. 2013, MNRAS, 433, 1941

Larsen, S. S., Baumgardt, H., Bastian, N., et al. 2015, ApJ, 804, 71

Lee, J.-W. 2018, ApJS, 238, 24

Letarte, B., Hill, V., Jablonka, P., et al. 2006, A&A, 453, 547

Leung, H. W., & Bovy, J. 2019, MNRAS, 483, 3255

Li, Z., & Deng, Y. 2018, Ap&SS, 363, 97

Lim, D., Lee, Y.-W., Pasquato, M., Han, S.-I., & Roh, D.-G. 2016, ApJ, 832, 99

Lind, K., Bergemann, M., & Asplund, M. 2012, MNRAS, 427, 50

Loebman, S. R., Roškar, R., Debattista, V. P., et al. 2011, ApJ, 737, 8

Luri, X., Brown, A. G. A., Sarro, L. M., et al. 2018, A&A, 616, A9

Mackereth, J. T., & Bovy, J. 2018, PASP, 130, 114501

Magrini, L., Vincenzo, F., Randich, S., et al. 2018, A&A, 618, A102

Majewski, S. R., Schiavon, R. P., Frinchaboy, P. M., et al. 2015, ArXiv e-prints, arXiv:1509.05420

Marigo, P., Girardi, L., Bressan, A., et al. 2017, ApJ, 835, 77

Marino, A. F., Milone, A. P., Yong, D., et al. 2014, MNRAS, 442, 3044

Marino, A. F., Milone, A. P., Casagrande, L., et al. 2016, MNRAS, 459, 610

Martin, N. F., Ibata, R. A., Bellazzini, M., et al. 2004, MNRAS, 348, 12

Mashonkina, L., Neretina, M., Sitnova, T., & Pakhomov, Y. 2019, arXiv e-prints, arXiv:1908.03370

Mashonkina, L., Zhao, G., Gehren, T., et al. 2008, A&A, 478, 529

McMahon, R. G., Banerji, M., Gonzalez, E., et al. 2013, The Messenger, 154, 35

Menzies, J. W. 1967, Nature, 214, 689

Mikolaitis, Š., Hill, V., Recio-Blanco, A., et al. 2014, A&A, 572, A33

Milone, A. P., Bedin, L. R., Piotto, G., et al. 2008, ApJ, 673, 241

Milone, A. P., Piotto, G., King, I. R., et al. 2010, ApJ, 709, 1183

Milone, A. P., Piotto, G., Bedin, L. R., et al. 2012, ApJ, 744, 58

Milone, A. P., Marino, A. F., Piotto, G., et al. 2013, ApJ, 767, 120

—. 2015, ApJ, 808, 51

Milone, A. P., Marino, A. F., Bedin, L. R., et al. 2019, MNRAS, 484, 4046

Minchev, I., Chiappini, C., & Martig, M. 2013, A&A, 1208.1506v3

Minchev, I., Chiappini, C., Martig, M., et al. 2014, ApJ, 781, L20

Minchev, I., Matijevic, G., Hogg, D. W., et al. 2019, MNRAS, 1195

Monelli, M., Testa, V., Bono, G., et al. 2015, ApJ, 812, 25

Mucciarelli, A., Bellazzini, M., Ibata, R., et al. 2017, A&A, 605, A46

Mura-Guzmán, A., Villanova, S., Muñoz, C., & Tang, B. 2018, MNRAS, 474, 4541

Nardiello, D., Milone, A. P., Piotto, G., et al. 2015, A&A, 573, A70

—. 2018, MNRAS, 477, 2004

Ness, M., Hogg, D. W., Rix, H.-W., Ho, A. Y. Q., & Zasowski, G. 2015, ApJ, 16

Netopil, M. 2017, MNRAS, 469, 3042

Nissen, P. E., & Schuster, W. J. 2010, A&A, 511, L10

—. 2011, A&A, 530, A15

O'Malley, E. M., Gilligan, C., & Chaboyer, B. 2017, ApJ, 1703.01915v1

Osorio, Y., Barklem, P. S., Lind, K., et al. 2015, A&A, 579, A53

Otsuka, M., Tajitsu, A., Hyung, S., & Izumiura, H. 2010, ApJ, 723, 658

Pancino, E., Romano, D., Tang, B., et al. 2017, A&A, 601, A112

Pancino, E., Lardo, C., Altavilla, G., et al. 2017, A&A, 598, A5

Pasquini, L., Avila, G., Blecha, A., et al. 2002, The Messenger, 110, 1

Pehlivan Rhodin, A., Hartman, H., Nilsson, H., & Jönsson, P. 2017, A&A, 598, A102

Piatti, A. E., & Koch, A. 2018, AJ, 867, 8

Piotto, G., Bedin, L. R., Anderson, J., et al. 2007, ApJ, 661, L53

Piotto, G., Milone, A. P., Anderson, J., et al. 2012, ApJ, 760, 39

Piotto, G., Milone, A. P., Bedin, L. R., et al. 2015, AJ, 149, 91

Pritzl, B. J., Venn, K. A., & Irwin, M. 2005, AJ, 130, 2140

Quinn, P. J., Hernquist, L., & Fullagar, D. P. 1993, ApJ, 403, 74

Randich, S., Gilmore, G., & Consortium, G.-E. 2013, The Messenger, 154, 47

Re Fiorentin, P., Bailer-Jones, C. A. L., Lee, Y. S., et al. 2007, A&A, 467, 1373

Recio-Blanco, A., Bijaoui, A., & de Laverny, P. 2006, MNRAS, 370, 141

Recio-Blanco, A., de Laverny, P., Kordopatis, G., et al. 2014, A&A, 567, A5

Reetz, J. 1991, Diplomarbeit, Universität München

Rix, H.-W., Ting, Y.-S., Conroy, C., & Hogg, D. W. 2016, ApJ, 826, L25

Roederer, I. U., & Thompson, I. B. 2015, MNRAS, 449, 3889

Ross, T. L., Holtzman, J., Anthony-Twarog, B. J., et al. 2013, arXiv e-prints, arXiv:1310.4553

Roškar, R., Debattista, V. P., Quinn, T. R., Stinson, G. S., & Wadsley, J. 2008, ApJ, 684, L79

Ruchti, G. R., Bergemann, M., Serenelli, A., Casagrande, L., & Lind, K. 2013, MNRAS, 429, 126

Ruchti, G. R., Fulbright, J. P., Wyse, R. F. G., et al. 2011, ApJ, 737, 9

Rybizki, J., Demleitner, M., Fouesneau, M., et al. 2018, Publications of the Astronomical Society of the Pacific, 130, 074101

Sales, L. V., Helmi, A., Abadi, M. G., et al. 2009, MNRAS, 400, L61

San Roman, I., Muñoz, C., Geisler, D., et al. 2015, A&A, 579, A6

Santos, N. C., Lovis, C., Melendez, J., et al. 2012, A&A, 1201.1108v1

Schoenrich, R., & Binney, J. 2009a, MNRAS, 0809.3006v2

—. 2009b, MNRAS, 0907.1899v1

Schoenrich, R., & McMillan, P. 2017, MNRAS, 1605.02338v2

Schoenrich, R., McMillan, P., & Eyer, L. 2019, MNRAS, 1902.02355v1

Schönrich, R., & Bergemann, M. 2014, MNRAS, 443, 698

Schönrich, R., Binney, J., & Dehnen, W. 2010, MNRAS, 403, 1829

Sheth, K., Elmegreen, D. M., Elmegreen, B. G., et al. 2008, ApJ, 675, 1141

Shipp, N., Drlica-Wagner, A., Balbinot, E., et al. 2018, ApJ, 862, 114

Simioni, M., Milone, A. P., Bedin, L. R., et al. 2016, MNRAS, 463, 449

Simpson, J. D., Martell, S. L., & Navin, C. A. 2017, MNRAS, 465, 1123

Sitnova, T. M., Mashonkina, L. I., & Ryabchikova, T. A. 2013, Astronomy Letters, 39, 126

Smiljanic, R., Korn, A. J., Bergemann, M., et al. 2014, A&A, 1409.0568v1

Smith, G. H., & Langland-Shula, L. E. 2009, PASP, 121, 1054

Smith, G. H., & Mateo, M. 1990, ApJ, 353, 533

Sobeck, J. S., Kraft, R. P., Sneden, C., et al. 2011, AJ, 141, 175

Steenbock, W., & Holweger, H. 1984, A&A, 130, 319

Steinmetz, M., Zwitter, T., Siebert, A., et al. 2006, AJ, 132, 1645

Stonkutė, E., Koposov, S. E., Howes, L. M., et al. 2016, MNRAS, 460, 1131

Székely, P., Kiss, L. L., Jackson, R., et al. 2007, A&A, 463, 589

Thygesen, A. O., Sbordone, L., Andrievsky, S., et al. 2014, A&A, 572, A108

Timmes, F. X., Woosley, S. E., & Weaver, T. A. 1995, ApJS, 98, 617

Ting, Y.-S., Conroy, C., Rix, H.-W., & Cargile, P. 2018, ArXiv e-prints, arXiv:1804.01530

Tolstoy, E., Hill, V., & Tosi, M. 2009, ARA&A, 47, 371

Tucholke, H. J. 1992, A&AS, 93, 311

Turri, P., McConnachie, A. W., Stetson, P. B., et al. 2015, ApJ, 1509.01764v1

van den Bosch, R., de Zeeuw, T., Gebhardt, K., Noyola, E., & van de Ven, G. 2006, ApJ, 641, 852

VandenBerg, D. A., Bergbusch, P. A., Ferguson, J. W., & Edvardsson, B. 2014, ApJ, 794, 72

Villalobos, Á., & Helmi, A. 2008, MNRAS, 391, 1806

Villalobos, Á., Kazantzidis, S., & Helmi, A. 2010, ApJ, 718, 314

Villanova, S., & Geisler, D. 2011, A&A, 535, A31

Wagner-Kaiser, R., Sarajedini, A., von Hippel, T., et al. 2017, MNRAS, 468, 1038

Walker, M. G., Mateo, M., Olszewski, E. W., et al. 2006, AJ, 131, 2114

Worley, C. C., & Cottrell, P. L. 2010, MNRAS, 406, 2504

Worley, C. C., Hill, V., Sobeck, J., & Carretta, E. 2013, A&A, 553, A47

Xing, Q. F., & Zhao, G. 2018, MNRAS, 476, 5388

Yakovleva, S. A., Voronov, Y. V., & Belyaev, A. K. 2016, A&A, 593, A27

Yan, Y., Du, C., Liu, S., et al. 2019, arXiv e-prints, arXiv:1906.03875

Yong, D., & Grundahl, F. 2008, ApJ, 672, L29

Yong, D., Grundahl, F., Nissen, P. E., Jensen, H. R., & Lambert, D. L. 2005, A&A, 438, 875

Yong, D., Grundahl, F., & Norris, J. E. 2015, MNRAS, 446, 3319

Yong, D., Meléndez, J., Grundahl, F., et al. 2013, MNRAS, 434, 3542

Yong, D., Roederer, I. U., Grundahl, F., et al. 2014, MNRAS, 441, 3396

Zhao, G., Mashonkina, L., Yan, H. L., et al. 2016, ApJ, 833, 225